Electronic structures and magnetic properties of Fe-doped ferromagnetic semiconductors

(Fe

)

29   12

Abstract

In the emerging field of spintronics, utilizing the spin degree of freedom of materials is thought to be promising to realize new functionalities that conventional electronic devices do not have. One candidate material for such technology is ferromagnetic semiconductors (FMS), which possess the properties of both ferromagnet and semiconductor and have been intensively studied since the discovery of Mn doped III-V semiconductors, (Ga,Mn)As and (In,Mn)As. In these materials, the ferromagnetic (FM) interaction is mediated by carriers, and hence it is possible to manipulate the ferromagnetism by controlling the number of carriers. In fact, it was demonstrated that it is possible to control the ferromagnetism by applying gate voltage or impinging light onto the materials. However, there has been problems for practical applications: the Curie temperatures (T_C) of these materials are still below room temperature, and only p-type materials are available.

Recently, Fe-doped ferromagnetic semiconductors, namely, (In,Fe)As:Be, (Ga,Fe)Sb, (Al,Fe)Sb, (In,Fe)Sb, and Ge:Fe, have been synthesized, and have the potential to overcome the above-mentioned problems. First, the Curie temperatures of (Ga,Fe)Sb and (In,Fe)Sb are higher than room temperature, 340 K for 25% Fe-doped (Ga,Fe)Sb and 335 K for 16% Fe-doped (In,Fe)Sb. Second, various types of transport properties are realized: p-type for (Ga,Fe)Sb and Ge:Fe, n-type for (In,Fe)As:Be and (In,Fe)Sb, and insulating for (Al,Fe)Sb.

In this thesis, their electronic structures and magnetic properties have been investigated using soft x-ray spectroscopy, namely, x-ray absorption spectroscopy (XAS), x-ray magnetic circular dichroism (XMCD), resonance photoemission spectroscopy (RPES), and soft x-ray angle-resolved photoemission spectroscopy (SX-ARPES). Furthermore, we have performed first-principles supercell calculation to obtain further insight into the electronic structures and the origin of the ferromagnetism.

In Chapter 3, the results of XAS and XMCD measurements to study the magnetization process of (Al,Fe)Sb thin films are presented. From magnetization curves measured by XMCD at various temperatures, it was found that nanoscale ferromagnetic domains of 300-400 μ_B exist even at room temperature well above the T_C of 40 K. This was attributed to a non-uniform distribution of Fe atoms on the nanoscale.

Chapter 4 is devoted to RPES, SX-ARPES, and first-principles calculation studies of group IV FMS Fe-doped Ge (Ge:Fe). ARPES spectra showed that the Fermi level is located 0.35 eV above the valence band maximum. From RPES spectra, non-dispersive Fe $3d$ states were found to exist at the Fermi

level, which was attributed to majority-spin p-$d(t_2)$ antibonding states and also to minority-spin Fe $3d(e)$ states. It was suggested that the ferromagnetic interaction is mediated by double-exchange interaction within the minority-spin Fe $3d(e)$ band.

In Chapter 5, the electronic structure of (Ga,Fe)Sb studied by XAS, XMCD, RPES and first-principles supercell calculation is discussed. From XAS and XMCD, it was suggested that Fe takes the $3d^6\underline{L}$ configuration, where $\underline{L}$ denotes a ligand hole. RPES spectra indicated the itinerant and correlated nature of Fe $3d$ electrons. The calculated electronic structure was very similar to that of (Ga,Mn)As except that the additional electron of Fe compared to Mn occupies the minority-spin e states, which may be the source of the nanoscale ferromagnetic order.

Chapter 6 summarizes the electronic structures of Fe-doped III-V semiconductors obtained by first-principles supercell calculation. The electronic structures can be understood on the basis of the electronic structures of Mn-doped III-V compounds except that the additional electron of Fe compared to Mn occupies either a majority-spin p-t_2 hybridized antibonding state ($t_{a,\uparrow}$) or a minority-spin e state ($e_\downarrow$). The $e_\downarrow$ state is preferentially occupied in the cases of (Ga,Fe)Sb and (In,Fe)Sb, where the valence band or p level is located high in energy and, therefore, it is more stable for the additional electron to occupy the $e_\downarrow$ state than to occupy the $t_{a,\uparrow}$ state. It was suggested that the ferromagnetism in Fe-doped III-V FMSs originates from the nanoscale fluctuation of Fe atom distribution as already suggested in the preceding chapters.

Contents

Chapter 1

Introduction

1.1 Diluted Magnetic Semiconductors

By exploiting the charge degree of freedom of carriers in semiconductors, electronics has resulted in a great success giving enormous benefits to human society. For further technological development, utilizing the spin of electron in addition to charge is thought to be important. This new field, called spintronics, is therefore expected to open up a way for new technologies [1]. One of the major approaches to achieve that goal is to synthesize magnetic semiconductors possessing the properties of semiconductor and magnetic materials. Especially, ferromagnetic semiconductors are highly desirable, because they can probably be used as non-volatile memories, and they can produce spin-polarized carriers, which may add another degree of freedom for information processing.

In the early 1960s, a class of ferromagnetic semiconductors europium chalcogenides were discovered [2–5]. In these materials, exchange interactions between conduction $5d$-$6s$ electrons and localized $4f$ electrons lead to a number of peculiar and interesting properties, such as the red shift of band gap at the ferromagnetic transition. Unfortunately, the crystal growth of europium chalcogenides is notoriously difficult, and the crystal structure (rock salt structure) is very much different from that of widely used group IV, III-V, and II-VI semiconductors such as Si (diamond) and GaAs (zinc-blende). In addition, the Curie temperatures of these materials are well below 100 K. These problems make it difficult to use them for practical spintronic devices.

In the late 1970s, a different approach was taken to explore new magnetic semiconductors, which is to dope magnetic atoms into a nonmagnetic semiconductor [6]. Since the magnetic atoms are doped dilutely, this class of magnetic semiconductors are called diluted magnetic semiconductors (DMSs), schematically described in Fig. 1.1B. Here, the schematic picture of magnetic semicon-
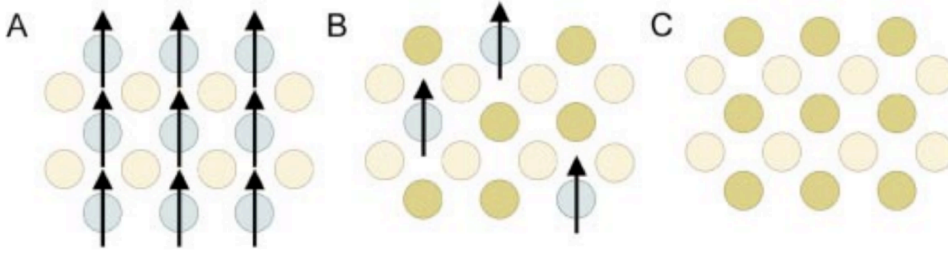
Figure 1.1: Three types of semiconductors [7]: (A) a magnetic semiconductor, in which a periodic array of magnetic element is present; (B) a diluted magnetic semiconductor, an alloy between nonmagnetic semiconductor and magnetic element; and (C) a nonmagnetic semiconductor, which contains no magnetic ions.

ductors such as EuO is also shown in panel A, in which magnetic elements are periodically located, and nonmagnetic semiconductor in panel C. The studies of DMSs were mostly done on II-VI semiconductors such as CdTe and ZnSe doped with Mn, mainly because the valence matching between Mn^{2+} and $cation^{2+}$ makes the material growth relatively easy. These II-VI DMSs attracted much attention since they showed interesting phenomena such as giant Faraday rotation upon the application of magnetic field [6]. Unfortunately, however, it is difficult to dope the II-VI DMSs with p- or n-type carriers, and also in most cases they are not ferromagnetic, which limits their device applications.

In 1989, Munekata *et al.* succeeded in incorporating Mn ions up to 18% into the III-V semiconductor InAs thin films exceeding their low solubility limit of the order of 10^{18} cm^{-3} ($\sim$0.1%) by low-temperature molecular beam epitaxy (LT-MBE), where magnetic elements are introduced under non-equilibrium conditions [8]. Schematic phase diagram of the temperature and Mn content dependence of the physical properties of MBE-grown samples is shown in Fig. 1.2. As can be seen from the figure, when a high concentration of magnetic ions are introduced in excess of the solubility limit under high temperature near equilibrium condition, the formation of secondary phase occurs. However, in the case of low-temperature growth, there is not enough thermal energy to form secondary phase, and a local potential landscape allows the epitaxial growth of a single-crystal alloy. Unlike Mn doped II-VI DMSs, where Mn^{2+} ions do not provide carriers, in the III-V semiconductor host, Mn^{2+} ions act as acceptors providing holes into the system, because the valence of Mn^{2+} is smaller than that of the group III element.

In 1992, soon after the success of epitaxial growth of (In,Mn)As by LT-MBE, Ohno *et al.* observed anomalous Hall effects in this material indicating
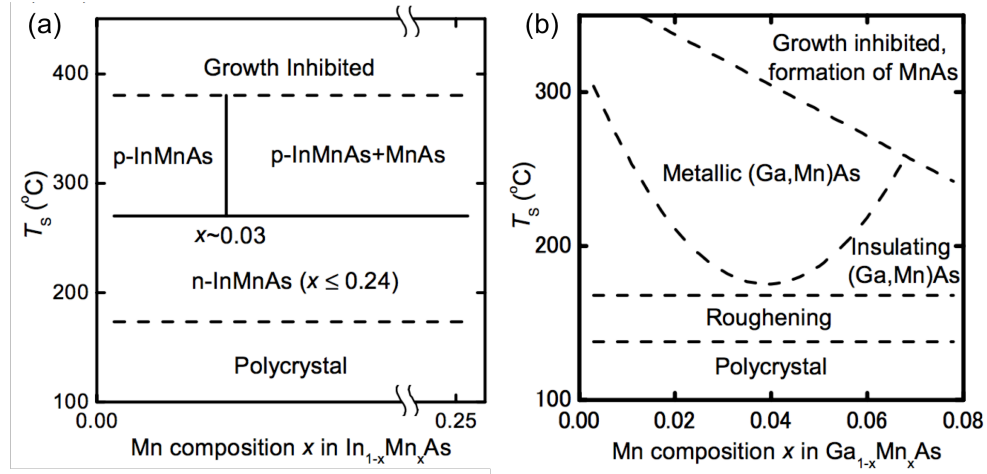
Figure 1.2: Schematic phase diagram showing the relation between growth parameters of MBE (substate temperature and Mn concentration) and the properties of (a) (In,Mn)As [9] and (b) (Ga,Mn)As [10], both of which are grown on GaAs(001).

the existence of ferromagnetic order below 7.5 K [11]. Subsequently, in 1996, Ohno *et al.* discovered the new Mn doped III-V DMSs (Ga,Mn)As. Surprisingly (Ga,Mn)As was found to be ferromagnetic, whose Curie temperature was as high as 60 K [12] and increased as hole concentration increased [13]. These discoveries have driven many researchers to study Mn doped III-V semiconductors, and a large number of papers have been published (for recent review, see [14,15]). Thanks to the development of sophisticated growth and annealing procedures and nanostructure engineering, the Curie temperature was pushed up to 200 K at the highest for (Ga,Mn)As [16], and 90 K for (In,Mn)As [17].

1.2 Carrier-induced Ferromagnetism

An interesting property of ferromagnetic semiconductors (FMSs) is that the ferromagnetic interaction are mediated by carriers. This kind of ferromagnetism is called carrier-induced ferromagnetism, which has been the central issue in the field of semiconductor spintronics. Figures 1.3(a)-(c) show the Mn concentration x dependence of the hole concentration p, the magnetization M, and the Curie temperature T_C, respectively, measured on the carefully optimized (Ga,Mn)As samples [18], which suggests that the doped Mn ions act as acceptors providing hole carriers and as local magnetic moments. The Curie temperature depends both on the concentration of holes and that of Mn as mean field theory predicts ($T_C \propto xp^{\frac{1}{3}}$) [20]. It should be noted that, without
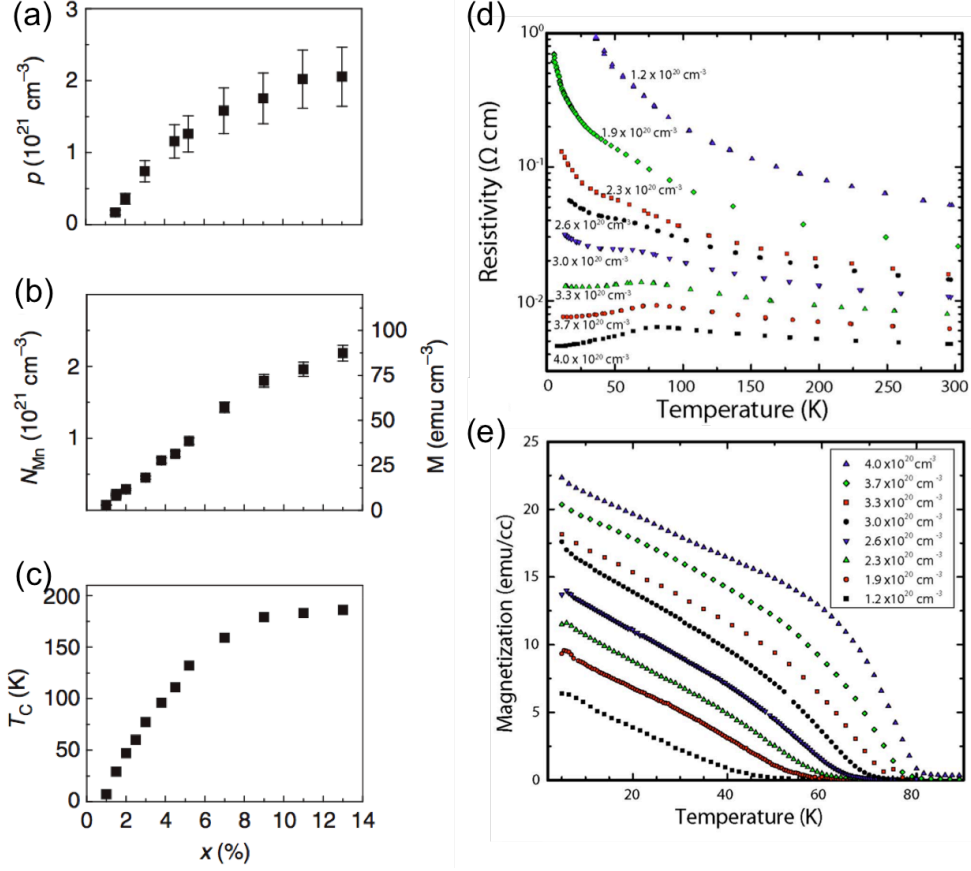
Figure 1.3: The Mn composition dependence of (a) hole concentration, (b) magnetization or the amount of magnetically active Mn atoms, and (c) Curie temperature, measured on carefully optimized sample without notable interstitial Mn defects [18]. (d) and Resistivity and (e) magnetization as a function of temperature of irradiated $Ga_{0.955}Mn_{0.045}As$ [19].

the optimization of growth and annealing conditions, Mn atoms would also be introduced into interstitial sites and act as double donors compensating two holes per one interstitial Mn (Mn_{int}) [21, 22]. In addition, the magnetic moment of Mn_{int} is known to be antiferromagnetically coupled to that of Mn atom at substitutional site (Mn_{sub}), which decreases the total magnetization of the sample [22, 23]. These two effects of the existence of Mn_{int} hinder ferromagnetic ordering and decrease the Curie temperature, and hence the properties of DMSs are significantly influenced by the preparation conditions. Figures 1.3(d) and (e) presents temperature dependence of resistivity and magnetization in a series of $Ga_{0.955}Mn_{0.045}As$ samples with different irradiation doses of Ne^+ ions that generate hole compensating defects, predominantly As vacancies, without

changing the amount of Mn atoms [19]. By the irradiation, the resistivity ex-trapolated to zero temperature significantly increases, which means that the sample turn from metal into insulator. Interestingly ferromagnetism is observed on its either side of metal insulator transition (MIT), but the magnitudes of both T_C and saturation spontaneous magnetization $M_s(T \rightarrow 0, H \rightarrow 0)$ de-ceases as the degree of compensation increases. This clearly suggests that the ferromagnetism is carrier-induced, and not only T_C but also the amount of Mn spins participating in the long-range ferromagnetic order becomes smaller on reducing the net hole concentration.

1.2.1   Spintronic Applications

Since ferromagnetism in Mn-doped III-V FMS is carrier induced, one may be able to control ferromagnetism by applying external fields to control carrier concentration, which is attractive for technological applications. Furthermore, via p-d exchange interaction between the spins of carriers in the valence band and the spins of localized $3d$ electrons, the carriers in the valence band are spin-polarized, which enables us to use these FMSs as a spin injector into nonmagnetic semiconductors.

Electric field control of ferromagnetism was first demonstrated using a metal-insulator-semiconductor field-effect transistor (MISFET) structure con-sisting of a thin (In,Mn)As channel of 5 nm [24]. Applying negative gate bias would increase the hole concentration in the channel and hence strengthen the ferromagnetic order, whereas applying positive bias would cause an opposite effect schematically described in Fig. 1.4(a). Actually the ferromagnetic order at 22.5K near T_C is strengthened by the bias voltage of -125 V and weakened or broken by the bias voltage of 125 V, as presented in Fig. 1.4(b). The Curie temperature is also varied by applying gate voltages as shown in Fig. 1.4(c). This kind of electric field control of ferromagnetism was also demonstrated for (Ga,Mn)As MISFET structures [25, 26].

Another way to control the ferromagnetism in carrier-induced FMSs is to impinge the light onto the materials and to create photo-generated carriers, as was first demonstrated in $In_{0.94}Mn_{0.06}As/GaSb/GaAs$ heterostructure [27, 28]. The schematic pictures of the structure and its band edge profile are shown in Figs. 1.5(a) and (b), respectively. Due to this peculiar band edge pro-file (broken-gap type-II alignment), where the surface Fermi level pinning inside the conduction band creates a large built-in electric field across the (In,Mn)As/GaSb heterostructure, photo generated holes in the GaSb layer can be transferred and accumulated in the (In,Mn)As layer and its vicinity. Since
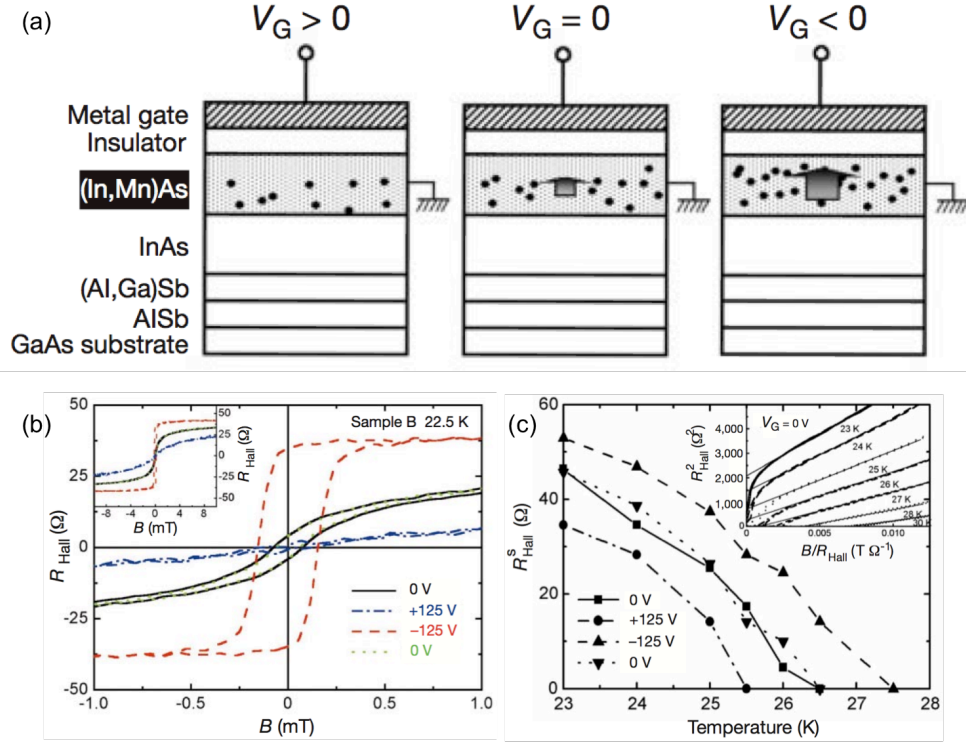
Figure 1.4: (a) Schematic pictures of (In,Mn)As field effect transistors under the gate bias voltage V_G. The hole carriers and the magnetization of Mn are depicted by filled circles and arrows, respectively. (b) Hall resistance R_{Hall} versus applied field B curves under three different gate biases. (c) Temperature dependence of spontaneous Hall resistance R_{Hall}^S under three different gate voltages. Inset shows the Arrot plots of R_{Hall}^2 vs B/R_{Hall}, from which R_{Hall}^S is determined [24].

electrons drift towards the opposite direction, holes do not recombine immediately with electrons even after light is switched off. The hole concentration estimated to be increased by ~ 4 % from 3.76×10^{19} cm^{-3} to 3.90×10^{19} cm^{-3}. Figure 1.5(c) shows the magnetization curves measured with SQUID at the temperature of 5 K before (open circles) and after (solid circles) light irradiation. It can be clearly seen that the paramagnetic sample turned into ferromagnetic by the illumination of light. The magnetization curve in the dark is fitted by Brillouin function with the constituent spin of $S = 75$ (solid line), which suggests that 30 Mn atoms form ferromagnetic clusters and the sample is very close to the ferromagnetic transition. This may be the reason why the small increase in hole concentration by 4% is enough for the appearance of ferromagnetic order.

The third demonstrated example of spintronic application of FMSs is the
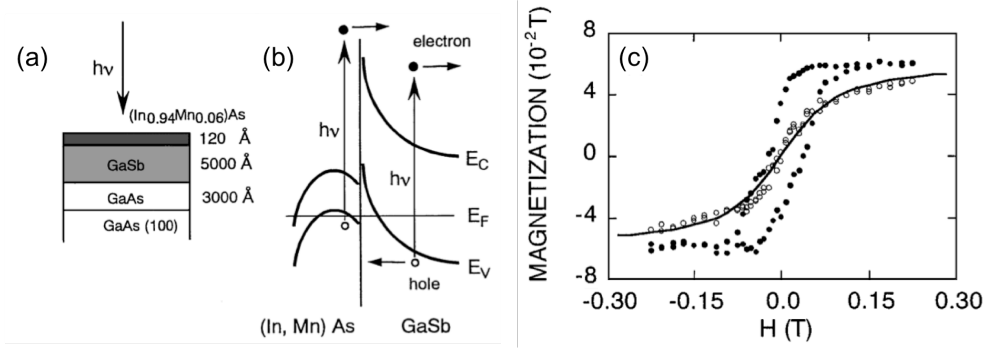
Figure 1.5: (a) Structure of the sample. (b) Band edge profile of (In,Mn)As/ GaSb heterostructure. (c) Magnetization curves at 5 K observed before (open circles) and after (solid circles) light irradiation. Solid line shows a fitted curve by Brillouin function [28].

spin-polarized light-emitting diode (spin-LED), which utilizes the spin polarization of carriers. The device structure is shown in Fig. 1.6(a). In this device, when a voltage is applied, the spin-polarized holes from (Ga,Mn)As travel over the GaAs spacer to the (In,Ga)As quantum well layer, where they recombine with the unpolarized electrons supplied from the bottom n-GaAs substrate. Since the holes are spin polarized, the light emitted in the recombination process has a specific helicity in order to conserve angular momentum. Figure 1.6(b) presents relative changes in electroluminescence (EL) polarization ΔP with respect to applied magnetic fields measured at the temperature of 6-52 K below and above T_C. Below $T = 31$ K, ΔP shows a hysteretic behavior and the coercive force increases as the temperature decreases, which reflects the ferromagnetic behavior of the (Ga,Mn)As layer. The inset of Fig. 1.6(c) shows that the temperature dependence of the relative remanent polarization $\Delta P(T, H = 0)$ follows the sample's magnetic moment M (solid black curve) measured by SQUID. These facts confirm the existence of carrier spin-polarization in (Ga,Mn)As and the possibility of spin injection into nonmagnetic semiconductors.

1.2.2   Exchange Mechanisms in DMSs

In this section, two different exchange mechanisms are presented: Zener's double exchange and Zener's p-d exchange, both of which favor ferromagnetic coupling.
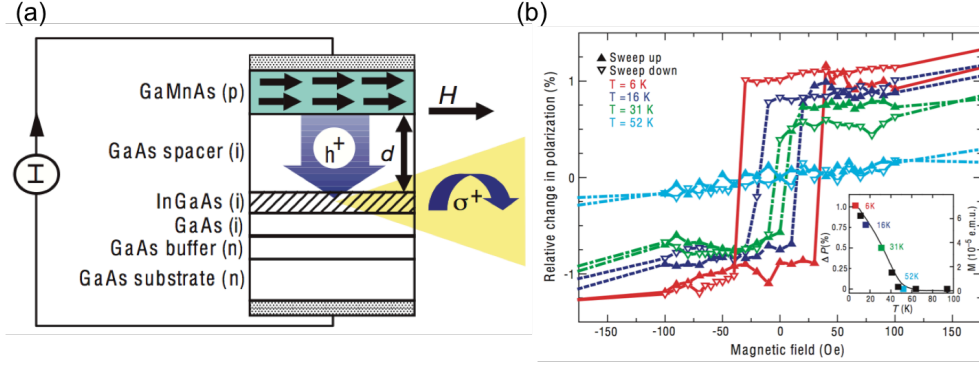
Figure 1.6: (a) Schematic picture of the GaMnAs/GaAs/InGaAs/GaAs heterostructure. (b) Hysteretic behavior of electroluminescence polarization with respect to the applied magnetic field. Inset shows remanent polarization (solid square) and remanent magnetization measured by a SQUID magnetometer (solid curve) [29].

Zener's Double Exchange

The basic concept of double exchange mechanism, first proposed by Zener [30], is as follows. When there exists two ions with different oxidation states, for example high-spin Mn^{3+} and Mn^{4+}, charge transfer from Mn^{3+} to adjacent Mn^{4+} occurs. Due to the Hund's coupling, the ferromagnetic alignment of spins of Mn^{3+} and Mn^{4+} is favored. Double exchange interaction gains energy through the d-electron transfer and occurs when Fermi energy (E_F) crosses the d band. Since carriers have d character, this interaction is likely to be relatively short-ranged.

Figure 1.7(a) shows the schematic spin-polarized density of states (DOS) of a transition-metal impurity in a wide-band-gap semiconductor such as Mn or Cr in GaN, where the Fermi level is assumed to fall within the partially occupied majority band of the t_2 impurity states. For an impurity band, the bandwidth scales linearly with the hopping matrix element t between neighboring impurities and as the square root of the impurity concentration c. Hence, the energy gain by double exchange mechanism is expressed as

$$\Delta E_{DX} \sim \sqrt{c}|t|, \tag{1.1}$$

and become largest when the Fermi level lies in the middle of the impurity band. If double exchange is dominant, the Curie temperature scales with $\sqrt{c}$ [31].

Figure 1.7: (a) Schematic diagram of the electronic structure in the case of double exchange. The full curves show the spin-up and spin-down impurity bands for a small concentration, and the dashed curves for a larger concentration. (b) Schematic for *p-d* exchange. The dashed curve represents the valence band after interaction with the magnetic impurities (*p-d* mixing) [31].
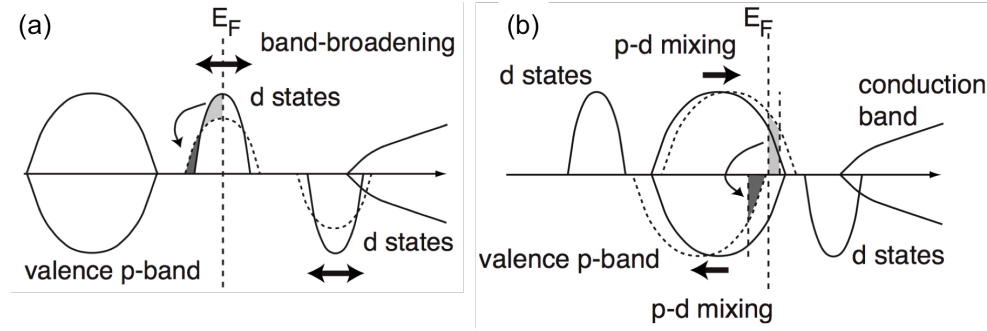
Zener's *p-d* Exchange

Figure 1.7(b) shows the case where Zener's *p-d* exchange interaction [32] is dominant. This is the case for narrow-gap semiconductors like GaSb or InSb, where the Mn^{2+} majority-spin d levels lie below the ligand p band, and the minority-spin d level lies above E_F. Due to the charge neutrality, one electron per Mn is missing in the valence band as indicated by the position of E_F. The solid curve represents the case where $1/2$ electron per Mn impurity is missing in both spin-up and spin-down valence bands, and the dashed curve represents the existence of the valence band exchange splitting due to *p-d* hybridization. The hybridization between the impurity d orbitals and the ligand p orbitals shifts the majority-spin p band to higher energies and the minority-spin p band to lower energies. If the hybridization is sufficiently strong, the minority p band becomes completely occupied, while one electron per Mn atom is missing in the majority p band, leading to a half-metallic density of states. Since carriers reside in the valence band having p character, *p-d* exchange interaction is likely to be long-ranged. If *p-d* exchange is dominant, the Curie temperature scales with the impurity concentration c [31].

Angle-resolved photoemission spectroscopy study of (Ga,Mn)As

In order to reveal the electronic structure of (Ga,Mn)As and its exchange mechanism, Kobayashi *et al.* [33] performed soft x-ray angle-resolved photoemission spectroscopy (SX-ARPES) measurements on a (Ga,Mn)As thin film with 2.5% Mn. The bulk sensitivity of SX-ARPES [34] is very helpful for the study of thin films whose surfaces are not clean and oxidized in most cases. The use
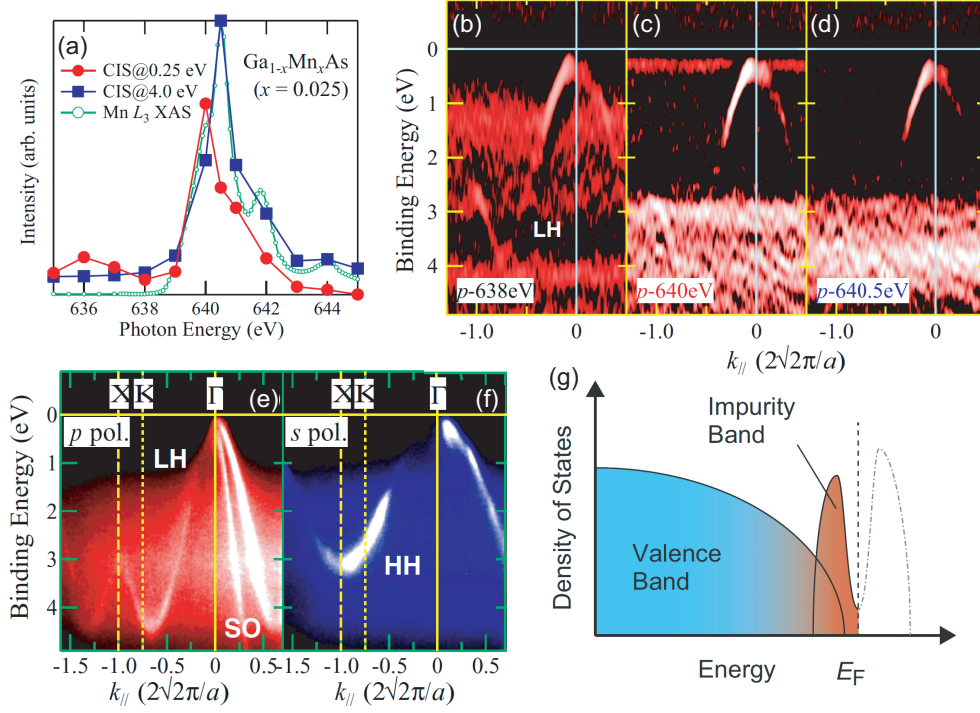
Figure 1.8: (a) Schematic diagram of the electronic structure in the case of double exchange. The full lines show the spin-up and spin-down impurity bands for a small concentration, and the dashed lines for a larger concentration. (b) Schematic for p-d exchange. The dashed curve represents the valence band after interaction with the magnetic impurities (p-d mixing) [31].

of soft x rays also made it possible to enhance the Mn $3d$ contributions to the band structure through the resonance photoemission effect at the Mn L_3 absorption edge. The basic principles of ARPES and resonance photoemission are presented in Chapter 2.

The results of the SX-ARPES experiment are summarized in Fig. 1.8. Figure 1.8(a) shows the x-ray absorption spectroscopy (XAS) spectrum of the $Ga_{0.975}Mn_{0.025}As$ thin film. It was demonstrated that XAS spectra of (Ga,Mn)As consist of two kinds of Mn components [23]: intrinsic signals from Mn atoms incorporated into GaAs lattice, which peaks at 640 eV, and extrinsic signals from Mn oxides segregated at the surface, which peaks at 640.5 eV. Figures 1.8(b)-(d) show ARPES spectra taken with the photon energies of off-resonance condition (638 eV), on-resonance condition for intrinsic Mn atoms (640 eV), and on-resonance condition for extrinsic Mn oxides (640.5 eV). At 640 eV, the non-dispersive signals appeared just below the Fermi level (E_F) and just above the valence band maximum (VBM), indicating the existence of a Mn $3d$-derived impurity band near E_F. The constant-initial-state (CIS)

spectra taken at the binding energies (E_B) of 0.25 eV and 4.0 eV are also shown in Fig. 1.8(a). The CIS spectrum at $E_B = 0.25$ eV showed clear resonance at 640 eV corresponding to the XAS signals from the intrinsic Mn atoms.

Figures 1.8 (e) and (f) shows the ARPES spectra around the Γ point, where the VBM was found to be located below E_F. The schematic electronic structure thus obtained is shown in Fig. 1.8(g). The results cannot be explained by the mean-field p-d Zener model [35], which states that the E_F crosses the Fermi level with holes in the host-derived valence band and that the ferromagnetic interaction is mediated by almost itinerant holes. This study has revealed that the p-d hybridized states do not merge with the valence band (if so the rigid band shift would be observed), but split off from the valence band. This means that the ferromagnetic interaction is mediated by holes weakly bound to Mn atoms or in p-d hybridized impurity bands.

In this thesis, we have taken the same approach to study the electronic structures and the origin of ferromagnetism of newly found Fe-doped ferromagnetic semiconductors.

1.3   Fe-doped Ferromagnetic Semiconductors

As discussed in the preceding section, most studies have been done on Mn-doped III-V compounds such as (Ga,Mn)As and (In,Mn)As. Those materials have two major problems for practical applications. First, only p-type conduction is possible since Mn atoms act as acceptors in III-V matrix. Second, the Curie temperature is lower than room temperature, 200 K at highest for (Ga,Mn)As [16].

Recently, Fe-doped semiconductors have been found to show ferromagnetism at relatively high temperatures attracting much interests. It has been demonstrated that they can potentially solve the above-mentioned problems that the Mn-doped FMSs have. First, various transport properties have been realized: n-type for (In,Fe)As:Be [36–39] and (In,Fe)Sb [40], p-type for (Ga,Fe)Sb [41–43] and Ge:Fe [44,45], and insulating for (Al,Fe)Sb [46]. Second, the Curie temperatures exceed room temperature: 340 K for (Ga,Fe)Sb with 25% Fe doping [43] and 335 K for (In,Fe)Sb with 16% Fe doping [40]. The basic physical properties of the Fe-doped FMSs with about 10% Fe doping are summarized in Table 1.1.

Table 1.1: Typical physical properties of the Fe-doped FMSs with the Fe content around 10%. Note that the Fe content x in Ge:Fe should be doubled when it is compared to that in III-V compounds.

Sample	Transport	x (%)	n (cm^{-3})	T_C (K)
(In,Fe)As:Be [38]	n-type	8.0	2.8×10^{19}	70
(Ga,Fe)Sb [43]	p-type	9.0	1.3×10^{19}	50
(Al,Fe)Sb [46]	insulating (p-type)	10.0	3.2×10^{17}	40
(In,Fe)Sb [40]	n-type	8.0		150
Ge:Fe [47]	p-type	6.5	2.7×10^{18}	35

1.3.1   (In,Fe)As:Be

Usually, the isoelectronic substitution of Fe^{3+} ions for the In atoms does not provide charge carriers, giving rise to Curie-Weiss paramagnetism [48]. However, Hai *et al.* have shown that by co-doping (In,Fe)As with Be atoms, which enter the interstitial sites and act as double donors, electrons are introduced and mediate ferromagnetic interaction between Fe atoms, and (In,Fe)As:Be becomes a new "n-type" III-V FMS. Here, unlike the Mn-doped materials, (In,Fe)As:Be has the advantage that one can control the concentration of magnetic ions and that of charge carriers independently.

Growth and Structural Characterizations

(In,Fe)As films can be grown by low-temperature molecular beam epitaxy (LT-MBE) (see ref. [38] for the details). A typical sample structure is shown in Fig. 1.9(a). A (In,Fe)As layer with or without Be atoms is grown on a GaAs(001) substrate with buffer layers in between, and covered by a InAs cap layer to prevent oxidation. For the substrate, one can also use InAs(001), and for the buffer layer, one can use (In$_{1-y}$,Ga$_y$)As or (Ga$_{1-z}$,Al$_z$)Sb layer to apply compressive or tensile strain, respectively [49].

Figure 1.9(b) shows a transmission electron microscopy (TEM) image of sample B0, In$_{0.909}$Fe$_{0.091}$As without Be co-doping, and Fig. 1.9(d) shows a high-resolution TEM lattice image of an area close to the buffer layer, indicated by a red rectangle in Fig. 1.9(b), where the inset shows a transmission electron diffraction (TED) pattern of this layer. The TEM and TED showed that the crystal structure is the zinc-blende-type without visible metallic Fe or inter metallic Fe-As precipitates in the entire (In,Fe)As layer. Figure 1.9(c) shows the atomic concentrations of the six areas indicated by $*$ in the TEM image obtained by energy dispersive x-ray spectroscopy (EDX). The amount of
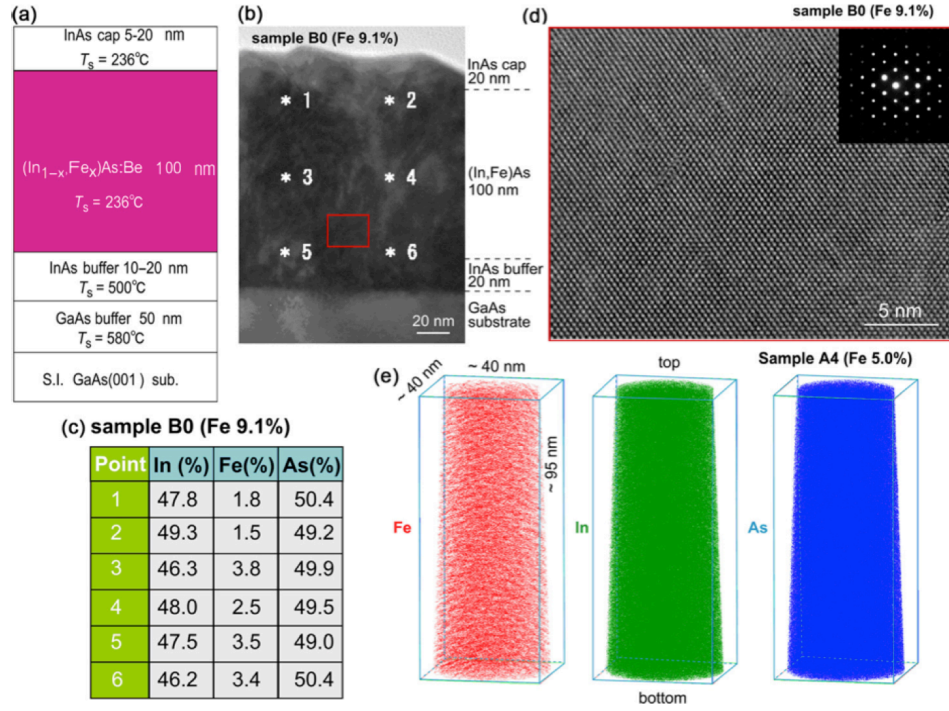
Figure 1.9: Sample characterization of (In,Fe)As [38]. (a) Sample structure. (b) TEM image of 100 nm thick $In_{0.909}Fe_{0.091}As$ layer grown on a GaAs substrate taken from the GaAs[110] direction. (c) Atomic concentrations of Fe, In and As obtained by energy dispersive x-ray spectroscopy (EDX) taken at 6 points marked by * in (b). (d) High-resolution TEM image of the area marked by the red rectangle in (b). (e) Three dimensional atom distribution of Fe, In, and As in a 100 nm-thick $In_{0.95}Fe_{0.05}As$ obtained by 3DAP. One dot corresponds to one atom.

As atoms was found to be equal to the sum of the amount of Fe and In atoms, which guarantees that doped Fe atoms are located at the In sites. Furthermore, the distribution of each element was investigated by laser-assisted three-dimensional atom probe (3DAP). The result is shown in Fig. 1.9(e), where it was found that the Fe atoms were distributed everywhere in the (In,Fe)As layer at least on the scale of a few tens of nanometers without any Fe-related precipitates. These careful structural analyses have confirmed that the ferromagnetism is intrinsic originating from Fe atoms incorporated into the InAs lattice, mainly substitutionally at the In sites.
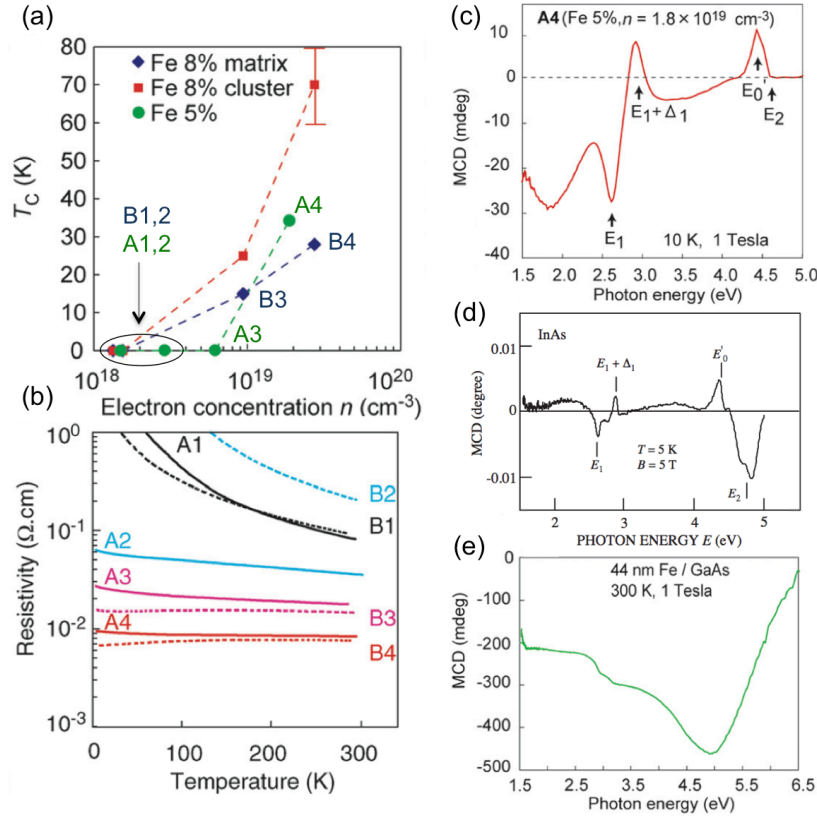
Figure 1.10: Transport and magneto-optical properties of (In,Fe)As [38]. (a) T_C as a function of electron concentration and (b) resistivity as a function of temperature for various samples with different Be contents. MCD spectra of (c) $In_{0.95}Fe_{0.05}As$ and (d) InAs [50]. E_1 (2.61 eV), $E_1 + \Delta_1$ (2.88 eV), E_0' (4.39 eV), and E_2 (4.74 eV) are optical critical point energies of InAs. (e) MCD spectrum of a 44 nm thick Fe thin film grown of a GaAs substrate.

Magnetism, Transport, and Magnet-optical Properties

Since Fe atoms are usually in the neutral state (Fe^{3+}), carriers are not provided. Actually, the electron concentration of $In_{0.909}Fe_{0.091}As$ without Be (sample B0) was estimated to be 1.6×10^{18} cm^{-3} four orders of magnitude smaller than the doped Fe concentration. On increasing the electron concentration by doping Be atoms, which enter interstitial sites and act as double donors, (In,Fe)As exhibits metal-insulator transition. The threshold electron concentration is about 1×10^{19} cm^{-3}, which is also the threshold for ferromagnetism as shown in Figs. 1.10(a) and (b). This suggests that (In,Fe)As is a n-type FMS, where ferromagnetic interactions are mediated by electron carriers.

Figures 1.10(c), (d) and (e) show the visible light magnetic circular dichro-

ism (MCD) spectra of ferromagnetic $In_{0.95}Fe_{0.05}As$ thin film, InAs thin film, and Fe metal thin film, respectively. MCD is a technique that measures the difference between the reflectivity for right $(R_{\sigma+})$ and left $(R_{\sigma-})$ circularly polarized light:

$$\text{MCD} = \frac{90}{\pi} \frac{(R_{\sigma+} - R_{\sigma-})}{2} \sim \frac{90}{\pi} \frac{\mathrm{d}R}{\mathrm{d}E} \Delta E, \tag{1.2}$$

where R denotes the reflectivity, E the photon energy, and ΔE the exchange-splitting energy (Zeeman energy) of a material. Since the MCD spectrum of a FMS directly reflects the spin-polarized band structure and its magnitude is proportional to the magnetization ($\Delta E \propto M$), MCD is a powerful and decisive tool to judge whether a FMS is intrinsic or not [51]. The spectral line shape of $In_{0.95}Fe_{0.05}As$ film is similar to that of InAs, and both spectra show peaks at the optical critical point energies of E_1 (2.61 eV), $E_1 + \Delta_1$ (2.88 eV), E'_0 (4.39 eV), and E_2 (4.74 eV), whereas the peak intensities are much higher in the ferromagnetic $In_{0.95}Fe_{0.05}As$ than the non-magnetic InAs. This suggests that there exists spin-splitting in the conduction and valence bands of the InAs host and that the ferromagnetism is intrinsic. In addition, the spectral line shape of (In,Fe)As is completely different from that of the Fe metal thin film.

The observations that the ferromagnetism appears at the boundary of metal insulator transition and that the MCD spectrum reflects the band structure of the host InAs suggests that the ferromagnetism is intrinsic and carrier-induced.

Magnetization Process

The magnetization process of (In,Fe)As:Be was investigated by x-ray magnetic circular dichroism (XMCD) [52]. XMCD is a suitable method to study the magnetization of a diluted magnetic thin film, because it is very sensitive and enabled one to deduce the intrinsic magnetization that does not contain diamagnetic signals from a substrate. The principles of XMCD will be given in Chapter 2.

Figure 1.11(a) shows the magnetization curves of a (In,Fe)As:Be thin film with 5% Fe measured at various temperature. Although the Curie temperature of the sample, where the hysteresis disappeared, was 15 K, the magnetization strongly responded to magnetic fields even at 260 K. This indicates that the existence of nanoscale ferromagnetic domains or superparamagnetism inside the sample. Indeed, the magnetization curves plotted against H/T fell onto one curve, following the Langevin function, except for the data at 20 K around which the macroscopic ferromagnetism starts to appear. By fitting the data to the summation of the Langevin function and a linear function representing superparamagnetism and paramagnetism, respectively, the average magnetic
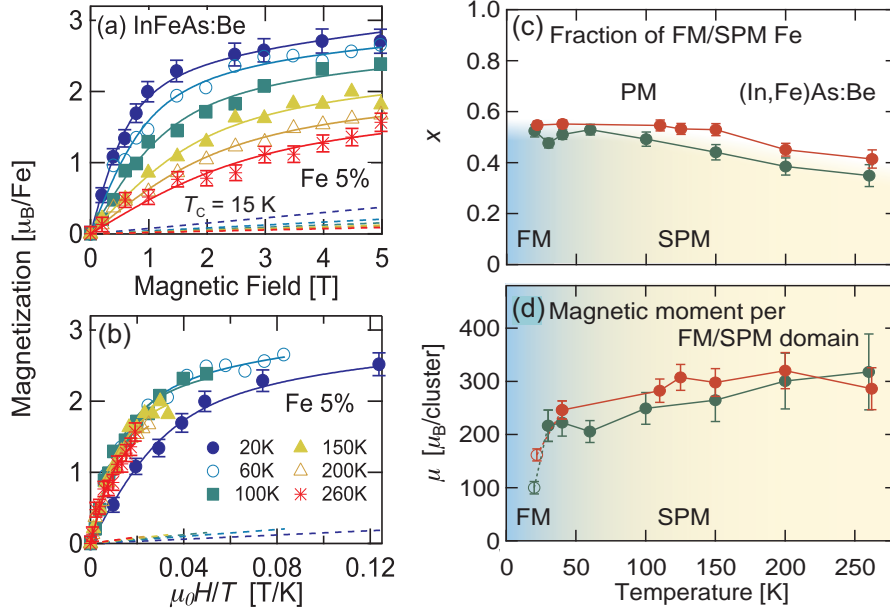
Figure 1.11: Magnetization of (In,Fe)As:Be with 5% Fe plotted against (a) magnetic fields and (b) $\mu_0 H/T$. (c) Fraction of Fe atoms participating in ferromagnetism or superparamagnetism. (d) Average magnetic moment of the nanoscale ferromagnetic domains. [52]

moment per nanoscale ferromagnetic domains was estimated to be 200-300 μ_B. The origin of such nanoscale ferromagnetic domains was attributed to the formation of Fe-rich regions on the nanometer scale during the material growth.

The XMCD study on (Al,Fe)Sb and (Ga,Fe)Sb will be presented in Chapters 3 and 5, respectively.

1.3.2   (Ga,Fe)Sb

(Ga,Fe)Sb is a p-type ferromagnetic semiconductor, whose Curie temperature is 340 K at highest exceeding room temperature. (Ga,Fe)Sb films can be grown by low-temperature molecular beam epitaxy (LT-MBE) (see ref. [43] for the details), and the typical sample structure is illustrated in Fig. 1.12(a). The TEM image in Fig. 1.12 shows that there are no Fe-related intermetallic precipitates and that Fe atoms are incorporated into zinc-blende GaSb lattice.

Being similar to the case of (In,Fe)As:Be, the MCD spectra shown in Fig. 1.12(c) have strong peaks at the optical critical points of GaSb. This again suggests that the ferromagnetism is intrinsic originating from the Fe atoms in the GaSb matrix.

Figure 1.12: (a) Sample structure of (Ga,Fe)Sb thin films. (b) High-resolution scanning TEM image of the 100-nm-thick (Ga,Fe)Sb layer with 13.7% Fe projected along the [110] axis. (c) MCD spectra measured at 5 K and 1 T. (d) Normalized magnetic field dependences of MCD, magnetization, and AHE measured on the sample with 13.7% Fe. (e) Curie temperature as a function of Fe content. [42]

Figure 1.12 (d) shows the normalized hysteresis curves measured using SQUID. MCD, and anomalous Hall effect (AHE). Their almost identical line shapes gurantee the single ferromagnetic phase in the sample. In addition to the AHE, negative magneto-resistance was observed, both of which suggests that the ferromagnetism and the carrier transport are related with each other. The hole concentration increased monotonically from 4.4×10^{18} cm^{-3} to 4.6×10^{19} cm^{-3} when the Fe content increased from 3.9% to 13.7% [43]. Accordingly, the T_C increased from 20 K to 140 K as shown in Fig. 1.12(e). Further increase of Fe content up to 25% results in the T_C of 340 K. Note that the carrier concentration is two orders of magnitude smaller than the doped Fe content, and the source of carriers has been attributed to native defects of GaSb.

1.3.3   (Al,Fe)Sb

(Al,Fe)Sb is a insulating ferromagnetic semiconductor [46]. The sample structure and the actual TEM image are shown in Figs. 1.13(a) and (b), respectively. Here, again, it was demonstrated that there are no intermetallic precipitates in (Al,Fe)Sb samples.
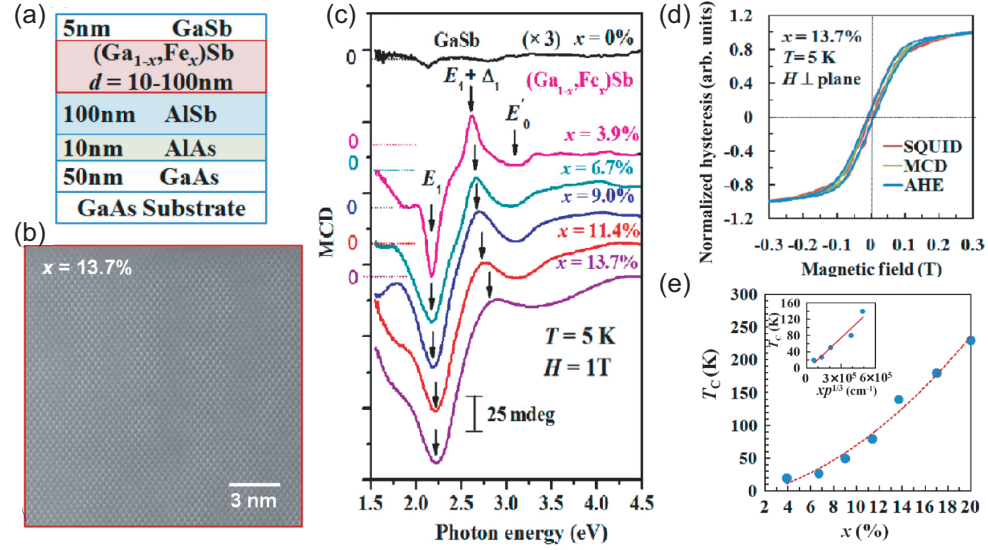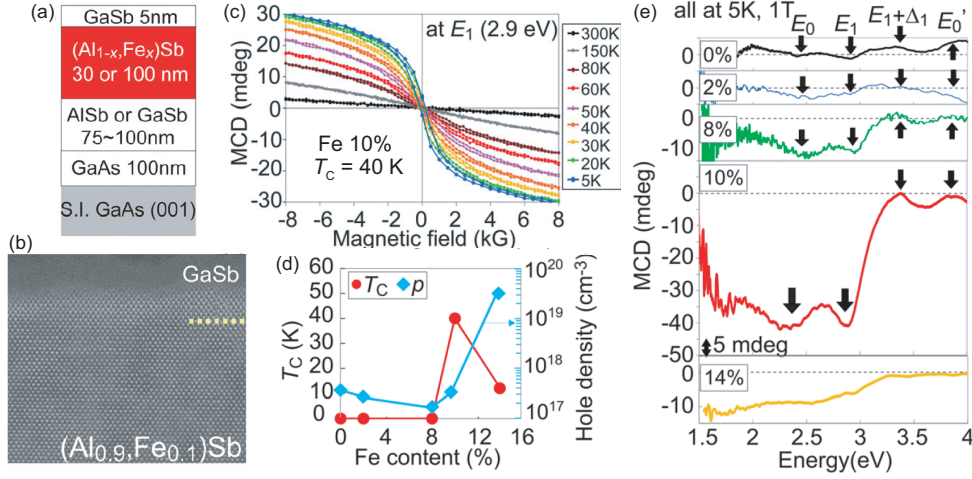
Figure 1.13: (a) Sample structure of (Al,Fe)Sb thin films. (b) High-resolution scanning TEM image of the sample with 10% Fe. (c) Magnetic field dependence of MCD intensity of the sample with 10% Fe at the E_1 position measured at various temperatures. (d) Curie temperature and hole concentration plotted against Fe content. (e) MCD spectra measured at 5K and 1T. [46]

Figure 1.13 shows the Curie temperature and the hole concentration of (Al,Fe)Sb films as a function of Fe content. Interestingly, the system remains almost paramagenetic up to 8% Fe doping, but suddenly becomes ferromagnetic ($T_C = 40$ K) with 10% Fe doping. The carrier concentration remains as low as the order of 10^{17} cm^{-3} in that doping range. Further increase of Fe content up to 14% leads to the decrease in T_C down to 10 K and to the increase in carrier concentration by the two order of magnitudes. This behavior was attributed to the degradation of the sample quality.

The MCD spectra of (Al,Fe)Sb (Fig. 1.13(e)), which behaves similarly to those of (In,Fe)As and (Ga,Fe)Sb, indicates that the ferromagnetism is intrinsic. Figure 1.13(c) shows the magnetic field dependence of MCD intensity of the sample with 10% Fe at E_1 position. Although the T_C is 40 K, the MCD intensity seems very responsive to magnetic fields even above T_C, which implies the existence of nanoscale ferromagnetic order as seen in (In,Fe)As:Be. In Chapter 3, more quantitative XMCD study on (Al,Fe)Sb, done for the purpose of investigating this magnetization process, will be presented.

1.3.4   (In,Fe)Sb

Very recently, it has been reported that (In,Fe)Sb thin films exhibit ferromagnetism above room temperature [40,53]. The T_C reaches 335 K with 16% Fe
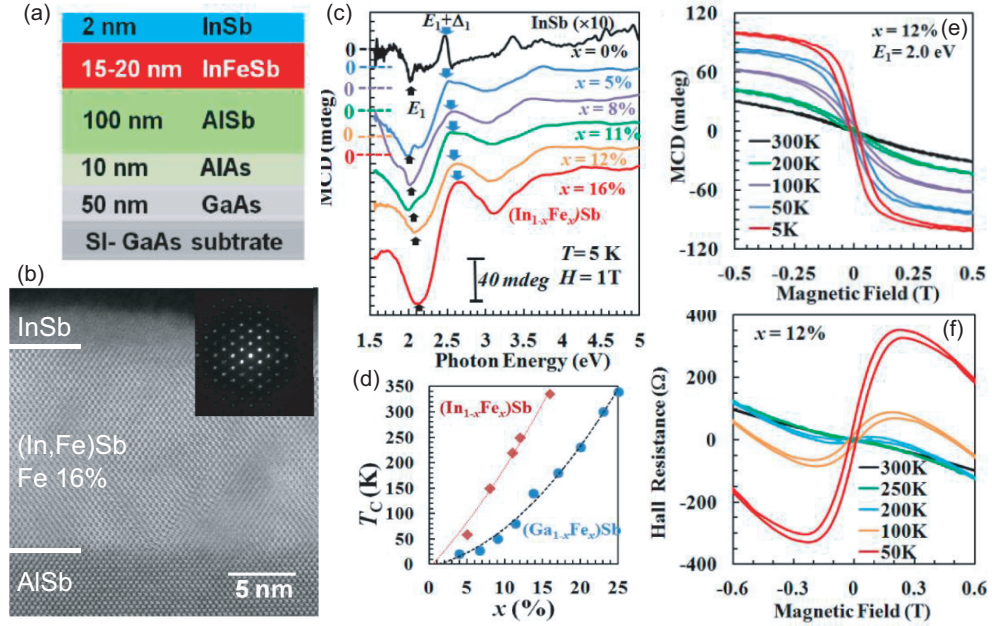
Figure 1.14: (a) Sample structure of (In,Fe)Sb thin films. (b) Cross-sectional scanning TEM image of the 15-nm-thick (In,Fe)Sb layer with 16% Fe. The inset shows the TED pattern. (c) MCD spectra measured at $T = 5$ K and $H = 1$ T. (d) Fe content dependence of the Curie temperatures of (In,Fe)Sb thin films in comparison with (Ga,Fe)Sb. (e) Magnetic field dependence of MCD intensity at E_1 position measured at various temperatures. (f) Hall resistance versus magnetic fields. [40]

doping [40], which is higher than that of (Ga,Fe)Sb with the same Fe content as shown in Fig. 1.14(d). The sample structure is illustrated in Fig. 1.14(a). It is clear from the TEM image and the TED pattern shown in Fig. 1.14(b) that there are no Fe-related precipitates in the samples.

Figure 1.14(c) shows the MCD spectra, and their intensities at E_1 position as a function of magnetic fields are shown in Fig. 1.14(e). The magnetic field dependence of Hall resistance is also shown in Fig. 1.14(f), where anomalous Hall effect was clearly observed. Those data suggest that the ferromagnetism is intrinsic being similar to the other Fe-doped FMSs.

1.3.5   Ge:Fe

Ge:Fe is one of a few group-IV ferromagnetic semiconductor reported thus far [44]. It shows p-type conduction with the typical hole concentration of 10^{18}-10^{19} cm^{-3} [47]. The same kinds of figures are presented in Fig. 1.15 as the ones presented above. From crystallographic characterizations [45, 54], it was
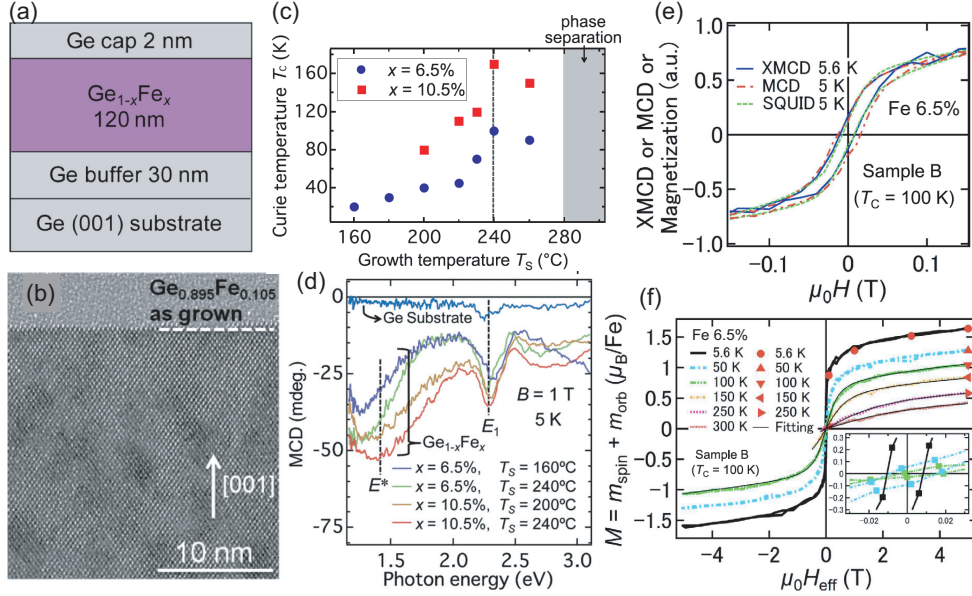
Figure 1.15: (a) Sample structure of Ge:Fe thin films. (b) High-resolution TEM image of $Ge_{0.895}Fe_{0.105}$ projected along the Ge [110] axis. [45] (c) Curie temperatures of Ge:Fe thin films with changing the growth temperature. (d) MCD spectra taken at $T = 5$ K and $H = 1$ T [54] (e) Magnetic field dependence of XMCD intensity, MCD intensity and magnetization. (f) Magnetization curves deduced using XMCD measured at various temperatures. [55]

confirmed that the Fe atoms reside in Ge matrix, where 85% of Fe atoms are located at the substitutional sites while 15% at the interstitial sites. The MCD spectra (Fig. 1.15(d)) and their magnetic field dependence in comparison with SQUID and XMCD (Fig. 1.15(e)) indicate that the ferromagnetism is intrinsic and has single-phase origin. The Curie temperature increases as the spatial distribution of Fe atoms becomes inhomogeneous, which can be controlled by annealing and growth temperatures as shown in Fig. 1.15(c). In addition, the magnetization showed superparamagnetic behavior even above T_C as revealed by the XMCD measurements [55] (Fig. 1.15(f)). This seems related to the inhomogeneous Fe distributions on the nanometer scale.

1.4   Objectives and Outlines of the Thesis

Although intriguing properties have been found in Fe-doped FMSs, there remain puzzles to solve. The most crucial one is the origin of the high-temperature ferromagnetism, which seems irrelevant to the transport properties. In the case of Mn-doped III-V FMSs, the ferromagnetic order is stabi-

lized by p-d exchange interaction, and the considerable amount of hole carriers (10^{20-21} cm^{-3}) is essential. In addition, it was expected that the Curie temperatures of n-type FMSs are significantly low compared to p-type FMSs because s-d exchange interaction is by far weaker than p-d exchange interaction. In the Fe-doped systems, however, not only p-type (Ga,Fe)Sb and Ge:Fe but also n-type (In,Fe)As and (In,Fe)Sb and insulating (Al,Fe)Sb show ferromagnetism at relatively high temperatures. Furthermore, the carrier concentrations are typically as low as 10^{17-19} cm^{-3}. The carrier-type variation could be understood if one assumes that the valence of Fe is 3+ in III-V semiconductor matrix. In such a case, Fe atoms would not provide carriers, and therefore, native defects would be responsible for carrier transport. However, this Fe^{3+} scenario would not explain the high temperature ferromagnetism especially in the n-type and insulating Fe-doped FMSs as mentioned above.

Thus far, we have found the superparamagnetic behavior well above T_{C} in (In,Fe)As:Be [52] and Ge:Fe [55] by XMCD measurements. Such superparamagnetic behavior seems universal for all the Fe-doped FMSs and would be a key to understand the ferromagnetism of the Fe-doped FMSs going beyond the classical p-d or s-d exchange model for carrier induced ferromagnetism.

In this thesis, we have studied the magnetic properties and electronic structures of the Fe-doped FMSs by using soft x-ray spectroscopies and first-principles calculations in order to address the above-mentioned issues. In Chapter 3, the magnetization process, or the superparamagnetic behavior, of (Al,Fe)Sb thin films were examined using XMCD. In Chapter 4, the electronic structure of Ge:Fe was investigated by SX-ARPES and first-principles supercell calculation. Chapter 5 presents the XMCD, resonance photoemission, and supercell calculation results of (Ga,Fe)Sb. In those Chapters, we have discussed the origin of the ferromagnetism and its relationship to the non-uniform distribution of Fe atoms on the nanoscale. Further calculations on other Fe-doped III-V semiconductors are introduced in Chapter 6, and the chemical trend, namely, the host-semiconductor dependence of electronic structure, has been investigated.

Chapter 2

Methods

2.1 X-ray Absorption Spectroscopy

X-ray absorption spectroscopy (XAS) is a core-level spectroscopic method, where a core electron is excited into empty states above the Fermi level. By using synchrotron radiation, one can get the absorption coefficient of the material as a function of photon energy as

$$\mu\left(\hbar\omega\right) \propto \sum_{f} |\langle f|\mathcal{H}_{int}|i\rangle|^2 \delta\left(E_f - E_i - \hbar\omega\right) \qquad (2.1)$$

where $\hbar\omega$ denotes the photon energy, $\mathcal{H}_{int}$ the electron-photon interaction operator, $|i\rangle$ and $|f\rangle$ the initial and final states, and $E_{i,f}$ the corresponding energies. Since the final states are unoccupied states reflecting the local environment around specific atom, XAS spectra provide element-specific information about the valence, spin state, orbital symmetry, crystal-field splitting, and the hybridization of atoms with their neighbors [56]. Especially, soft x-ray is very powerful to study the materials containing a $3d$ transition-metal element, because the photon energy covers the $L_{2,3}$ edges which are due to transition from $2p$ core level to the $3d$ valence level and have large cross section. In this thesis, I will focus on this soft x-ray absorption at the $L_{2,3}$ edges of $3d$ transition metals.

2.1.1 Measurements Modes

There are three ways to measure x-ray absorption, the transmission mode, the electron yield (EY) modes, and the fluorescence yield (FY) modes, schematically shown in Fig. 2.1. In the transmission mode, the intensity of transmitted x-ray through the sample is measured. Although transmission is the most direct way to measure absorption coefficient, it is not used in the soft x-ray
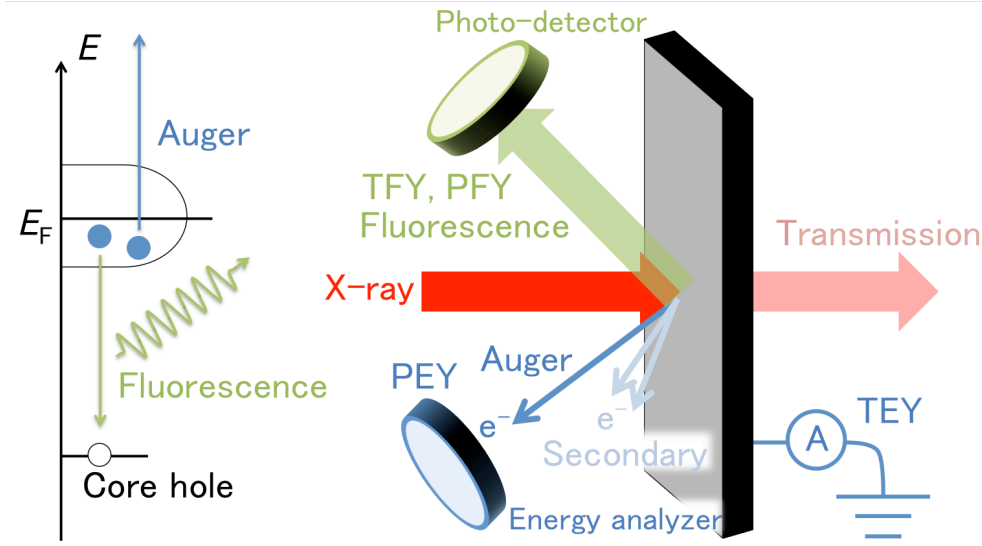
Figure 2.1: Schematic picture of XAS measurements. In order to obtain XAS spectra, transmission of incoming x-rays, or its decay products, electrons or fluorescence, are measured.

region because the attenuation length is so small that only ultra-thin samples of sub-micron thickness can be probed.

In the yield modes, which are more commonly employed, decay products such as electrons and fluorescence photons, which are created when a core-hole is filled by an electron having a lower binding energy, are counted. These techniques operate on the principle that the numbers of emitted decay products are proportional to the number of core-holes created in the photo-absorption process, and hence are proportional to the absorption cross section.

For EY modes, there are two methods to count the number of electrons. One is the partial electron yield (PEY) mode, where emitted Auger electrons are counted by an energy analyzer. For instance, PEY is employed to obtain the depth profile of electronic and magnetic states [57]. The other is the total electron yield (TEY) mode, where the compensation current flowing into the sample from ground are measured. Since Auger electrons produce a lot of secondary electrons through a cascade process, the use of TEY mode often results in a high S/N ratio. Therefore, the TEY mode is the most commonly used for XAS measurements. The EY modes are surface sensitive, probing the first 1-2 nm layer from the surface for PEY and ~ 5 nm for TEY, because the escape depth of electrons (a few nm) is much shorter than the penetration depth of incoming x-rays (~ 100 nm).

In the case of FY modes, the probing depth is much larger, as large as $\sim$

100 nm. FY is commonly measured as either total fluorescence yield (TFY), collecting photons of any energies, or as the partial fluorescence yield (PFY), collecting photons of certain energies. PFY mode is used in order to remove unwanted background radiation which may distort the spectra under interest. It is known that the spectra taken with FY modes suffer from "self-absorption effect", which suppresses the peak of the spectra and makes the FY spectra nonlinear with respect to the absorption coefficients [58]. This effect arises because the penetration depth of incoming x-ray is comparable to the escape depth of fluorescence light. Also in the case of EY modes, the same kind of effect happens, known as "saturation effect", when the incident angle is small so that the penetration depth become comparable to the escape depth of escaping electrons [59].

2.1.2 X-ray Absorption Cross-Section

The Hamiltonian including electromagnetic field of photons can be described using the vector potential $\boldsymbol{A}$ as

$$\mathcal{H} \;=\; \frac{1}{2m}\left(\boldsymbol{p} + e\boldsymbol{A}\right)^2 + V \tag{2.2}$$

$$=\; \mathcal{H}_0 + \frac{e}{2m}\left(\boldsymbol{A}\cdot\boldsymbol{p} + \boldsymbol{p}\cdot\boldsymbol{A}\right) + \frac{e^2}{2m}\boldsymbol{A}^2 \tag{2.3}$$

$$=\; \mathcal{H}_0 + \frac{e}{m}\boldsymbol{A}\cdot\boldsymbol{p} + \frac{i\hbar e}{2m}\left(\nabla\cdot\boldsymbol{A}\right) + \frac{e^2}{2m}\boldsymbol{A}^2 \tag{2.4}$$

since $[\boldsymbol{A}, \boldsymbol{p}] = i\hbar\nabla\cdot\boldsymbol{A}$. Taking Coulomb gauge ($\nabla\cdot\boldsymbol{A} = 0$) and ignoring the $\boldsymbol{A}^2$ term, the interaction operator $\mathcal{H}_{int}$ can be written as

$$\mathcal{H}_{int} = -\frac{e}{m}\boldsymbol{A}\cdot i\hbar\nabla. \tag{2.5}$$

Here, the vector potential satisfying $\Box\boldsymbol{A} = 0$ under the Coulomb gauge can be expressed as

$$\boldsymbol{A} = A_0 \; \boldsymbol{\epsilon} \; \mathrm{e}^{i(\boldsymbol{k}\cdot\boldsymbol{r} - \omega t)} \tag{2.6}$$

where $\boldsymbol{\epsilon}$ is the polarization vector. In soft-x-ray regions, the wave length ($\sim$ a few nm) is much larger than the radius of wave function of core electron, namely $\boldsymbol{k}\cdot\boldsymbol{r} \ll 1$, so the vector potential can be simplified as (electric dipole approximation)

$$\boldsymbol{A} = A_0 \; \boldsymbol{\epsilon} \; \mathrm{e}^{i(\boldsymbol{k}\cdot\boldsymbol{r} - \omega t)} \simeq A_0 \; \boldsymbol{\epsilon} \; \mathrm{e}^{-i\omega t}. \tag{2.7}$$

Considering the commutation relationship of $[\boldsymbol{r}, \mathcal{H}_0] = (i\hbar/m)\,\boldsymbol{p}$, the matrix element can be written as follows:

$$\langle f|\mathcal{H}_{int}|i\rangle = \langle f|\frac{e}{m}\boldsymbol{A}\cdot\boldsymbol{p}|i\rangle \tag{2.8}$$

$$= \frac{eA_0}{m}\langle f|\boldsymbol{\epsilon}\cdot\frac{m}{i\hbar}\left[\boldsymbol{r},\mathcal{H}_0\right]|i\rangle \tag{2.9}$$

$$= \frac{ieA_0}{\hbar}\left(E_f - E_i\right)\langle f|\boldsymbol{\epsilon}\cdot\boldsymbol{r}|i\rangle. \tag{2.10}$$

From the considerations above, the transition probability $W_{i,f}$, according to the Fermi's golden rule, can be written as

$$W_{i,f} = \frac{2\pi}{\hbar}|\langle f|\mathcal{H}_{int}|i\rangle|^2\delta\left(E_f - E_i - \hbar\omega\right) \tag{2.11}$$

$$= \frac{2\pi e^2 A_0{}^2\omega^2}{\hbar}|\langle f|\boldsymbol{\epsilon}\cdot\boldsymbol{r}|i\rangle|^2\delta\left(E_f - E_i - \hbar\omega\right) \tag{2.12}$$

Hence, the absorption cross section σ, which is defined as the ratio of the energy absorbed in a unit time to the photon flux, is given by

$$\sigma = \frac{absorbed\ energy}{photon\ flux} \tag{2.13}$$

$$= \frac{\hbar\omega\cdot W_{i,f}}{A_0{}^2\omega^2 c\ \varepsilon_0} \tag{2.14}$$

$$= 8\pi^2\alpha\hbar\omega|\langle f|\boldsymbol{\epsilon}\cdot\boldsymbol{r}|i\rangle|^2\delta\left(E_f - E_i - \hbar\omega\right) \tag{2.15}$$

where $\alpha = e^2/4\pi\varepsilon_0\hbar c$ is the fine structure constant.

2.2   X-ray Magnetic Circular Dichroism

X-ray magnetic circular dichroism (XMCD) is defined as the difference between XAS spectra taken with left- and right- circularly polarized light, schematically shown in Fig. 2.3. If there exists spin polarization in the valence states, XMCD has a finite value due to the different matrix elements between left- and right-circular polarizations. Since the spectra reflect the local environment of the atom as well as the valence and spin state of the atom, XMCD provides the unique information about the magnetic properties of the material in an element- and site-specific way. Utilizing these features, it is possible to study the magnetization process precisely. When measuring the magnetization of thin films by macroscopic magnetization measurements such as SQUID magnetometry, there are always contributions of the diamagnetic response from the substrate
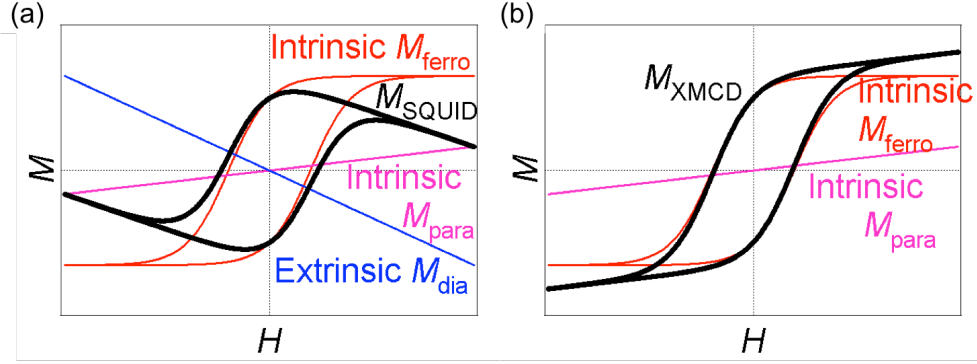
Figure 2.2: Schematic figures of magnetization curves measured with (a) SQUID and with (b) XMCD.

as shown in Fig. 2.2(a), which prohibit the extraction of the intrinsic paramagnetic component [60]. However, XMCD yields intrinsic magnetic properties and enables one to extract the paramagnetic component accurately as shown in Fig. 2.2(b).

XMCD experiments are frequently performed at the $L_{2,3}$ edges because it shows large dichroic signals compared to the K edge.

2.2.1 Two-Step Model: One Electron Approach

The simplest model to describe XMCD is the two-step model [61,62]. In this picture, the first step is to write the initial orbitals as spin-orbit split $2p$ wave functions, in the case of the $L_{2,3}$ edges, as shown in Table 2.1. The second step is to calculate the matrix elements for transitions to various $3d$ states.

Rewriting the polarization vector using spherical harmonics Y_{lm},

$$\boldsymbol{\epsilon} \cdot \boldsymbol{r} = (\epsilon_x \sin\theta\cos\phi + \epsilon_y \sin\theta\sin\phi + \epsilon_z \cos\theta)\, r \tag{2.16}$$

$$= \sqrt{\frac{4\pi}{3}} r \left(\epsilon_z Y_{10} + \frac{-\epsilon_x + i\epsilon_y}{\sqrt{2}} Y_{11} + \frac{-\epsilon_x + i\epsilon_y}{\sqrt{2}} Y_{1-1} \right), \tag{2.17}$$

where $\epsilon_+ = \frac{1}{\sqrt{2}}(-\epsilon_x + i\epsilon_y)$ and $\epsilon_- = \frac{1}{\sqrt{2}}(\epsilon_x + i\epsilon_y)$ correspond to left- and right-circular polarization, respectively, and the light travels along the z direction. In the atomic system, where the wave function can be given by n, l, and m, the matrix element can be separated into the angular part and radial part as

$$\langle f|\boldsymbol{\epsilon} \cdot \boldsymbol{r}|i\rangle = \sqrt{\frac{4\pi}{3}} \langle l_f, m_f| \left(\epsilon_z Y_{10} + \epsilon_+ Y_{11} + \epsilon_- Y_{1-1}\right)|l_i, m_i\rangle \mathcal{R}, \tag{2.18}$$

$$\mathcal{R} = \langle n_f, l_f|r|n_i, l_i\rangle. \tag{2.19}$$

Here, the selection rule can be deduced from the relation below, where Wigner 3-j symbols are employed,

$$\int Y_{l_1 m_1}^* Y_{l_2 m_2} Y_{l_3 m_3} \mathrm{d}\Omega = (-1)^{m_1} \sqrt{\frac{(2l_1 + 1)(2l_2 + 1)(2l_3 + 1)}{4\pi}}$$

$$\times \begin{pmatrix} l_1 & l_2 & l_3 \\ 0 & 0 & 0 \end{pmatrix} \begin{pmatrix} l_1 & l_2 & l_3 \\ -m_1 & m_2 & m_3 \end{pmatrix} \quad (2.20)$$

because the Wigner 3-j symbol becomes zero unless both $-m_1 + m_2 + m_3 = 0$ and $|l_1 - l_2| \leq l_3 \leq l_1 + l_2$ are satisfied. For example, in the case of electric dipole transition described by $Y_{1m'}$, only the transition with $\Delta l = 0, \pm 1$ and $\Delta m = m'$ is allowed.

Now the matrix element can be calculated for the transition with $\Delta l = 1$ and $\Delta m = \pm 1$ (circular polarization), which is under interest, as

$$T_{l_i, m_i}^{\pm} = \sqrt{\frac{4\pi}{3}} \langle l_f = l_i + 1, m_f = m_i \pm 1 | Y_{1\pm 1} | l_i, m_i \rangle \mathcal{R} \quad (2.21)$$

$$= (-1)^{l_i - m_i + 1} \sqrt{l_i + 1} \begin{pmatrix} l_i + 1 & 1 & l_i \\ -m_i \mp 1 & \pm 1 & m_i \end{pmatrix} \mathcal{R} \quad (2.22)$$

$$= \sqrt{\frac{(l_i \pm m_i + 2)(l_i \pm m_i + 1)}{2(2l_i + 3)(2l_i + 1)}} \mathcal{R}. \quad (2.23)$$

The probabilities $\left(T_{1,m}^{\pm}/\mathcal{R}\right)^2$ of $p \to d$ transition are summarized in the right two columns of Table. 2.1 and also shown in the Fig. 2.3(b). From this table, it can be known that left-circularly polarized x-rays preferentially emits spin-up electrons (5/8 times) at the L_3 edge and spin-down electrons (3/4 times) at the L_2 edge. Therefore, the absorption of the left-circularly polarized x-rays becomes larger at the L_3 edge and smaller at the L_2 edge for the spin polarization $P = (n_{h\uparrow} - n_{h\downarrow})/(n_{h\uparrow} + n_{h\downarrow})$, where n_h denote the number of holes. This is the simplest explanation how XMCD provides the information about the magnetism of the materials.

For example, in the case where the spin-up states are completely occupied and only spin-down states are available, i.e. $P = -1$, the intensities at the $L_{2,3}$ edges with two circular polarizations can be calculated by summing over $m = -2$ to 2:

$$I_{L_3}^+ = \sum_{i,f} |\langle f | \sqrt{\frac{4\pi}{3}} r Y_{11} | i \rangle|^2 = \frac{1}{3}\mathcal{R}^2, \ I_{L_3}^- = \frac{5}{9}\mathcal{R}^2 \quad (2.24)$$

Table 2.1: Initial core p states in the presence of the spin-orbit interaction are shown in the left two columns. On the right hand side, the transition probabilities are shown for both left- and right- circular polarization, where the subscripts denote m_l and m_s of the final state. [62]

$\lvert J, M\rangle$	$\lvert m_l, m_s\rangle$ $(l=1)$	$\left(T_{1,m}^{+}/\mathcal{R}\right)^2$	$\left(T_{1,m}^{-}/\mathcal{R}\right)^2$
$\lvert\frac{3}{2},\frac{3}{2}\rangle$	$\lvert+1,\uparrow\rangle$	$\left(\frac{2}{5}\right)_{2,\uparrow}$	$\left(\frac{1}{15}\right)_{0,\uparrow}$
$\lvert\frac{3}{2},\frac{1}{2}\rangle$	$\sqrt{\frac{1}{3}}\lvert 1,\downarrow\rangle+\sqrt{\frac{2}{3}}\lvert 0,\uparrow\rangle$	$\left(\frac{2}{15}\right)_{2,\downarrow},\left(\frac{2}{15}\right)_{1,\uparrow}$	$\left(\frac{1}{45}\right)_{0,\downarrow},\left(\frac{2}{15}\right)_{-1,\uparrow}$
$\lvert\frac{3}{2},-\frac{1}{2}\rangle$	$\sqrt{\frac{2}{3}}\lvert 0,\downarrow\rangle+\sqrt{\frac{1}{3}}\lvert-1,\uparrow\rangle$	$\left(\frac{2}{15}\right)_{1,\downarrow},\left(\frac{1}{45}\right)_{0,\uparrow}$	$\left(\frac{2}{15}\right)_{-1,\downarrow},\left(\frac{2}{15}\right)_{-2,\uparrow}$
$\lvert\frac{3}{2},-\frac{3}{2}\rangle$	$\lvert-1,\downarrow\rangle$	$\left(\frac{1}{15}\right)_{0,\downarrow}$	$\left(\frac{2}{5}\right)_{-2,\downarrow}$
$\lvert\frac{1}{2},\frac{1}{2}\rangle$	$\sqrt{\frac{2}{3}}\lvert 1,\downarrow\rangle+\sqrt{\frac{1}{3}}\lvert 0,\uparrow\rangle$	$\left(\frac{4}{15}\right)_{2,\downarrow},\left(\frac{1}{15}\right)_{1,\uparrow}$	$\left(\frac{2}{45}\right)_{0,\downarrow},\left(\frac{1}{15}\right)_{\lvert-1,\uparrow}$
$\lvert\frac{1}{2},-\frac{1}{2}\rangle$	$\sqrt{\frac{1}{3}}\lvert 0,\downarrow\rangle+\sqrt{\frac{2}{3}}\lvert-1,\uparrow\rangle$	$\left(\frac{1}{15}\right)_{1,\downarrow},\left(\frac{2}{45}\right)_{0,\uparrow}$	$\left(\frac{1}{15}\right)_{-1,\downarrow},\left(\frac{4}{15}\right)_{-2,\uparrow}$

$$I_{L_2}^{+}=\frac{1}{3}\mathcal{R}^2,\ \text{and}\ I_{L_2}^{-}=\frac{1}{9}\mathcal{R}^2 \qquad (2.25)$$

Therefore the XMCD intensity can be calculated to be $\Delta I_{L_3}=I_{L_3}^{+}-I_{L_3}^{-}=-(2/9)\mathcal{R}^2$ at the L_3 edge and $\Delta I_{L_2}=(2/9)\mathcal{R}^2$ at the L_2 edge.

2.2.2   XMCD Sum Rules

In 1992 and 1993, Thole and Carra derived the formulae to calculate the orbital magnetic moment and spin magnetic moment from the integrated spectra of XAS and XMCD, which is called XMCD sum rules [64, 65] and schematically shown in Fig. 2.3(c). The equations for the transition from the spin-orbit-split core state $c\pm\frac{1}{2}$ into the valence shell $l=c\pm 1$ occupied by n electrons are

$$\frac{\int_{L_3+L_2}(\mu^{+}-\mu^{-})\,\mathrm{d}\omega}{\int_{L_3+L_2}(\mu^{+}+\mu^{-}+\mu^{0})\,\mathrm{d}\omega}=\frac{l(l+1)+2-c(c+1)}{2l(l+1)(4l+2-n)}\langle L_z\rangle, \qquad (2.26)$$

$$\frac{\int_{L_3}(\mu^{+}-\mu^{-})\,\mathrm{d}\omega-\frac{c+1}{c}\int_{L_2}(\mu^{+}-\mu^{-})\,\mathrm{d}\omega}{\int_{L_3+L_2}(\mu^{+}+\mu^{-}+\mu^{0})\,\mathrm{d}\omega}=\frac{l(l+1)-2-c(c+1)}{3c(4l+2-n)}\langle S_z\rangle$$

$$+\frac{l(l+1)\{l(l+1)+2c(c+1)+4\}-3(c-1)^2(c+2)^2}{6lc(l+1)(4l+2-n)}\langle T_z\rangle \qquad (2.27)$$
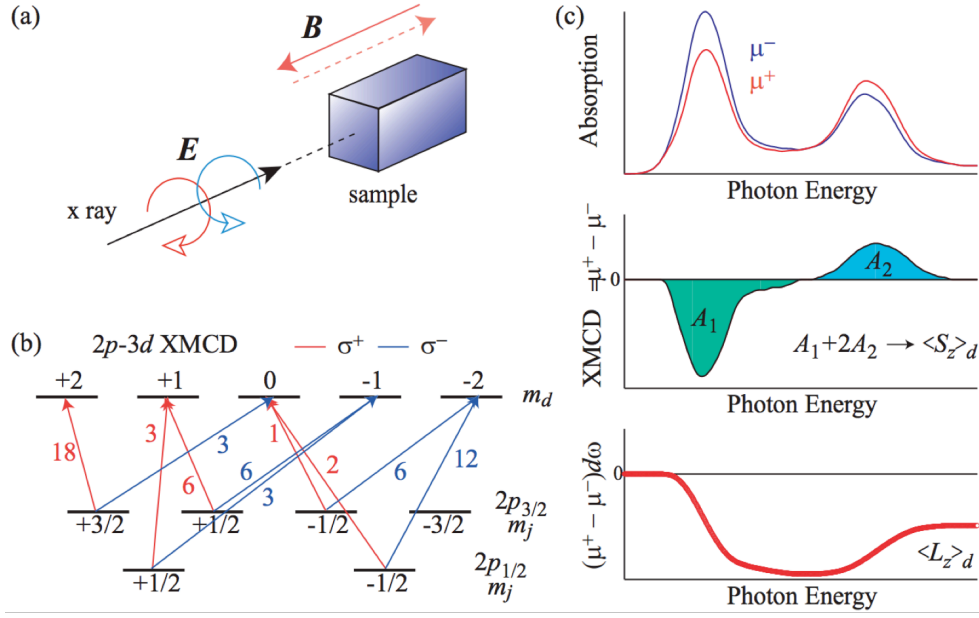
Figure 2.3: Schematic diagram of XMCD [63]. (a) Experimental setup for XMCD measurements. (b) Transition probability of $2p \rightarrow 3d$ absorption with left- and right- circularly polarized x-rays, σ. Note that the $3d$ states shown here are spin-up states. (c) XAS spectra taken with circularly polarized x-rays, and resulting XMCD and integrated XMCD spectra. μ^+ and μ^- denote the absorption of the left- and right- circular polarized x-rays, respectively.

where μ^+, μ^- and μ^0 denote the absorption of the x-rays with the polarization ϵ_+, ϵ_-, and ϵ_z (look at eq.(2.19)), and $\langle T_z \rangle$ denotes the expectation value of the magnetic dipole operator $\boldsymbol{T} = \sum_i \boldsymbol{S}_i - 3\hat{\boldsymbol{r}}_i (\hat{\boldsymbol{r}}_i \cdot \boldsymbol{S}_i)$, expressing the asphericity of the spin distribution in the valence shell.

For the $2p \rightarrow 3d$ transition, assuming $\mu_0 = (\mu_+ + \mu_-)/2$, the sum rules, which one often finds in literatures, can be written as

$$\langle L_z \rangle = \frac{4}{3} n_h \frac{\int_{L_3 + L_2} (\mu^+ - \mu^-) \, \mathrm{d}\omega}{\int_{L_3 + L_2} (\mu^+ + \mu^-) \, \mathrm{d}\omega} \tag{2.28}$$

$$2\langle S_z \rangle + 7\langle T_z \rangle = 2n_h \frac{\int_{L_3} (\mu^+ - \mu^-) \, \mathrm{d}\omega - 2 \int_{L_2} (\mu^+ - \mu^-) \, \mathrm{d}\omega}{\int_{L_3 + L_2} (\mu^+ + \mu^-) \, \mathrm{d}\omega}, \tag{2.29}$$

where n_h ($= 10 - n$) represent the number of holes in the valence shell. Since it is known that $\langle T_z \rangle$ is negligibly small in the system with high symmetry such as T_d and O_h [66], spin magnetic moment as well as orbital magnetic moment can be obtained in most three dimensional bulk materials. In addition, the ratio of the spin magnetic moment to the orbital magnetic moment can be obtained

Table 2.2: Correction factors $\langle SE_z \rangle_{\text{sum}}/\langle SE_z \rangle$ for Ni, Co, Fe, and Mn with various valence states, and the expectation values of the orbital moment L_z, spin moment S_z, and the magnetic dipole operator T_z. n denotes the number of electrons in the d shell. [68]

Element	n	$\langle L_z \rangle$	$\langle S_z \rangle$	$\langle T_z \rangle$	$\langle SE_z \rangle_{\text{sum}}/\langle SE_z \rangle$
Ni^{2+}	8	-0264	-0.995	-0.00291	0.921
Ni^{3+}	7	-0.788	-0.969	0.00491	0.923
Co^{2+}	7	-0.812	-1.01	0.00452	0.921
Co^{3+}	6	-7.11	-1.65	0.0195	0.874
Fe^{2+}	6	-0.736	-1.69	0.0126	0.875
Fe^{3+}	5	-0.002	-2.50	0.00048	0.685
Mn^{2+}	5	-0.002	-2.50	0.00031	0.680
Mn^{4+}	3	0.176	-1.50	0.00015	0.587

without the knowledge of the value of n_h.

Experimentally, in 1995, Chen *et al.* proved the validity of XMCD sum rules by measuring very thin Fe and Co films with transmission mode, where the deduced spin and orbital magnetic moments show excellent agreement with those obtained by gyromagnetic ratio measurements [67].

2.2.3   Correction Factor for the Spin Sum Rule

In order to use the spin sum rule for the $L_{2,3}$ edges, one has to assume that the L_3 and the L_2 edges are not mixed and well separated in energy, because otherwise there is no clear method to divide the spectrum into L_3 and L_2. This assumption is not always the case especially for early transition metals such as V and Cr, where the spin-orbit splitting of the $L_{2,3}$ edges is relatively small. Therefore, in general, the effective spin moment, $\langle SE_z \rangle = \langle S_z \rangle + 7/2\langle T_z \rangle$, deduced from the spin sum rule $\langle SE_z \rangle_{\text{sum}}$, is different from the actual expectation value $\langle SE_z \rangle$.

In 1996, Teramura *et al.* [68] estimated the correction factor $\langle SE_z \rangle_{\text{sum}}/\langle SE_z \rangle$ for the late transition metals from Mn to Ni in order to deduce the actual spin magnetic moment from the spin sum rule on the basis of an atomic model including the full multiplet and the crystal field with O_h symmetry. The results are summarized in Table 2.2, where it was assumed that 10Dq = 1.5 eV. Note that It is difficult to estimate the correction factors for elements with d electrons less than 5 such as Mn^{3+}, V, and Cr, and hence one need to be careful to analyze the XMCD data of light transition-metal elements.

The discrepancy between $\langle SE_z \rangle_{\text{sum}}$ and $\langle SE_z \rangle$ is caused by the final-state

effects: a significant overlap of the wave functions of the $2p$ hole and the $3d$ hole, so-called multiplet effects [69]. The multiplet effects are hardly screened in solids, while the core hole potential is largely screened.

2.3   Photoemission Spectroscopy

Photoemission spectroscopy (PES) is a very powerful and direct technique to study the electronic structures of materials. Basic principles are described below. When photons hit a sample, photoelectrons come out. Due to the conservation of energy, the kinetic energy of the photoelectron satisfies the following relation,

$$E_{\mathrm{kin}}^{\mathrm{vac}} = \hbar\omega - E_B - \phi, \qquad (2.30)$$

where $\hbar\omega$ is the photon energy, E_B the binding energy relative to the Fermi level (E_{F}), and $\phi = E_{\mathrm{vac}} - E_{\mathrm{F}}$ the work function. The binding energy thus can be obtained as

$$E_B = \hbar\omega - E_{\mathrm{kin}}^{\mathrm{vac}} - (E_{\mathrm{vac}} - E_{\mathrm{F}}) = \hbar\omega - E_{\mathrm{kin}}, \qquad (2.31)$$

where the kinetic energy E_{kin} measured from the Fermi level is directly observed in real experiment. Practically, by measuring a Au spectrum which is in contact with the sample and has a clear Fermi edge, one can identify the Fermi level of the system and hence the binding energy of electrons inside the sample.

If the sudden removal of an electron does not change the wave function of the other N-1 electrons (one-electron approximation), $-E_B$ is equal to the energy ϵ_k of the initial Bloch state. If this is the case, the photoemission spectrum directly reflects the density of states $N(E)$ of the system.

$$I(E_B) \propto \sum_k \delta(E_B + \epsilon_k) \propto N(-E_B). \qquad (2.32)$$

In real systems, because the wave function of N-1 electrons relaxes by the creation of a photo-hole, E_B is given by the energy difference between the N-electron initial state and the N-1 electron final state. Therefore, analyzing the photoemission spectra gives various information such as the strength of electron correlation and charge-transfer effect.
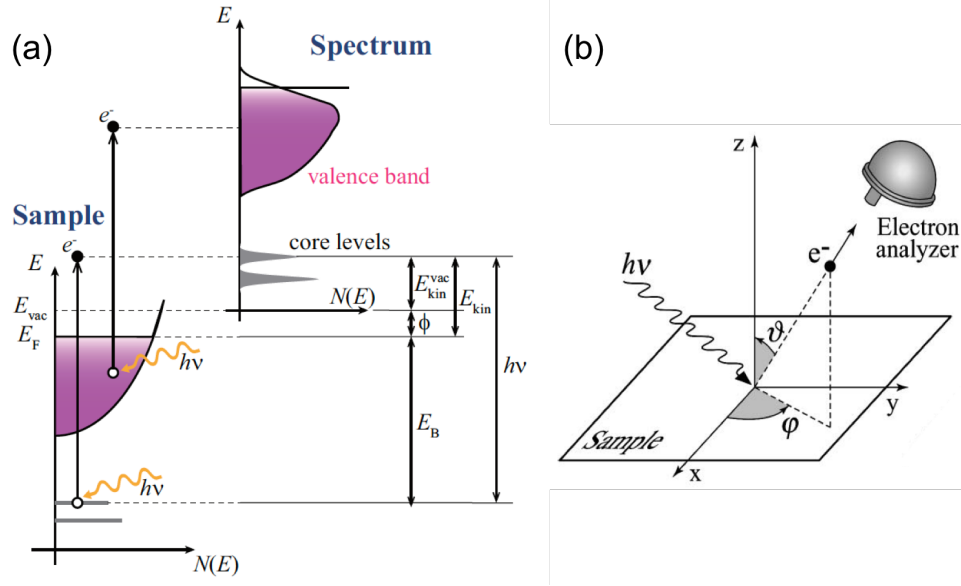
Figure 2.4: (a) Schematic illustration of PES [70]. Here, the relationship between the energy levels in a solid and the PES spectrum is shown. (b) Geometry of ARPES measurements [71].

2.3.1 Angle-resolved Photoemission Spectroscopy

In the preceding section, only the kinetic energy of the photoelectron and energy conservation are discussed. In angle-resolved photoemission spectroscopy (ARPES), the emission angle of photoelectrons is also measured. The measurement geometry is shown in Fig. 2.4(b). The momentum of photoelectron can be obtained as

$$p_x = \sqrt{2m_e E_{\text{kin}}^{\text{vac}}} \sin \vartheta \cos \varphi, \tag{2.33}$$

$$p_y = \sqrt{2m_e E_{\text{kin}}^{\text{vac}}} \sin \vartheta \sin \varphi, \tag{2.34}$$

$$p_z = \sqrt{2m_e E_{\text{kin}}^{\text{vac}}} \cos \vartheta. \tag{2.35}$$

Assuming that an electron with the crystal momentum $\boldsymbol{K}_i = (K_{i,x}, K_{i,y}, K_{i,z})$ is photo-excited into a free-electron-like band with the bottom energy E_0, the wave vector of the final state $\boldsymbol{K}_f = (K_{f,x}, K_{f,y}, K_{f,z})$ and the energy of the electron E can be written as

$$\boldsymbol{K}_f = \boldsymbol{K}_i + \boldsymbol{G} + \boldsymbol{k}_{\hbar\omega}, \tag{2.36}$$

$$E = \frac{\hbar^2}{2m}(K_{f,x}^2 + K_{f,y}^2 + K_{f,z}^2) - E_0 \ (= \hbar\omega - E_B), \tag{2.37}$$

where $\boldsymbol{G}$ is a reciprocal lattice vector and $\boldsymbol{k}_{\hbar\omega}$ the wave vector of photon. Note that $\boldsymbol{k}_{\hbar\omega}$ is usually negligible in VUV-ARPES but has a finite contribution in soft x-ray ARPES measurements.

When the excited electron is emitted to the vacuum, the parallel component of momentum is conserved due the translational symmetry.

$$p_x = \hbar K_{f,x}, \tag{2.38}$$
$$p_y = \hbar K_{f,y}. \tag{2.39}$$

Using those relationships, the band structure, namely, E_B-$\boldsymbol{K}_i$ relationship, can be obtained as

$$\hbar K_{i,x} = \sqrt{2m(E_B + h\nu - \phi)} \sin\vartheta \cos\varphi, \tag{2.40}$$
$$\hbar K_{i,y} = \sqrt{2m(E_B + h\nu - \phi)} \sin\vartheta \sin\varphi, \tag{2.41}$$
$$\hbar K_{i,z} = \sqrt{2m[(E_B + h\nu - \phi)\cos^2\vartheta + V_0]}. \tag{2.42}$$

Here $V_0 = E_0 + \phi$ is called "inner potential", which is material dependent. Experimentally, V_0 can be determined from the symmetry of the photon-energy-dependence of ARPES spectra. Note that the assumption Eq. 2.37 is not necessary to obtain Eqs. 2.40 and 2.41.

2.3.2   Resonance Photoemission Spectroscopy

When the used photon energy is in the vicinity of an absorption edge, one can enhance the signal from the orbital at which absorption occurs. Because thus obtained enhanced spectrum corresponds to the partial density of states (PDOS) of the specific orbital, resonance photoemission spectroscopy (RPES) has been widely used to study the element-specific electronic structure of materials [33, 72–76]. The basic principle is described below.

The direct photoemission process can be written as

$$|\Psi_g(N)\rangle + \hbar\omega \xrightarrow{V_{\mathrm{rad}}} |\Psi_f(N-1), \phi_k\rangle, \tag{2.43}$$

where $\Psi_g(N)$ denotes the ground state with N valence electrons and eigenenergy E_g, $\Psi_f(N-1)$ a final state with N-1 valence electrons and eigenenergy E_f, and ϕ_k the state of a photoelectron with energy ϵ_k measured relative to E_{F}. Here, energy conservation gives $\epsilon_k = \hbar\omega + E_g - E_f$. The signal intensity
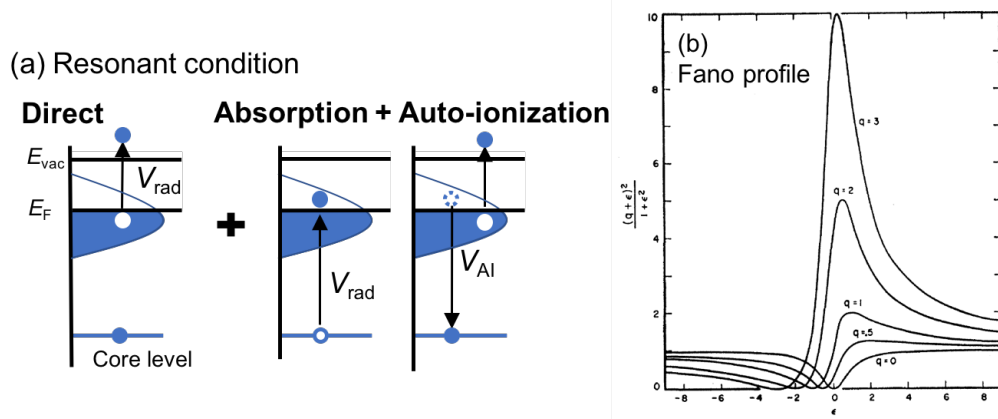
Figure 2.5: (a) Schematic illustration of resonance-photoemission process. (b) Simulated Fano profile with various values of asymmetry parameter q [77].

from photoelectron with the energy of ϵ_k is given by

$$I(\epsilon_k, \omega) \propto \sum_f |\langle \Psi_g(N)| T(\omega) |\Psi_f(N-1), \phi_k\rangle|^2 \delta(\hbar\omega + E_g - E_f - \epsilon_k), \quad (2.44)$$

where $T(\omega)$ is the transition operator. In the direct photoemission, the transition operator $T^{\mathrm{PES}}(\omega)$ is given by $V_{\mathrm{rad}} = \frac{e}{m}\boldsymbol{A} \cdot \boldsymbol{p}$ as in Eq. 2.9. When the used photon energy is in the vicinity of an absorption edge, another process can occur in addition to the direct photoemission as follows.

$$|\Psi_g(N)\rangle + \hbar\omega \xrightarrow{V_{\mathrm{rad}}} |\Psi_m(\underline{c}, N+1)\rangle \xrightarrow{V_{\mathrm{AI}}} |\Psi_f(N-1), \phi_k\rangle, \quad (2.45)$$

where $\Psi_m(\underline{c}, N+1)$ is the intermediate state with a core hole and N+1 valence electrons and with eigenenergy E_m. In this process, photo-absorption from a core level to a valence state takes place followed by auto-ionization process. Since the resonance process has the same final state as the direct photoemission process, quantum-mechanical interfere will occur. Including this resonance channel, the transition operator can be written to the lowest order [78, 79] as

$$T^{\mathrm{RPES}}(\omega) = V_{\mathrm{rad}} + V_{\mathrm{AI}} \sum_m \frac{|\Psi_m\rangle \langle \Psi_m|}{\hbar\omega + E_g - E_m + i\Gamma_m} V_{\mathrm{rad}}, \quad (2.46)$$

where $V_{\mathrm{AI}} = \mathrm{e}^2/r$ is the Coulomb interaction responsible for the auto-ionization, Γ_m is the spectral width of the intermediate state $|\Psi_m\rangle$. The second term contributes to the photoemission intensity significantly when the photon energy is close to an absorption edge and the denominator $\hbar\omega + E_g - E_m + i\Gamma_m$ becomes

very small. This interference gives characteristic Fano profile [77] as a function
of photon energy, which is

$$\frac{|\langle \Psi_g(N)| T^{\mathrm{RPES}}(\omega) |\Psi_f(N-1), \phi_k\rangle|^2}{|\langle \Psi_g(N)| T^{\mathrm{PES}}(\omega) |\Psi_f(N-1), \phi_k\rangle|^2} = \frac{q+\epsilon}{1+\epsilon^2}. \tag{2.47}$$

Here, $E = (\hbar\omega - E_m)/\Gamma_m$ and q is the dimensionless Fano asymmetry parame-
ter. Simulated Fano profiles with various values of q are shown in Fig. 2.5(b),
where photoemission intensity shows a sharp increase at the threshold of an
absorption edge.

2.4   Density Functional Theory

In this section, the basics of the density functional theory (DFT) calculation
is introduced. The hamiltonian of solids is generally given by

$$\mathcal{H} = \sum_j^N [-\nabla^2 + V_{\mathrm{ion}}(\boldsymbol{r}_j)] + \frac{1}{2}V_{ee}, \tag{2.48}$$

where $V_{\mathrm{ion}}(\boldsymbol{r})$ is the Coulomb interaction between electrons and nuclei, and V_{ee}
the interaction between electrons.

$$V_{\mathrm{ion}} = -\sum_I \frac{Z_I e^2}{|\boldsymbol{r}_j - \boldsymbol{R}_I|}, \quad V_{ee} = \sum_{j\neq k} \frac{e^2}{|\mathrm{r_j} - \mathrm{r_k}|} \tag{2.49}$$

Although the electronic structure of any material should be obtained by solv-
ing the Schrodinger equation $\mathcal{H}\Psi = E\Psi$ of N electrons, the calculation is
practically impossible because of too many variables, namely the $3N$ spatial
coordinates of N electrons.

Density functional theory is another approach to solve many-body prob-
lems, based on the two Hohenberg-Kohn (HK) theorems [80]. The first theorem
states that the ground state properties of a many-electron system is uniquely
determined by an electron density $\rho(\boldsymbol{r})$ which only depends on 3 spatial coor-
dinates. The second theorem proves that the total energy functional $E_{\mathrm{g}}[\rho'(\boldsymbol{r})]$
becomes minimum when $\rho'(\boldsymbol{r})$ is the correct electron density $\rho_{\mathrm{g}}(\boldsymbol{r})$. That is,

$$E_{\mathrm{g}}[\rho_{\mathrm{g}}(\boldsymbol{r})] < E_{\mathrm{g}}[\rho'(\boldsymbol{r})]. \tag{2.50}$$

Therefore, by finding the electron density that minimize the total energy of
a system, one can obtain the ground-state properties. This approach is much

more convenient than to exactly solve the N-electron Schrodinger equations.

The energy functional can be expressed using the kinetic energy $T[\rho]$, the interaction with the external potential v_{ext}, and the electron-electron repulsion V_{ee}, as follows.

$$E[\rho] = T[\rho] + \int \rho(\boldsymbol{r}) v_{\text{ext}} \mathrm{d}\boldsymbol{r} + V_{ee}[\rho]. \tag{2.51}$$

In Kohn-Sham theory [81], it is assumed that the ground-state electron density can be obtained as the ground state density of a fictitious system without electron-electron interactions. Here, N orbitals $\{\varphi_i(\boldsymbol{r})\}$ are introduced, which are the solutions of non-interacting Schrodinger equations with fictitious potential V_{eff},

$$(-\nabla^2 + V_{\text{eff}})\varphi_i = \epsilon_i \varphi_i. \tag{2.52}$$

These orbitals give the electron density as

$$\rho(\boldsymbol{r}) = \sum_i^N |\varphi_i(\boldsymbol{r})|^2. \tag{2.53}$$

Here, the kinetic energy $T[\rho]$ and the electron-electron interaction V_{ee} are approximated as

$$T_s[\rho] = -\sum_i^N \langle \varphi_i | \nabla^2 | \varphi_i \rangle, \ V_{\text{H}}[\rho] = \frac{1}{2} \iint \frac{\rho(\boldsymbol{r})\rho(\boldsymbol{r}')}{|r - r'|} \mathrm{d}\boldsymbol{r}\mathrm{d}\boldsymbol{r}', \tag{2.54}$$

where T_S is non-interacting kinetic energy and V_H the classical Coulomb interaction called Hartree term. The energy functional can be rewritten as

$$E[\rho] = T_s[\rho] + \int \rho(\boldsymbol{r}) v_{\text{ext}} \mathrm{d}\boldsymbol{r} + V_H[\rho] + E_{\text{xc}}[\rho], \tag{2.55}$$

$$E_{\text{xc}}[\rho] = (T[\rho] - T_s[\rho]) + (V_{ee}[\rho] - V_{\text{H}}[\rho]). \tag{2.56}$$

Here, E_{xc} is called "exchange-correlation functional", the form of which is unknown. By using the variational method to find the minimum of the energy functional, one obtains

$$V_{\text{eff}}(\boldsymbol{r}) = V_{\text{ext}}(\boldsymbol{r}) + \frac{1}{2} \int \frac{\rho(\boldsymbol{r}')}{|r - r'|} \mathrm{d}\boldsymbol{r}' + V_{\text{xc}}, \ V_{\text{xc}} = \frac{\delta E_{\text{xc}}}{\delta \rho}. \tag{2.57}$$

Thus, eq. 2.52 becomes

$$[-\nabla^2 + V_{\text{ext}}(\boldsymbol{r}) + \frac{1}{2} \int \frac{\rho(\boldsymbol{r}')}{|r - r'|} \mathrm{d}\boldsymbol{r}' + V_{\text{xc}}]\varphi_i(\boldsymbol{r}) = \epsilon_i \varphi_i(\boldsymbol{r}), \tag{2.58}$$

which is called Kohn-Sham (KS) equation.

Because the form of E_{xc} is unknown, one need to make some approximations to solve the KS equations. For example, local density approximation (LDA) [81] and generalized gradient approximation (GGA) [82] have been widely used, by which the ground state properties have been successfully calculated. Once the form of E_{xc} is determined, the KS equations can be solved in a self-consistent way. First, by using some trial electron density, V_{eff} is calculated. Second, by solving KS equations, $\{\varphi_i\}$ are obtained. Third, the electron density is calculated from φ using eq. 2.53, which will be used for the trial electron density for the next iteration. This cycle is repeated until the electron density or the total energy of the system converges.

2.4.1 WIEN2k package

WIEN2k is a commercial DFT calculation software originally developed by P. Blaha and K. Schwarz [83]. It utilizes the full-potential (linearized) augmented plane-wave plus local orbitals basis set to solve the KS equations, which is one of the most accurate methods for electronic structure calculations.

2.5 Experimental Setup

2.5.1 SPring-8 BL23SU

All the XMCD and photoemission experiments in this thesis were performed at the beam line BL23SU of SPring-8, the world's largest third-generation synchrotron radiation facility, located at Sayo-cho, Hyogo, Japan. BL23SU is a soft x-ray beam line developed and maintained by Japan Atomic Energy Agency (JAEA) for the study of solid state physics as well as surface chemistry and biophysics. The main targets for solid state physics are superconductivity and magnetism of strongly correlated electron system such as actinide compounds and transition-metal compounds. The beam line is equipped with the twin-helical undulator (THU) that can produce left- and right-circularly polarized (LCP and RCP) light of 300 - 1500 eV [84]. The performance of the beam line is briefly summarized in Table 2.3.

The layout of the beam-line optics is shown in Fig. 2.6. The light from the undulator goes through prefocusing mirrors M_v and M_h and becomes monochromatized by a monochromator consisting of entrance and exit slits (S_1 and S_2), vertical focusing mirror M_1 or M_2, and a varied-line-spacing plane grating (VLSPG). After being monochromatized, the beam is refocused by
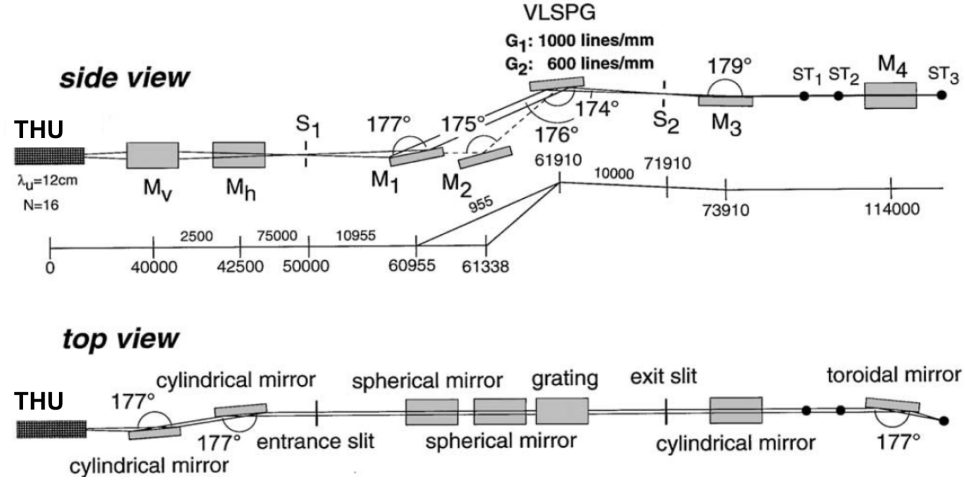
Figure 2.6: Schematic layout of the beam line BL23SU optics [84, 85]. The scale represents the distance from the center of the undulator in units of mm. M_v is a vertical condensing mirror; M_h, a horizontal collimating mirror; $M_{1,2}$, a vertical focusing mirror; M_3, a vertical collimating mirror; M_4, a refocusing toroidal mirror. XMCD and photoemission apparatuses are located at the end station ST_3.

post-focusing mirrors M_3 and M_4. XMCD apparatus is installed at the very end of the beam line (ST_3), and the photoemission apparatus is located between the XMCD apparatus and the M_4 mirror.

For XMCD measurements, RCP and LCP are switched at 1 Hz frequency so that one can obtain dichroic signals without time-dependent backgrounds. This is made possible by having two sets of helical undulators emitting RCP and LCP light as shown in Fig. 2.7. RCP or LCP can be selectively chosen by deforming the electron path using five kicker magnets [86]. When the orbit bump A (B) is generated by activating the kicker magnets 1-3 (3-5), LCP (RCP) light goes through a slit and is guided to the beam line. The helicity

Table 2.3: Performance of the beam line BL23SU of SPring-8 [84].

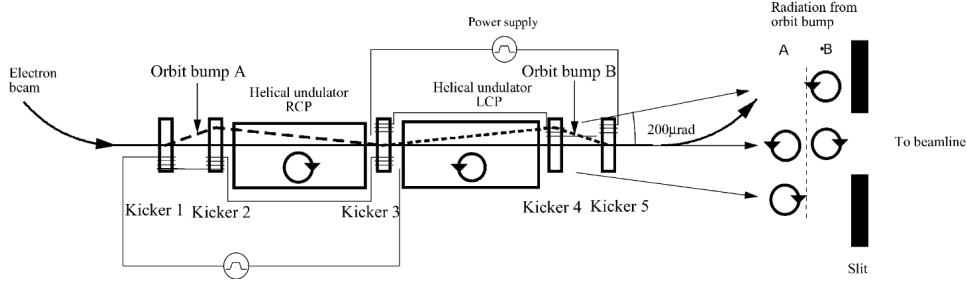| Polarization	Circular
Photon energy	350 - 1500 eV
Beam spot size	< 0.2 mm in diameter
Photon flux	1×10^{12} photons/s/0.01%b.w.
Energy resolution	$E/\Delta E > 10000$

Figure 2.7: Schematic illustration of helicity switching mode of BL23SU [84,86]. The orbit of electron beam is deformed by five kicker magnets. When the orbit bump A (B) is generated, only LCP (RCP) light goes through a slit and reach the end station.

switching at 1 Hz frequency is thus realized by the alternate generation of orbit bumps A and B.

Photoemission spectroscopy station

The photoemission spectroscopy station at BL23SU of SPring-8 is designed for the study of electronic structure of strongly-correlated electron systems. A high-energy-resolution electron energy analyzer SES-2002 is equipped. Since the soft x ray of 350-1500 eV is available, one can perform resonance photoemission experiments at the $L_{2,3}$ absorption edges of $3d$ transition-metal compounds. In addition, one can measure x-ray absorption spectra using TEY method. The measurement temperature can be varied from 10 K to room temperature.

XMCD endstation

The XMCD station at BL23SU of SPring-8 focuses on the study of the magnetism of strongly-correlated electron systems. The apparatus is equipped with a superconducting magnet, which can produce magnetic fields up to 10 T. Absorption signals are collected by TEY mode, and dichroic signals are measured by switching photon helicity as described above. XMCD spectra can be obtained by sweeping the photon energy under a fixed magnetic field. One can also measure element-specific magnetization curves by sweeping the magnetic field under the certain photon energy. The measurement temperature can be varied from 5 K to room temperature.

Chapter 3

XMCD Study of (Al,Fe)Sb

3.1 Introduction

In the insulating FMS (Al,Fe)Sb, ferromagnetism of $T_C = 40$ K emerges with 10% of Fe doping, and the hole concentration is about 10^{17} cm^{-3} [46]. Unlike the other FMSs, further Fe doping up to 14% leads to the decrease in T_C down to 10 K and the two orders of magnitudes increase in the hole concentration up to 10^{19} cm^{-3}. This is probably because the crystal quality is degraded through the creation of many defects, and there is no clear signature of phase separation from reflection high energy electron diffraction (RHEED) patterns and x-ray diffraction (XRD) profiles.

Since (Al,Fe)Sb is insulating, the ferromagnetism is most likely not carrier-induced being different from the other typical FMSs [14]. In the present study, for the purpose of revealing the mechanism of how ferromagnetism appears in (Al,Fe)Sb, we have conducted x-ray absorption spectroscopy (XAS) and x-ray magnetic circular dichroism (XMCD) measurements at the Fe $L_{2,3}$ absorption edge.

In the previous XMCD study on (In,Fe)As:Be [52] and Ge:Fe [55], it was found that nano-scale ferromagnetic domains exist far above the Curie temperature. On lowering the temperature, those domains seemed to coalesce, resulting in global ferromagnetism at the Curie temperature. In the present study, we have found the same behavior for (Al,Fe)Sb and concluded that the nanoscale ferromagnetic domains of several hundreds μ_B are formed in Fe-rich regions, which is likely the universal feature of Fe-doped magnetic semiconductors.

3.2   Experiment

Two samples $Al_{0.9}Fe_{0.1}Sb$ and $Al_{0.86}Fe_{0.14}Sb$ were synthesized using the low-temperature molecular beam epitaxy (LT-MBE) methods by Dr. Le Duc Anh from Prof. Masaaki Tanaka's group at the department of electrical engineering, the University of Tokyo. The structure of the samples was, from the top top surface to the bottom, InAs cap (5nm)/(Al,Fe)Sb (100 nm)/AlSb (100 nm)/GaAs (100 nm)/p-GaAs(001) substrate. The detail of the sample growth is described in Ref. [46].

The XMCD experiment was conducted at beam line BL23SU of SPring-8. Measurement temperature T was varied from 4.5 K to 300 K, and magnetic field $\mu_0 H$ from -7 T to 7 T. The samples were placed in the measurement chamber so that the sample surface was perpendicular to the x-ray incident direction and hence the magnetic field. Absorption signals were collected in the total electron yield (TEY) mode, and dichroic signals were measured by reversing the helicity of x rays with 1 Hz frequency at each photon energy. The spectra were obtained by sweeping the photon energy under a fixed magnetic field, and the scans were repeated with opposite magnetic field direction to minimize experimental artifacts. That is, each XMCD spectrum was obtained as $(\sigma_{+,h} - \sigma_{-,h}) + (\sigma_{-,-h} - \sigma_{+,-h})$, and each XAS spectrum as the summation of all the four terms, where σ denotes the absorption cross-sections, the first subscript the helicity of x rays, and the second subscript the direction of magnetic field. We also measured magnetization curves by recording XMCD signals at the photon energies of the $L_{2,3}$ edge with sweeping the magnetic field. The data have been normalized to the total magnetic moment at $\mu_0 H = 7$ T deduced by applying the XMCD sum rules to the spectra [64, 65, 67].

3.3   Results and Discussion

Figure 3.1 shows raw absorption spectra taken with x rays of positive and negative helicities under $\mu_0 H = 7$ T and $T = 4.5$ K. As can be seen from the figure, there is a large difference between the two helicities, indicating that the magnetism indeed arises from the Fe atoms. Because there was a 5 nm thick InAs capping layer to prevent oxidation, a relatively strong In M_2 peak overlapped the Fe L_3 peak. In order to remove the In contribution, we assumed a Lorentzian function and subtracted it from the spectra together with a linear background and a double step functions representing the Fe $L_{2,3}$-edge jumps. The summation and the difference spectra after the background subtraction are also shown at the bottom of Fig. 3.1. Note that we have processed all the
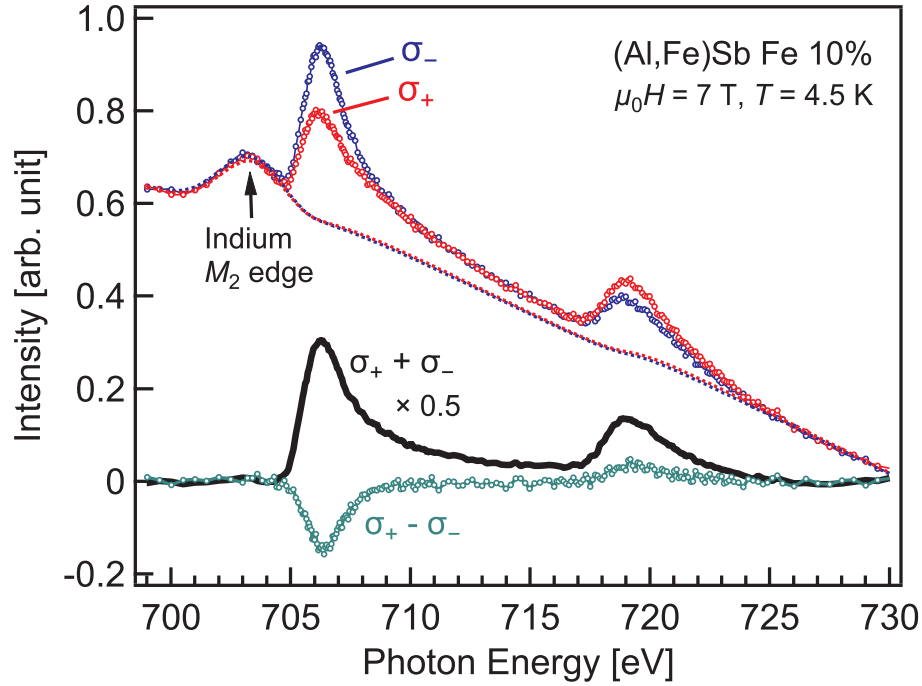
Figure 3.1: Absorption spectra taken with x rays of positive and negative helicity. Dashed curves represent the backgrounds, which consist of a Lorentzian function representing the Indium M_2 peak, a double-step function for edge jumps, and a linear function. At the bottom, XAS and XMCD spectra after the background subtraction are also shown.

data in the same manner.

Figure 3.2 shows the averaged XAS and XMCD spectra of (Al,Fe)Sb taken under two opposite magnetic-field directions as described above. Here, the spectra of other Fe-doped FMSs, namely, (Ga,Fe)Sb and (In,Fe)As:Be, as well as those of Fe metal, $FeCr_2S_4$ (Fe^{2+}), and Fe_2O_3 (Fe^{3+}) are also shown for comparison. The XAS and XMCD spectra of (Al,Fe)Sb is broad and asymmetric having a tail on the high-energy side, being similar to the case of Fe metal. In addition, fine structures due to multiplet splitting are hardly seen, which would be present if $3d$ electrons are localized as in Fe_2O_3 and $FeCr_2S_4$. These indicate the significant delocalization of the Fe $3d$ electrons and would challenge the assumption that Fe takes the valence of 3+ with localized five $3d$ electrons. The same is also true for the other Fe-doped FMSs [52, 55], and it seems that the itinerancy of Fe $3d$ electrons are the key for the ferromagnetism of the Fe-doped systems. Note that although there are small differences in XAS spectra of (Al,Fe)Sb, (Ga,Fe)Sb and (In,Fe)As:Be, which most likely
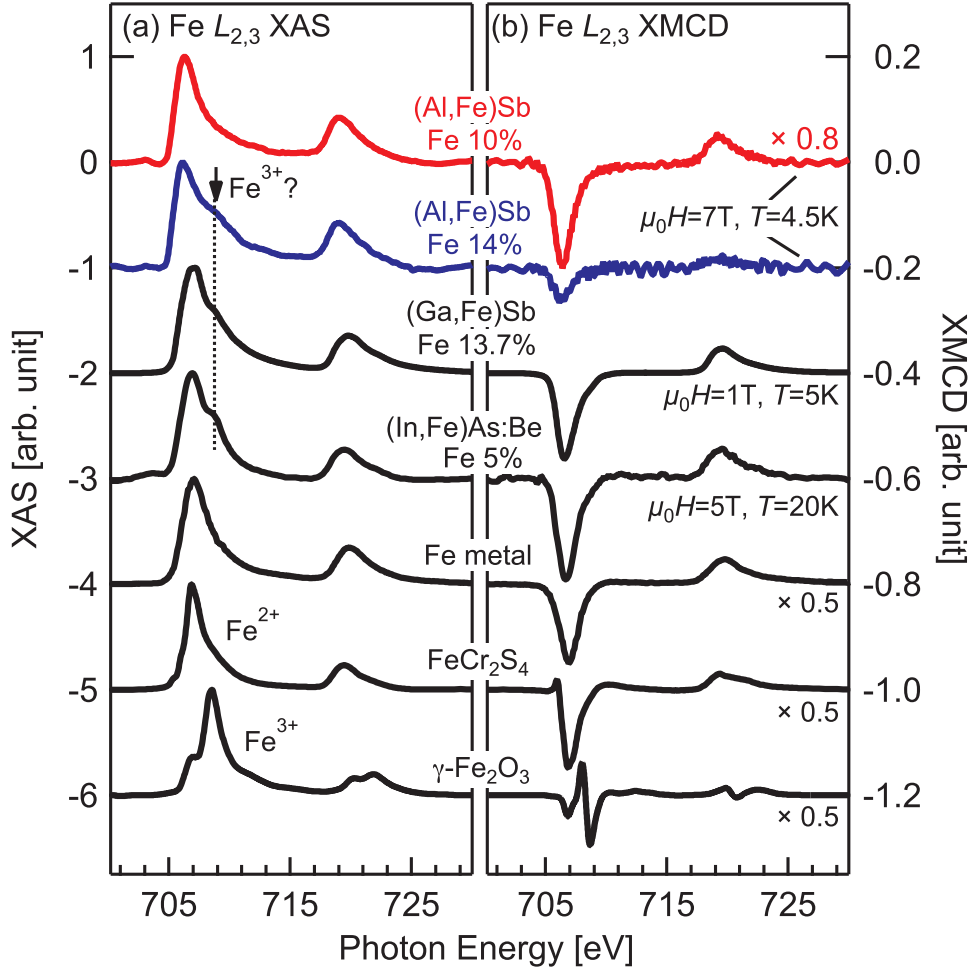
Figure 3.2: XAS and XMCD spectra of (Al,Fe)Sb in comparison with those of (Ga,Fe)Sb [87], (In,Fe)As:Be [52], Fe metal [67], FeCr$_2$S$_4$, and γ-Fe$_2$O$_3$ [88].

stem from extrinsic components such as surface oxides, the XMCD spectra have almost identical lineshapes. This indicates that the local electronic structure of the Fe atoms that contribute to the ferromagnetism is very similar among the Fe-doped FMSs.

Regarding the Fe concentration dependence, only the XAS spectrum of the sample with Fe 14% has a shoulder around 709 eV. Because a corresponding structure does not exist in the XMCD spectrum, it would be attributed to extrinsic nonmagnetic Fe^{3+} signals originating from Fe oxides formed near the surface or some defect states taking into account the crystal quality lower than that of the Fe 10% sample.

The XMCD intensity is considerably weaker for the 14% Fe-doped than for

the 10% Fe-doped sample, which is consistent with the observation that the Curie temperature decreases with increasing Fe concentration from 10% to 14%. This also suggests that the ferromagnetism of (Al,Fe)Sb is not due to Fe-metal precipitates because if the magnetism originated from Fe-metal precipitates, higher Fe doping level would result in enhanced ferromagnetism. Taking into account that the spectral line shapes of XAS and XMCD are similar between the two samples except for the small shoulder in the XAS spectrum of 14% Fe-doped sample, the disappearance or the weakening of the ferromagnetism with increasing Fe concentration seems also intrinsic.

The spin and orbital magnetic moments at $\mu_0 H = 7$ T and $T = 4.5$ K estimated from the XMCD sum rules were $(m_{\mathrm{spin}}, m_{\mathrm{orb}}) = (1.63, 0.423)$ for Fe 10% and $(0.38, 0.08)$ for Fe 14%. Here, we assumed the number of $3d$ electrons to be 6, which was deduced from first-principles supercell calculations, and the correction factor to be 0.875 for Fe^{2+} state [68, 69]. The unquenched orbital magnetic moments seem to support the $3d^6\underline{L}$ configuration of the Fe atom, where $\underline{L}$ denotes a ligand hole. Note that the uncertainty in $m_{\mathrm{orb}}/m_{\mathrm{spin}}$ and $m_{\mathrm{orb}} + m_{\mathrm{spin}}$ can be as large as $\sim 20\%$ and $\sim 10\%$, respectively, because the thick InAs capping layer made signals very weak.

Figures 3.3(a) and 3.3(b) show the magnetization curves measured at various temperatures by XMCD. Here, hysteresis could not be detected because it was too small. Despite the fact that the T_{C}, below which hysteresis appears, is as low as 40 K for the sample with 10% Fe, the magnetization M still strongly depends on the magnetic field at 300 K in contrast to typical ferromagnets, where magnetization disappears rather quickly above T_C. We attribute this behavior to the superparamagnetism of nanoscale ferromagnetic domains (FM/SPM domains), as has been also found in other Fe-doped FMSs [52, 55]. At the low temperature of 4.5 K, the magnetization shows a gradual linear increase after the steep increase at low magnetic fields. This indicates the existence of paramagnetic Fe atoms even below T_{C}. To be quantitative, the magnetic susceptibility or the slope of the magnetization versus magnetic field curve at low and high magnetic fields are plotted in Figs. 3.3(c) and 3.3(d), respectively, where

$$\chi_{\mathrm{low}} = \left.\frac{\Delta M}{\Delta(\mu_0 H)}\right|_{\mu_0 H = 0\mathrm{T}}, \chi_{\mathrm{high}} = \left.\frac{\Delta M}{\Delta(\mu_0 H)}\right|_{\mu_0 H = 7\mathrm{T}}. \tag{3.1}$$

Note that, in Fig. 3.3(c), χ_{low} is multiplied by the temperature to see whether χ_{low} is inversely proportional to temperature as in ideal superparamagnetism. Although the $\chi_{\mathrm{low}}T$ of the sample with 10% Fe shows some temperature depen-

dence, it remains large even at 300 K, suggesting the existence of superparamagnetism. On lowering the temperature, $\chi_{\text{low}}T$ gradually increases, which may indicate that the number of Fe atoms participating in superparamagnetism increases. Further lowering the temperature down to below $T_C = 40$ K leads to a drop of $\chi_{\text{low}}T$, which implies the system turns into global ferromagnetism which cannot be explained by superparamagnetism.

As for the high magnetic field susceptibility χ_{high}, the values remain finite even at the low temperature of 4.5 K, indicating the coexistence of ferromagnetism and paramagnetism, and they are comparable between the two samples. Considering that there are much more paramagnetic Fe atoms in the sample with 14% Fe, χ_{high} should be much larger. This may be due to the antiferromagnetic correlation between Fe atoms in the case of 14% Fe doping.

In order to understand the behavior of χ_{low} and χ_{high} or how the paramagnetic and superparamagnetic/ferromagnetic phase coexist more in detail, we fitted the data to the linear combination of the Langevin function $L(\xi)$ representing superparamagnetism and a linear function representing paramagnetism:

$$M = x m_{\text{sat}} \mu_B L\left(\frac{\mu \mu_0 H}{k_B T}\right) + (1 - x)\frac{C \mu_0 H}{T + T_A}, \tag{3.2}$$

$$C = \frac{m_{\text{sat}}(m_{\text{sat}} + 2)\mu_B^2}{3 k_B}, \tag{3.3}$$

$$L(\xi) = \coth(\xi) - \frac{1}{\xi}, \tag{3.4}$$

where M is the magnetization per Fe atom, $m_{\text{sat}}\mu_B$ the total magnetic moment of Fe atom, μ_B the Bohr magneton, k_B the Boltzmann constant, and C the Curie constant. We have assumed that $m_{\text{sat}} = 3.4$, which was obtained by first-principles supercell calculation, and that the g factor is 2 for simplicity. Fitting parameters in the present model are the following: μ, the total magnetic moment of a superparamagnetic (SPM) cluster; x, the fraction of Fe atoms participating in ferromagnetism or superparamagnetism; T_A, the antiferromagnetic Weiss temperature. Note that μ and x were allowed to vary with temperature, while T_A was kept constant.

The fitted curves are shown by solid curves and the paramagnetic linear components are also separately shown by dashed lines in Figs. 3.3(a) and 3.3(b). As can be seen, the data were fitted well by the equation. The fitting yielded the antiferromagnetic Weiss temperature of 28 K for the sample with 10% Fe and 98 K for the sample with 14% Fe, again indicating that antiferromagnetic correlations are stronger for the sample with 14% Fe. This may
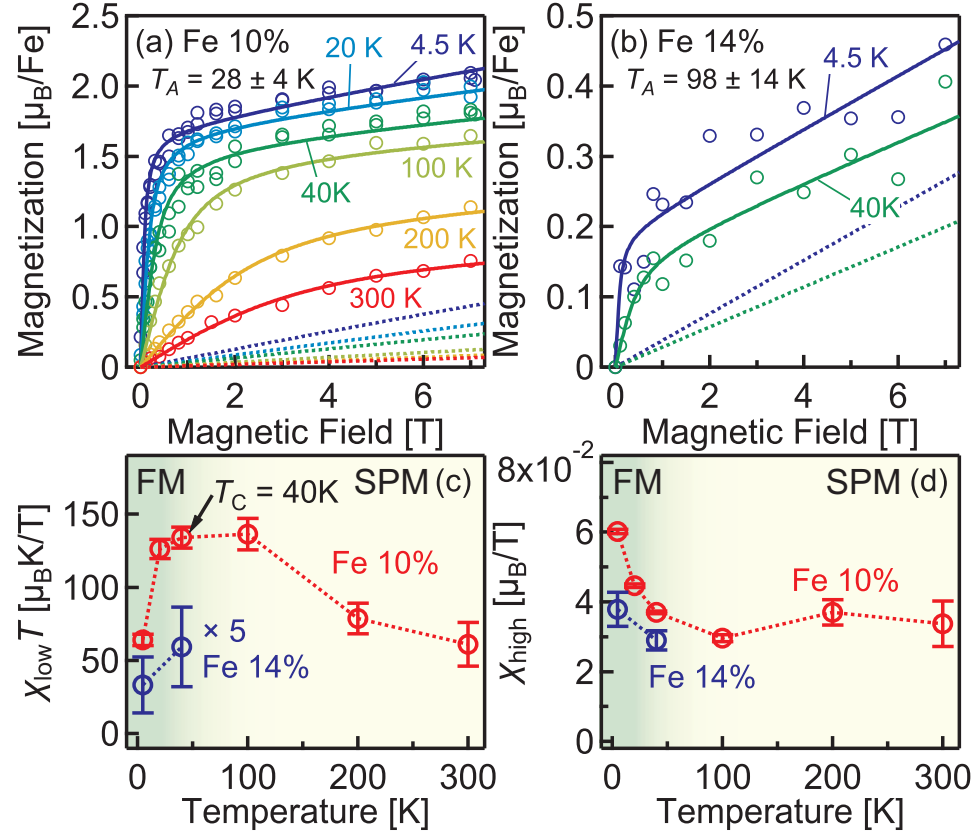
Figure 3.3: (a) Magnetization curves of the sample with 10% Fe and (b) the sample with 14% Fe deduced from XMCD. The fitting results are shown by solid curves, and the paramagnetic linear components are also separately shown by dashed lines. (c) Magnetic susceptibility at low magnetic fields near 0 T and (d) that at high magnetic fields around 7 T, which are deduced from the fitting results. Here, the low magnetic field susceptibility is multiplied by temperature.

be because antiferromagnetic superexchange interactions between adjacent Fe atoms become dominant when the concentration of doped Fe atoms increases. Note that using the Brillouin function instead of a linear function does not change the line shape of the fitting curves as well as the fitting parameters, because relatively large Weiss temperatures make the Brillouin function linear within the range of 0 T to 7 T even at the low temperature of 4.5 K.

Figures 3.4(a) and 3.4(b) show the temperature dependences of the obtained fitting parameters x, the fraction of Fe atoms participating in ferromagnetism or superparamagnetism, and μ, the total magnetic moment of each FM/SPM domain, respectively. x for the sample with 14% Fe was about only 5%, which
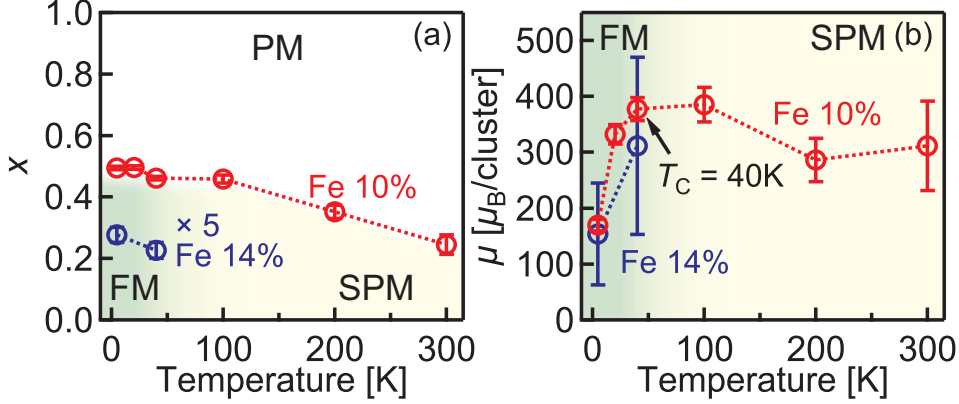
Figure 3.4: Fitting parameters. (a) Fraction of Fe atoms contributing to ferro-magnetism or superparamagnetism, denoted by x. (b) Total magnetic moment μ per one FM/SPM domains

confirms the near absence of ferromagnetism in the sample with 14% Fe.

In the case of 10% Fe doping, x gradually increases with decreasing temper-ature, and 25% of Fe atoms still contribute to the FM/SPM at 300 K, while 50% Fe remain paramagnetic even at 4.5 K. This highlights the inhomogeneous na-ture of magnetism in (Al,Fe)Sb. The magnetic moment per FM/SPM domain was found to be 300-400μ_B, and it also increased from $\sim 300\mu_B$ to $\sim 400\mu_B$ with decreasing temperature from 300 K to 40 K. Note that μ dropped suddenly be-low 40 K, as $\chi_{low}T$ dropped, reflecting the gradual appearance of macroscopic ferromagnetism, in which the system deviates from the Langevin behavior. Here, μ of 300μ_B-400μ_B corresponds to $\mu/m_{Fe}\mu_B \sim 100$ Fe atoms. The density of FM/SPM domains could be deduced from μ and x as 7×10^{18} cm^{-3} for the sample with 10% Fe and 1×10^{18} cm^{-3} for the sample with 14% Fe. Assuming that the Fe atoms are distributed randomly and the domains have spherical shape, the radius of the domain can be calculated to be 2.5 nm for Fe 10% doping.

The origin of the nanoscale FM/SPM domains may be attributed to the nanoscale fluctuation in Fe distribution as discussed for the other Fe-doped semiconductors (In,Fe)As:Be [52, 89] and Ge:Fe [55, 90, 91]. In addition, the previous theoretical studies, where chemical pair interactions were calculated, suggested that Fe atoms tend to segregate and form Fe-rich regions with keep-ing the lattice structure in the InAs [89] and Ge [90] matrix, while maintain-ing the zinc blende and diamond lattice structure. Note that in the case of (In,Fe)As:Be, the formation of first nearest-neighbor Fe-Fe pairs is not favor-

able energetically [89]. The same kind of scenario may also be applied to (Al,Fe)Sb and possibly to the other Fe-doped FMSs. If so, short-range ferromagnetic interaction, probably double exchange interaction, between Fe $3d$ orbitals can stabilize the ferromagnetism in nanoscale Fe-rich FM/SPM domains at rather high temperatures around 300 K. This may be consistent with the present XAS and XMCD spectra, where rather close Fe-Fe distance bestows the itinerancy of the $3d$ electrons. On lowering the temperature, those domains would start to overlap or interact with each other, resulting in the macroscopic ferromagnetism.

3.4   Summary

We have performed x-ray absorption spectroscopy (XAS) and x-ray magnetic circular dichroism (XMCD) on the new ferromagnetic semiconductor (Al,Fe)Sb to study its electronic structure and magnetization process. The spectral line shapes were broad and asymmetric having a tail on the high-energy side, indicating the itinerant nature of Fe $3d$ electrons. The XMCD sum rules yielded an unquenched orbital magnetic moment, which suggests that Fe takes the $3d^6$ configuration with a ligand hole. From the magnetization curves measured by XMCD, in the case of optimally doped sample with 10% Fe, it was found that nanoscale ferromagnetic domains of 300-400 μ_B exist even at room temperature, much above the Curie temperature, and the system behaves as a superparamagnet. The formation of such domains was ascribed to the non-uniform distribution of Fe atoms on the nanoscale. For the sample with 14% Fe, the weakening of the ferromagnetism and the strengthening of the antiferromagnetic correlations were observed compared to the 10% doping case. This may be because antiferromagnetic superexchange interaction between adjacent Fe atoms becomes dominant when the system is doped with a large concentration of Fe atoms.

Chapter 4

ARPES and First-Principles Calculation Studies of Ge:Fe

Part of this chapter has been published in " Origin of robust nanoscale ferromagnetism in Fe-doped Ge revealed by angle-resolved photoemission spectroscopy ", S. Sakamoto, Y. K. Wakabayashi, Y. Takeda, S.-i. Fujimori, H. Suzuki, Y. Ban, H. Yamagami, M. Tanaka, S. Ohya, and A. Fujimori, Physical Review B **95**, 075203 (2017).

4.1 Introduction

Ferromagnetic semiconductors (FMSs) such as (Ga,Mn)As [7, 12] have been studied extensively driven by scientific and technological interest [1, 14, 15, 39, 92, 93] as mentioned in Chapter 1. Among them, Group-IV FMSs are especially important since they are compatible with mature Si-based electronics. In fact, $Ge_{1-x}Fe_x$ (Ge:Fe) [44, 45, 54, 94] can be epitaxially grown on Ge and Si substrates by the low-temperature molecular beam epitaxy (LT-MBE) method without the formation of any second phases [95]. The Curie temperature (T_C) increases as the Fe content increases and also as the Fe atom distribution becomes inhomogeneous [45, 54]. The highest T_C of ~210 K is reached by post-growth annealing [54], which is higher than the T_C of (Ga,Mn)As of ~200 K [16]. Unlike (Ga,Mn)As, where the T_C is dependent significantly on the carrier concentration or the hole conductivity, the T_C of Ge:Fe is not, and the conductivity remains low upon Fe doping [95]. Recent x-ray magnetic circular dichroism (XMCD) study [55] has shown that the ferromagnetism evolves from nanoscale ferromagnetic domains formed in Fe-rich regions, which persists even at room temperature.

When an Fe atom substitutes for a Ge atom, the neutral Ge atom with the $3d^{10}(4sp)^4$ configuration is replaced by the neutral Fe atom with the $3d^6(4sp)^2$, $3d^5(4sp)^3$, or $3d^4(4sp)^4$ configuration. If the Fe atom takes the $3d^6(4sp)^2$ configuration (Fe^{2+}), two holes are provided to the Ge host since two $4sp$ electrons are missing in the $3d^6(4sp)^2$ configuration compared to $3d^{10}(4sp)^4$. An interstitial Fe^{2+} atom acts as a double-donor, which donate the $(4sp)^2$ electrons to the Ge host. Taking $\sim$15% of interstitial Fe atoms [45] into account, the number of holes brought by one Fe atom can be estimated as $2 \times 0.85 - 2 \times 0.15 = 1.4$.

In order to explain the origin of the ferromagnetism in (Ga,Mn)As and related FMSs, two models have been proposed so far [31, 93, 96], namely, the valence-band model [20, 35] and the impurity-band model [97–100] as introduced in Chapter 1. In the valence-band model, acceptor levels derived from the magnetic impurities are merged into the valence band and itinerant holes occupying states around the valence-band maximum (VBM) mediate ferromagnetism through Zener's p-d exchange mechanism. In the case of the impurity-band model, on the other hand, impurity levels are detached from the VBM and lies within the band gap of the host semiconductor and hence ferromagnetism is stabilized through a double-exchange-like mechanism within the impurity band.

In this chapter, we elucidate the origin of the ferromagnetism of Ge:Fe distinct from that of (Ga,Mn)As by examining its electronic structure. Especially, the Fermi level (E_F) position and the modification of the host band structure caused by the Fe 3d electrons were studied using soft x-ray angle-resolved photoemission spectroscopy (SX-ARPES) and first-principles supercell calculations.

4.2   Experiment & Calculation

A Ge$_{0.935}$Fe$_{0.065}$ thin film was synthesized using the LT-MBE method at the substrate temperature of 240 °C by Dr. Yuki Wakabayashi from Prof. Masaaki Tanaka's group at the department of electrical engineering, the University of Tokyo. The structure of the sample was Ge cap ($\sim$ 2 nm)/Ge$_{0.935}$Fe$_{0.065}$ ($\sim$120 nm)/Ge buffer ($\sim$30 nm)/p-Ge (001) substrate from the top surface to the bottom. Note that the growth condition and the sample structure were the same as the previous studies [45, 55], and the sample is expected to have inhomogeneous distribution of Fe atoms while keeping the diamond lattice structure and to show nanoscale ferromagnetic order above the T_C of 100 K [45, 55]. In the Fe-rich regions, the Fe content would be about 10%, while $\sim$4% in the Fe-poor regions [45].

A SX-ARPES experiment was conducted at beam line BL23SU of SPring-8. The sample temperature was kept at 20 K and circularly polarized x rays of 700-950 eV were used. The sample was placed so that the [-110] direction became parallel to the analyzer slit and perpendicular to the beam. Rotating the sample around the [-110] axis and changing the photon energy enabled us to cover the entire Brillouin zone. The overall energy resolution of the photoemission experiment was about 170 meV. X-ray absorption spectra were also taken in the total electron yield mode. In order to remove the oxidized layer at the surface, we etched the sample in a hydrofluoric acid (HF) solution (3 mol/L) for 5 seconds and subsequently rinsed it in water just before loading the sample into the vacuum chamber of the spectrometer. This method is known to be efficient for cleaning the surfaces of Ge [101] as well as those of Ge:Fe [55].

First-principles calculations based on the density functional theory (DFT) were done utilizing the full-potential augmented-plane-wave plus local orbital method as implemented in the WIEN2k code [83]. For the calculation of the host Ge band structure, modified Becke-Johnson (mBJ) exchange potential with the local density approximation (LDA) for correlation potential [102] was employed. For the calculation of the partial density of states (PDOS) of Ge:Fe, we constructed the $3\times3\times3$ supercell of $Ge_{53}Fe$ and the cubic unit cell of Ge_7Fe as shown in Figs. 4.4(d) and (e), respectively. Here, the generalized gradient approximation (GGA) of the Perdew-Burke-Ernzerhof type [82] was used for the exchange-correlation energy functional. The experimental lattice constant of $a = 5.648$ Å for $Ge_{0.935}Fe_{0.065}$ [45] was used and spin-orbit interaction was included for all the calculations.

4.3   Results & Discussion

4.3.1   Resonance Photoemission

Figure 4.1(a) shows resonance photoemission (RPES) spectra taken in the angle-integrated mode with changing the photon energy from 704 eV to 714 eV by 0.5 eV across the Fe L_3 absorption edge. Here, the off-resonance spectrum taken at a lower photon energy of 704 eV shown in Fig. 4.1(b) was subtracted from all the spectra. Used photon energies are also indicated by open circles on the XAS spectra in Fig. 4.1(c), whose color correspond to that of the spectra. Note that the binding energy is defined relative to E_F. Figure 4.1(d) shows the false color plot of the spectra in Fig. 4.1(a) normalized to the area of the energy distribution curve (EDC). There can be seen the strong normal Auger
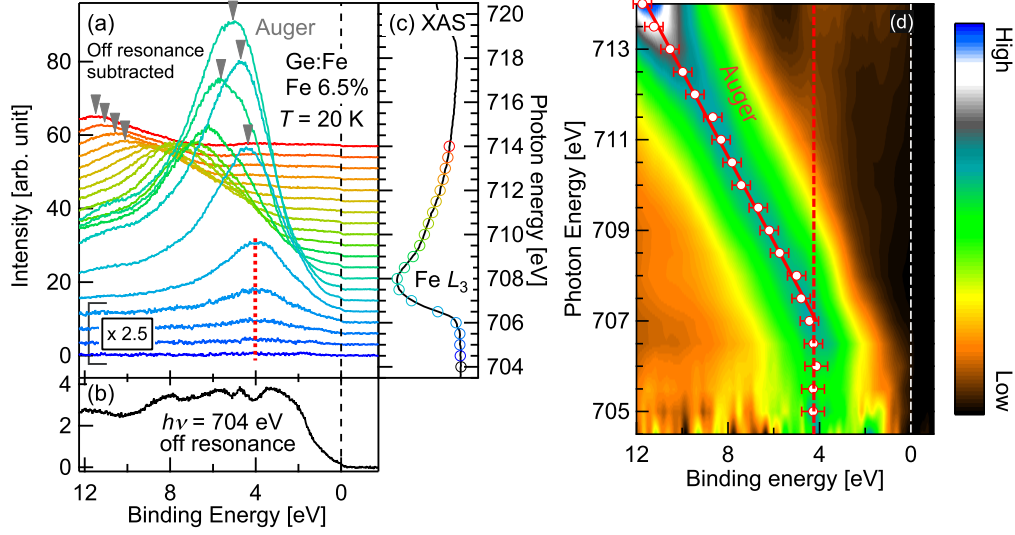
Figure 4.1: Resonance photoemission spectra of $Ge_{0.9335}Fe_{0.065}$. (a) Angle-integrated spectra with changing the photon energy by 0.5 eV across the Fe L_3 absorption edge as depicted by circles on the XAS spectrum in panel (c). The off-resonance spectrum shown in panel (b) has been subtracted from all the spectra in panel (a), where the units of the vertical axes in panels (a) and (b) are the same. The spectra for $h\nu$ = 704.5 - 706 eV have been magnified by a factor of 2.5. (d) False color plot of the spectra in panel (a) normalized to the area of the energy distribution curve (EDC). The red points represent the peak position of each spectrum. The dispersive Auger peak and the non-dispersive resonance feature are indicated by red solid and dashed lines, respectively.

peak dispersing with photon energy as denoted by triangles in Fig. 4.1(a) and a red solid line in Fig. 4.1(d). The existence of Auger peak indicates the itinerant nature of the Fe $3d$ electrons in Ge:Fe, because the normal Auger process occurs when the core-hole potential is screened by conduction electrons faster than core-hole decay. This is further confirmed by the fact that XAS spectra consisted of a broad single peak with asymmetric tail on higher-energy side and did not exhibit multiplet features which should be present when $3d$ electrons are localized [103]. It should be noted that the XAS spectrum did not show Fe^{3+} oxides signals, which guarantees the effectiveness of the HF etching prior to the measurements.

In addition to the normal Auger peak, non-dispersive feature can be seen around the binding energy of 4.2 eV shown by a red dashed line in 4.1(a) and 4.1(d), and exhibited resonance enhancement. Such a non-dispersive resonance feature is either due to direct recombination, where the photoexcited electron
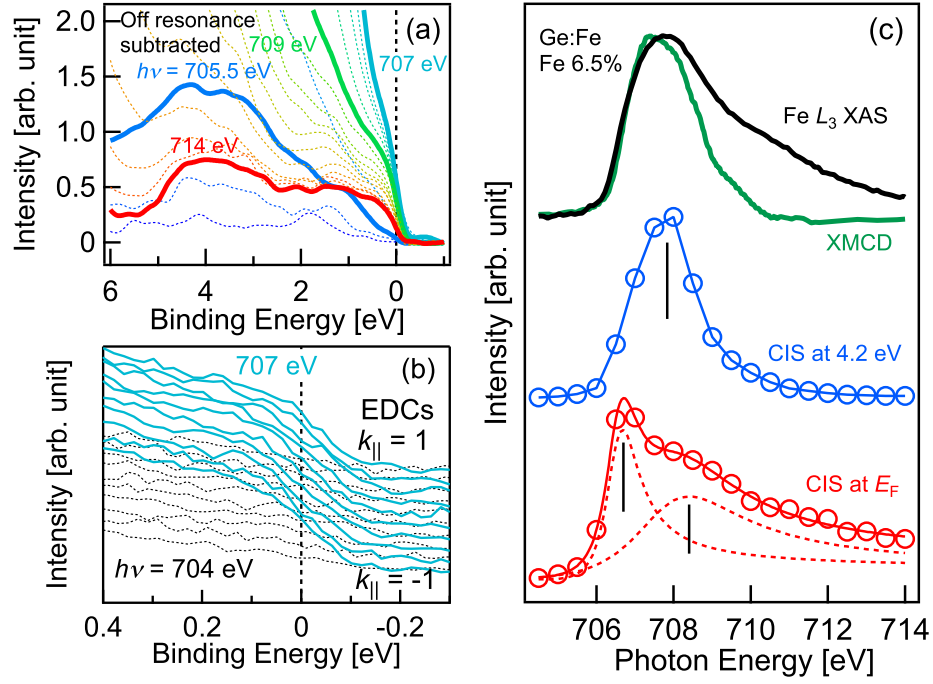
Figure 4.2: (a) Enlarged plot of the spectra in Fig. 4.1(a), where the same color is used. (b) Energy distribution curves (EDCs) taken in the angle-resolved mode along $k_\parallel \parallel$ [-110], where the used photon energies are 704 eV (off resonance) and 707 eV (on resonance). Note that $k_\parallel$ is in units of $2\sqrt{2}\pi/a$. (c) Constant initial state (CIS) spectra around E_F ($E_B = 0.4$ to -0.2 eV) and at 4.2 eV. XAS and XMCD spectra [55] are also shown by black and green solid curves, respectively.

recombines with the core hole, or to a satellite [104], where the photoexcited core electron acts as a spectator to the core-hole recombination process. Note that similar behavior has been also found in various metallic compounds such as Ni [105, 106], Cr, Fe [107], and Fe-based superconductors [75, 108, 109]. The peak position of 4.2 ± 0.2 eV is larger than that of Fe metal (3.2 eV) [107] but is close to that of the Fe-based superconductors $CeFeAsO_{0.89}F_{0.11}$ (4.2 eV) [108] and $BaFe_2As_2$ (3.6eV) [109], which might be relevant to the similar tetrahedral coordination of non-metal atoms to the Fe atoms in the Fe-based superconductors and Ge:Fe.

Figure 4.2(a) shows the smoothed RPES spectra plotted on an expanded scale. Although strong Auger peak made it difficult to extract the PDOS from the spectra taken with $h\nu = 708$ eV at which XAS peaked, we have deduced the Fe 3d PDOS by using a higher energy photons of 714 eV, as

shown by a red curve in Fig. 4.2(a). The PDOS is broad extending from E_{F} to 5 eV below it, out of which the structure around 4.2 eV was attributed to a satellite because it showed strong enhancement at the resonance energy like the satellite in transition metals and transition-metal compounds as mentioned above. Therefore, we conclude that the main part of the Fe $3d$ PDOS is located from E_{F} to $\sim$3 eV. In addition, Fermi edge-like step is present at E_{F}, which indicates that the Fe $3d$ states have a finite contribution to the states at E_{F}, and would be involved in the charge transport of Ge:Fe.

Figure 4.2(b) shows the energy distribution curves (EDCs) taken in the angle-resolved mode along $k_{\parallel} \parallel$ [-110] at the photon energies of 704 eV (off-resonance) and 707 eV (on-resonance). The enhanced Fe $3d$ states at E_{F} were found to exist in a wide region in momentum space without appreciable dispersions. Note that the Fermi edge-like feature at E_{F} is much clearer in Ge:Fe than in (Ga,Mn)As [110, 111], indicating that contributions of $3d$ electrons to states at E_{F} are more pronounced in Ge:Fe than in (Ga,Mn)As.

Figure 4.2(c) shows the intensity of the RPES spectrum around E_{F} (-0.2 to 0.4 eV) as a function of photon energy, namely, constant initial state (CIS) spectrum, where the XAS and XMCD [55] spectra and the CIS spectrum at E_B =4.2 eV are also shown as references. Although the CIS spectrum at E_B =4.2 eV has a similar line shape to the XAS spectrum, the CIS spectrum at E_{F} showed a sharp increase at the threshold well below the peak of the XAS spectrum, followed by a broader peak at a higher photon energy. Here, for clarity, we have fitted the spectrum to the combination of two Fano profiles [77]. The fitting curve is shown by a red solid curve and each Fano profile by a red dashed curve. Since the peak position of the XMCD spectrum is also located at a lower photon energy than that of the XAS spectrum, the Fe $3d$ states at E_F may contribute to the magnetism significantly. The sharp increase may originate from the transitions into the narrow $3d(e)$ band just above E_{F}, while the broader peak from transitions into the empty $3d(t_2)$ level, corresponding to the XAS spectrum, which will be discussed below.

4.3.2   ARPES Spectra

Figure 4.3(a) shows the photon energy dependence of ARPES spectra along $k_{\parallel}$ direction at the binding energy of 4 eV, where photon energy changed from 850 eV to 920 eV to find the Γ point. It was found from the symmetry of the spectra that the ARPES taken with x rays of 875 eV crosses the Γ point. The maximum energy of the valence-band dispersion is plotted against photon energy in Fig. 4.3(b), and indeed reaches its highest, namely, the valence band
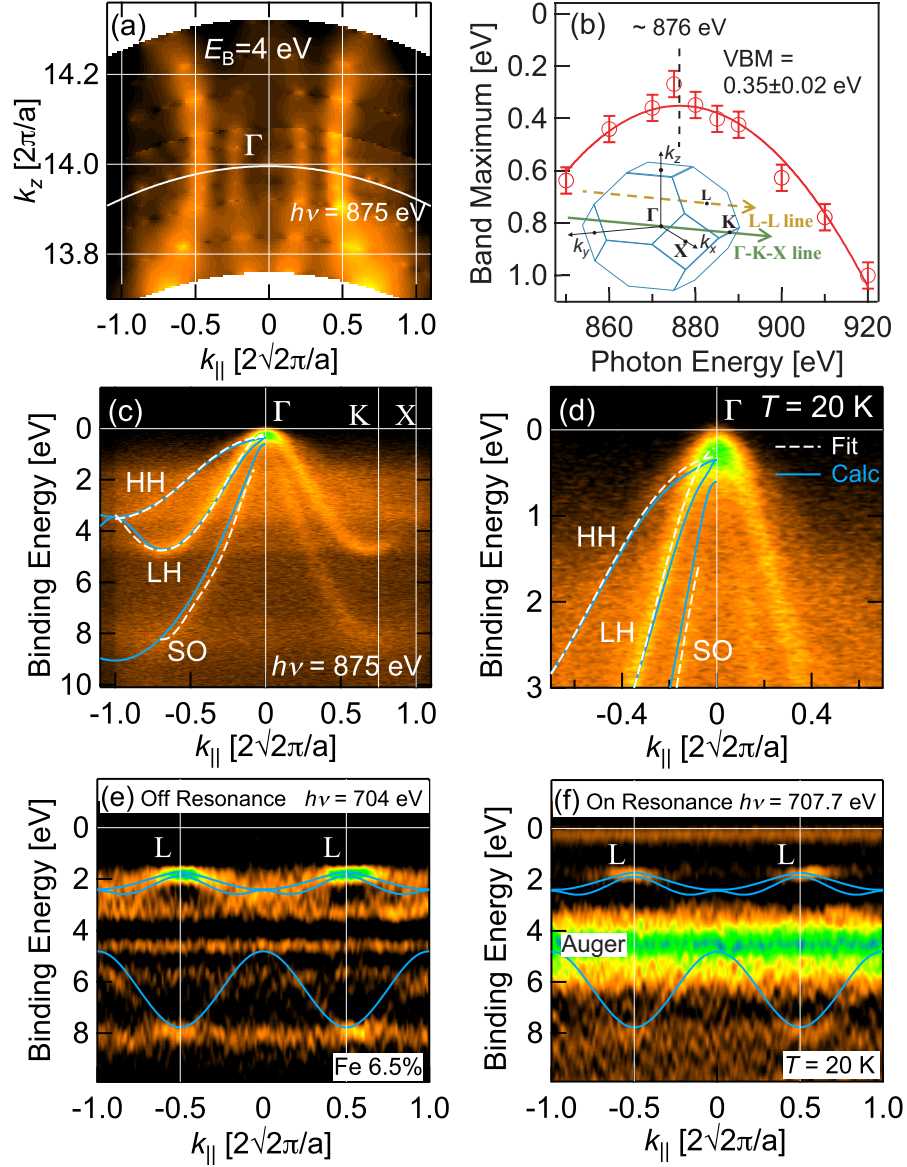
Figure 4.3: ARPES band mapping for $Ge_{0.935}Fe_{0.065}$. (a) $k_{\parallel}$-k_z mapping image at the binding energy of 4 eV. A white curve represents the ARPES cut for the photon energy of 875 eV. (b) Energy position of the band maximum along $k_{\parallel}$ as a function of photon energy. The solid red curve represents a fitted parabolic function. Inset shows the Brillouin zone of the fcc lattice. (c), (d) ARPES spectra along the Γ-K-X line taken with $h\nu = 875$ eV. The peak positions of the second derivatives of the EDCs have been fitted to a Fourier series and are shown by white dashed curves. (e), (f) EDC second derivatives of the ARPES spectra taken at (e) off-resonance ($h\nu = 704$ eV) and (f) on-resonance (707.7 eV). In panels (c)-(f), solid blue curves represent the calculated band dispersions of the host Ge.

maximum (VBM), at ~ 876 eV. The energy of the VBM was also deduced to be 0.35 eV below E_{F}, indicating that the Fermi level of Ge:Fe is located in the middle of the Ge band gap of ~ 0.7 eV. From this photon-energy dependence, the inner potential was estimated to be 11 eV.

Figure 4.3(c) shows ARPES spectra along the Γ-K-X line in the Brillouin zone of the fcc lattice (see the inset of Fig. 4.3(b)) taken with the photon energy of 875 eV. The peak positions of the second derivatives of the EDCs were fitted to a Fourier series up to 5th order and are shown by white dashed curves. Here, heavy-hole (HH), light-hole (LH), and split-off (SO) bands characteristic of Ge were clearly observed, which guarantees the good crystallinity of the Ge:Fe sample as well as the clean surface after the HF etching. It was also found that the ARPES spectra of Ge:Fe agree fairy well with the calculated band dispersions of the Ge host, which are shown by blue solid curves. This indicates that the doped Fe atoms did not affect the electronic structure of the Ge host significantly. Note that the observed band structure most likely reflected contributions from the Fe-poor regions (4%) more than the Fe-rich (10%) regions for the following reasons: the volume of the Fe-poor regions is larger than that of the Fe-rich regions by $\sim 20\%$ in the present 6.5% Fe-doped sample; the band structure of the Fe-rich regions should be perturbed more strongly and become more obscured than that of the Fe-poor regions. Such an insensitivity of the band structure to transition-metal doping was also reported in the previous SX-ARPES [110] and VUV-ARPES [111] studies on (Ga,Mn)As, although whether or not the energy bands shifts with doping remains controversial. Figure 4.3(d) provides a closer look at the ARPES spectra near the Γ point. As mentioned above, the VBM does not touch the Fermi level and is located 0.35 eV below it.

Figures 4.3(e) and 4.3(f) show the EDC second derivative of the ARPES spectra taken at $h\nu = 704$ eV (off-resonance) and 707.7 eV (on-resonance), respectively. The photon energies of 704-707.7 eV nearly correspond to the L-L line in the Brillouin zone if the inner potential of ~ 11 eV is assumed. In the figures, calculated band dispersions of the Ge host are also shown by blue solid curves. Note that the non-dispersive flat features seen in Fig. 4.3(e) is not from Fe atoms, but just from the photoelectrons that lost the momentum information when escaping from the surface because those flat structures were not enhanced on resonance. Apart from the intense Auger peak seen in the on-resonance spectra, the primary difference from the off-resonance spectra is the non-dispersive feature just below E_{F} as already seen in Fig. 4.2. This feature originates from the Fermi edge of the Fe $3d$ states enhanced on resonance and probably reflects the randomness of the Fe distribution.
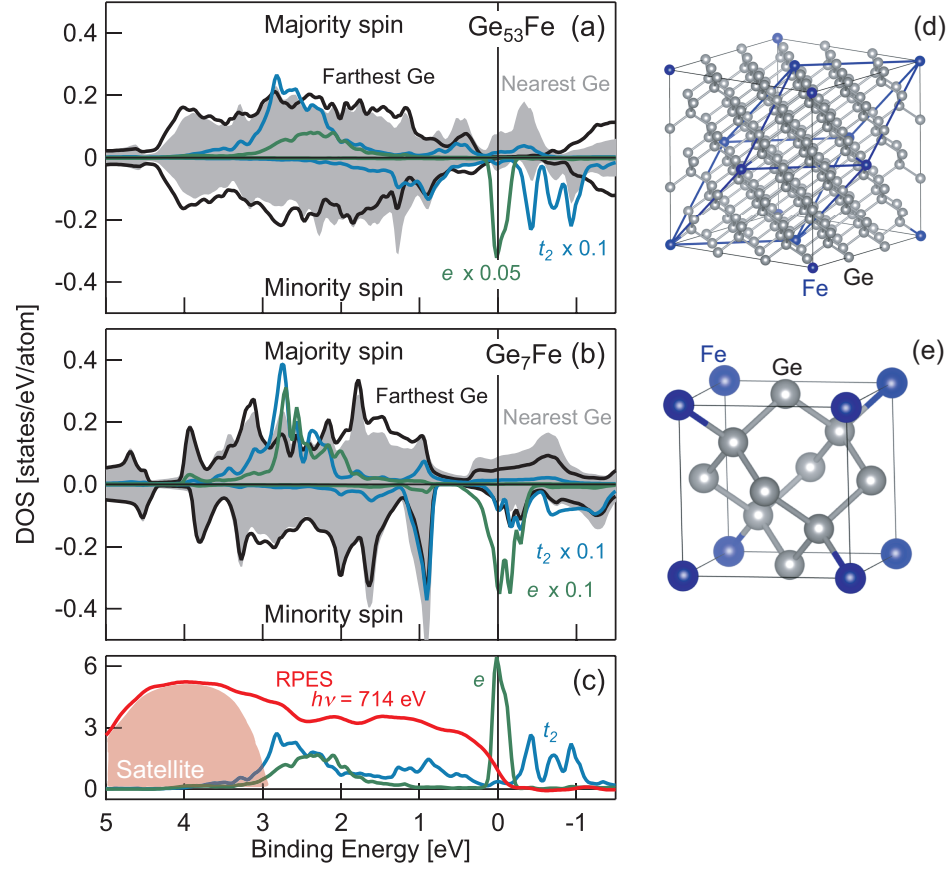
Figure 4.4: Spin-resolved partial densities of states (PDOSs) of $Ge_{53}Fe$ (a) and Ge_7Fe (b) supercells. The supercells are illustrated in the upper-left corner of each panel [112], and the primitive cell of $Ge_{53}Fe$ is indicated by blue lines inside the cubic cell. Black curve and gray area represent the PDOS of the farthest and the nearest Ge atom to the Fe atom, respectively, and blue and green curves represent the PDOS of the Fe $3d$ t_2 and e states of Fe, respectively. The PDOS of the t_2 and e states have been scaled by a factor of 0.05 or 0.1 for the sake of comparison with the PDOS of Ge. (c) Spin-averaged PDOS of the Fe t_2 and e orbitals of the $Ge_{53}Fe$ supercell. The experimental spectrum is superposed by a red curve.

4.3.3   First-principles Calculation

In order to investigate the electronic structure of a Fe atom substituting a Ge atom in the Ge host in comparison with a Mn atom substituting Ga in the GaAs host, we calculated the spin-resolved PDOSs of the $Ge_{53}Fe$ supercell (Fe 1.85%) and the Ge_7Fe supercell (Fe 12.5%) as shown in Figs. 4.4(d) and

(e), respectively. Since Fe-rich (10%) and Fe-poor (4%) regions coexist in the real system [45], the calculated electronic structures of $Ge_{53}Fe$ would explain the properties of the Fe-poor regions, and those of Ge_7Fe the Fe-rich regions. Although the situation is different in the real system with random Fe distribution, to study the supercells is a good starting point to elucidate the underlying physics. In Figs. 4.4(a) and (b), gray area and black curve represent the PDOS of the Ge atoms nearest to and farthest from the Fe atom, and blue and green curves represent the PDOS of Fe $3d$ t_2 (d_{xy} ,d_{yz}, and d_{zx}) and e ($d_{x^2-y^2}$ and d_{z^2}) orbitals, respectively. In the case of $Ge_{53}Fe$ (Fig. 4.4(a)), the PDOS of the farthest Ge is not affected by the presence of Fe significantly. Therefore, the Fe atom in this supercell can be considered as an isolated impurity. On the other hand, the PDOS of the nearest Ge is strongly affected due to the hybridization with Fe $3d$ states (mainly with t_2), in particular within ∼0.5 eV of E_F, as in the case of (Ga,Mn)As. A significant difference between Ge:Fe and (Ga,Mn)As is that there is an additional Fe $3d$ electron in Ge:Fe which occupies the minority-spin e states at the Fermi level. This means that Fe is in the Fe^{2+} state with $3d^6(sp)^2$ configuration. This is consistent with a previous calculation on a $2 \times 2 \times 2$ Ge supercell having a neighboring Fe-Fe pair [113], although the $3d(e)$ states was split into bonding and anti-bonding states due to the overlap of the d orbitals of paired Fe atoms in that calculation. The p-$d(t_2)$ hybridized states in Ge:Fe is pushed from the VBM into the band gap of host Ge and act as deep acceptor levels, which agrees with the experimental finding that the Fermi level was in the middle of the band gap.

In the case of Ge_7Fe (Fig. 4.4(b)), the PDOS of both nearest and farthest Ge atoms are significantly modified because of the high concentration of Fe. The band widths of the Fe $3d$ levels and p-d hybridized levels in Ge_7Fe are broader than those of $Ge_{53}Fe$ especially near and above the Fermi level due to the shorter Fe-Fe distance. It should be mentioned, however, that the relative energy positions of different Fe $3d$ levels in Ge_7Fe is the same as those in $Ge_{53}Fe$, and the basic electronic structures are not altered qualitatively.

Figure 4.4(c) shows the spin-averaged PDOS of Fe t_2 and e orbitals of $Ge_{53}Fe$ in comparison with the experimentally obtained PDOS. Except for the feature around 4 eV, which was attributed to a satellite, the calculated PDOS agrees with the experiment at least qualitatively, that is, both PDOS have a finite value at E_F and extend down to ∼3 eV below E_F.

A schematic energy-level diagram of the electronic structure of Ge:Fe thus obtained is shown in Fig. 4.5(a) and that of (Ga,Mn)As in Fig. 4.5(b). In both cases, the local T_d crystal symmetry around the transition-metal atom makes the d levels split into two sublevels, the doubly degenerate e level and
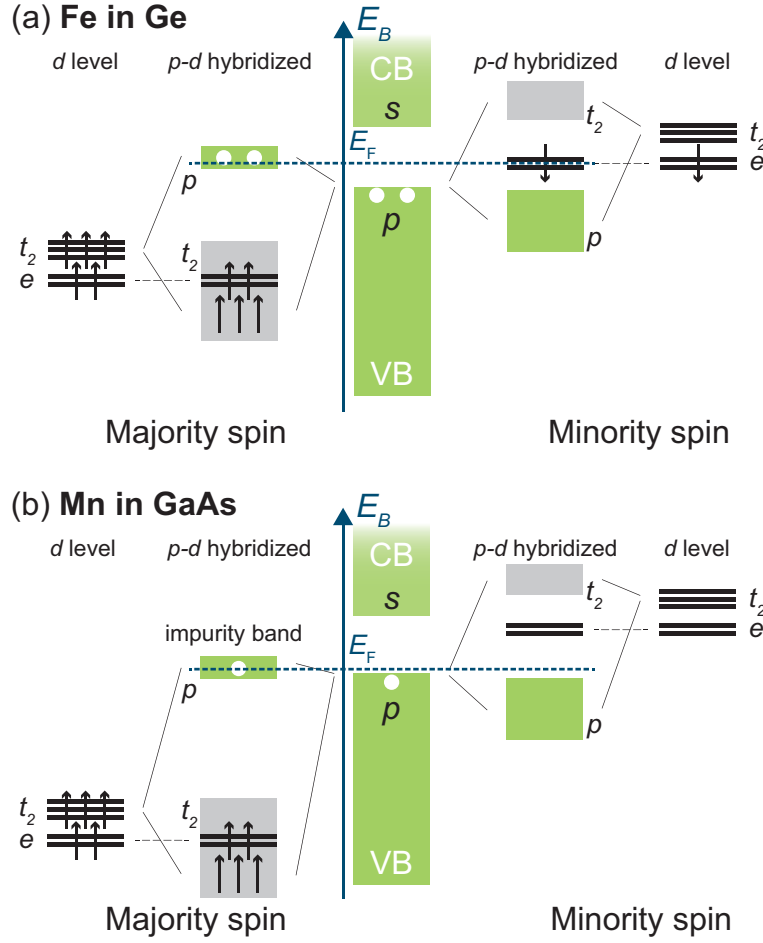
Figure 4.5: Schematic energy-level diagram of (a) Ge:Fe and (b) (Ga,Mn)As. The valence band (VB) and the conduction band (CB) of the host semiconductor are shown at the center of each panel, and the majority-spin and minority-spin d levels are shown at the left- and right-hand sides of each panel, respectively. In addition, energy levels with p-d hybridization are shown in between, where green and gray boxes represent the state with predominant p and t_2 character, respectively.

the triply degenerate t_2 level. In the presence of p-d hybridization (predominantly p-t_2 hybridization), the majority-spin t_2 levels are shifted downwards and the minority-spin t_2 levels upwards. At the same time, some p states are split from the VBM: majority-spin levels are shifted upward and minority-spin ones downward. Note that, as a result of the p-$d(t_2)$ hybridization, the shifted levels have both p and $d(t_2)$ characters. In Fig. 4.5 the states with predominant t_2 and p character are indicated by gray and green boxes, respectively,

and we refer to the lower levels as bonding levels, and the upper as antibonding levels hereafter. In the case of (Ga,Mn)As, the majority-spin d levels are almost fully occupied and the minority-spin d levels are nearly empty. Mn is in the Mn^{2+} state with five majority-spin d electrons and one p hole. Due to the strongest Hund's coupling of the Mn^{2+} state with d^5 configuration, the majority-spin d levels are located well below E_F, while the minority-spin d levels well above E_F. Therefore, the hole enters the majority-spin antibonding levels with predominant p characters split-off from the VBM and acts as a shallow acceptor level. On the other hand, the Fe atom substituting for Ge should have six $3d$ electrons and provides two p holes from the electron counting argument. The majority-spin d levels of Ge:Fe are shallower in energy than those of (Ga,Mn)As because of the reduced Hund's energy, and p-$d(t_2)$ hybridization becomes stronger. Consequently, the majority-spin antibonding levels are pushed well above the VBM compared to the Mn case and even above the minority-spin e level. The sixth d electrons of Fe thus occupy the doubly degenerate minority-spin e states and the two p holes reside in the majority-spin anti-bonding states of the deep acceptor-level origin. If the Fe concentration is high enough and Fe-Fe interaction is non-negligible, the band widths of the Fe $3d$ levels including the minority-spin e level become broader as mentioned above and shown in Fig. 4.4(b). Accordingly, since the minority-spin e band is almost half-filled, double-exchange mechanism would become effective. This is probably the case for the Fe-rich regions in this material.

From the above considerations, we conclude that the valence-band model is not applicable in a different sense from the (Ga,Mn)As case. The majority-spin p-$d(t_2)$ hybridized levels located above the VBM seem responsible for the charge transport and the non-dispersive Fe $3d$ intensity at E_F observed by the resonance ARPES measurements. On the other hand, the narrow-band or nearly localized Fe e electrons probably play an essential role in stabilizing the ferromagnetism through a double-exchange-like mechanism between neighboring Fe atoms. The present picture explains the observed increase of T_C with Fe concentration [94] and with the inhomogeneity of Fe distribution [45, 54]. The same picture explains the observation of robust nanoscale ferromagnetic domains formed in Fe-rich regions well above the T_C [55].

4.4 Summary

In summary, we have performed SX-ARPES measurements and first-principles supercell calculation on Ge:Fe. ARPES spectra showed that the Fermi level is located at 0.35 eV above the VBM and that non-dispersive Fe $3d$ states exist

at the Fermi level, which was attributed to majority-spin p-$d(t_2)$ antibonding states of deep acceptor-level origin, and also to minority-spin Fe $3d(e)$ states. Combining the ARPES result with the results of supercell calculations and the previous XMCD study, it is concluded that charge transport occurs through the majority-spin impurity band of the deep acceptor-level origin, and that the ferromagnetic interaction is mediated by double-exchange interaction within the nearly localized minority-spin Fe $3d(e)$ band.

Chapter 5

XMCD, RPES, and First-Principles Calculation Studies of (Ga,Fe)Sb

5.1 Introduction

In Fe-doped III-V FMSs, if Fe substitutes for the In^{3+} or Ga^{3+} site and takes the stable valence of 3+ with the $3d^5(4sp)^3$ configuration, no charge carrier will be provided and hence both n- and p-type conduction would be possible via additional carrier doping. In fact, (Al,Fe)Sb is insulating, (In,Fe)As:Be n-type, where doped interstitial Be atoms act as double donors, and (Ga,Fe)Sb p-type, where native charged defects such as Ga anti-sites are thought to act as acceptors and provide holes. It has been found that the distribution of Fe atoms is non-uniform in these systems, which seems to play an important role in stabilizing the ferromagnetic order [42, 46, 52], as also discussed in preceding chapters.

In this chapter, we have studied the electronic structure and the magnetic properties of (Ga,Fe)Sb epitaxial thin films by XAS, XMCD, RPES, and first-principles supercell calculation.

5.2 Experiment and Calculation

$Ga_{1-x}Fe_xSb$ films with two different Fe contents $x = 6.0$ and 13.7% (referred to as sample A and B, respectively) were grown on GaAs(001) substrates using the low-temperature molecular beam epitaxy (LT-MBE) method by Dr. Nguyen Thanh Tu from Prof. Masaaki Tanaka's group at the department of electrical

engineering, the University of Tokyo. To relax the lattice mismatch between (Ga,Fe)Sb and GaAs, three buffer layers were inserted; initially GaAs (50 nm) and AlAs (10 nm) layers were successively grown at the substrate temperature T_S of 550 °C, and then AlSb (100 nm) layer at $T_S = 470$°C. After growing the buffer layers, the (Ga,Fe)Sb layer of 50 nm thickness was grown. Here, the T_S was set to 200 °C for sample A and 250 °C for sample B. Lastly sub-nanometer-thick amorphous As cap layer was deposited to prevent surface oxidation. Note that sample A was paramagnetic down to 5 K, and sample B was ferromagnetic with $T_C = 170$ K. In order to remove the oxidized surface, we etched the sample by hydrochloric acid (HCl) (2.4 mol/L) for 5 seconds and subsequently rinsed it by water just before loading the sample in the vacuum chamber of the spectrometer [91, 114].

All the measurements were performed at beam line BL23SU of SPring-8. Circularly polarized x rays of 690 - 780 eV were used for both absorption and photoemission measurements. For XMCD measurements, the magnetic field was applied parallel to the incident x rays and perpendicular to the sample surface. Absorption signals were taken in the total electron yield (TEY) mode, and dichroic signals were measured by reversing the helicity of x rays with 1 Hz frequency at each photon energy under a fixed magnetic field. In order to eliminate spurious XMCD signals, the scans were repeated with opposite magnetic field directions. Each XMCD spectrum was obtained as the average, namely, $((\sigma_{+,h} - \sigma_{-,h}) + (\sigma_{-,-h} - \sigma_{+,-h}))$, where σ denotes the absorption cross-sections, the first subscript the helicity of x rays, and the second subscript the sign of the magnetic field. XAS was obtained as the summation of all the four terms. Note that two-step inverse tangent function representing the Fe $L_{2,3}$-edge jumps were subtracted from each term [67].

For RPES measurements, the sample temperature was set to 100 K, and the energy resolution was about 150 meV. The samples were placed so that the [-110] direction became parallel to the analyzer slit and perpendicular to the beam. Photoelectrons were collected in the normal emission geometry with 45-degree light incidence.

First-principles calculations were performed on a 3×3×3 GaSb supercell with one substitutional Fe atom, namely, $Ga_{26}Fe_1Sb_{27}$ (3.7% Fe), using the full-potential augmented-plane-wave method as implemented in the WIEN2k code [83]. The experimental lattice constant of 6.085 Å, estimated from Vegard's law in Ref. [42], was used for the calculation. For the exchange-correlation potential, the generalized gradient approximation (GGA) of Perdew-Burke-Erzerhof parametrization [82] was employed with/without the empirical Hubbard U (GGA+U) [115] accounting for the on-site Coulomb correlation of Fe

$3d$ electrons. Spin-orbit interaction was also included.

5.3   Results and Discussion

5.3.1   XAS and XMCD

Figures 5.1(a) and 5.1(b) show XAS and XMCD spectra of the present
(Ga,Fe)Sb films after the HCl etching compared with those of (In,Fe)As:Be [52],
Fe metal [67], $FeCr_2S_4$ [87], and γ-Fe_2O_3 [88]. Note that the Fe $3d$ electrons in
$FeCr_2S_4$ and γ-Fe_2O_3 are localized, and that the valence of Fe is 2+ in $FeCr_2S_4$
and 3+ in γ-Fe_2O_3. The line shapes of the spectra of the two (Ga,Fe)Sb films
resemble those of bcc Fe metal rather than the sharper spectra of $FeCr_2S_4$,
manifesting the itinerant nature of the Fe $3d$ electrons in (Ga,Fe)Sb. Although
the spectral line shapes of the two (Ga,Fe)Sb films look almost identical, rep-
resenting nearly the same electronic structure, the intensity of the XMCD sig-
nals was significantly suppressed for the 6% Fe-doped sample compared to the
13.7% Fe-doped sample simply because only the 13.7% Fe-doped sample ex-
hibits ferromagnetism while the 6% Fe-doped one is paramagnetic at 5 K. Such
an insensitivity of the line shape to transition-metal content was also reported
for (Ga,Mn)As [116], (In,Fe)As:Be [52], etc.

In addition to the main peak at ∼708 eV, there is a shoulder at ∼710
eV, which is more evident in XAS than in XMCD. This can be attributed
to Fe^{3+} oxides formed at the surface because the feature at ∼710 eV was
prominent before etching and disappeared almost completely after etching, as
shown in Fig. 5.2. Here, the spectra of both paramagnetic and ferromagnetic
samples after etching resemble those of Ge:Fe and (In,Fe)As:Be. Using these
two spectra containing the different degrees of contribution from surface oxides,
it was possible to deduce the intrinsic spectra as $[XAS]_{int} \propto [XAS]_a - p[XAS]_b$.
Here, $[XAS]_a$ and $[XAS]_b$ denote the XAS spectrum after and before etching,
respectively, and p was chosen so that the shoulder at ∼ 710 eV vanished, or
the second derivative of $[XAS]_{int}$ did not show a peak at ∼710 eV as shown
in the inset of Fig. 5.2. The extrinsic contribution from the surface oxides
to the XAS spectra was also extractable in a similar manner as $[XAS]_{ext} \propto$
$[XAS]_a - q[XAS]_b$, where q was chosen so that $[XAS]_{ext}$ became identical to the
spectra of α-Fe_2O_3 shown by the green dashed curve. Thus obtained intrinsic
and extrinsic components are separately shown in Fig. 5.2 by red and orange
dashed curves, respectively, for both spectra before and after etching. From
this procedure, it was found that the extrinsic contribution to the XAS was
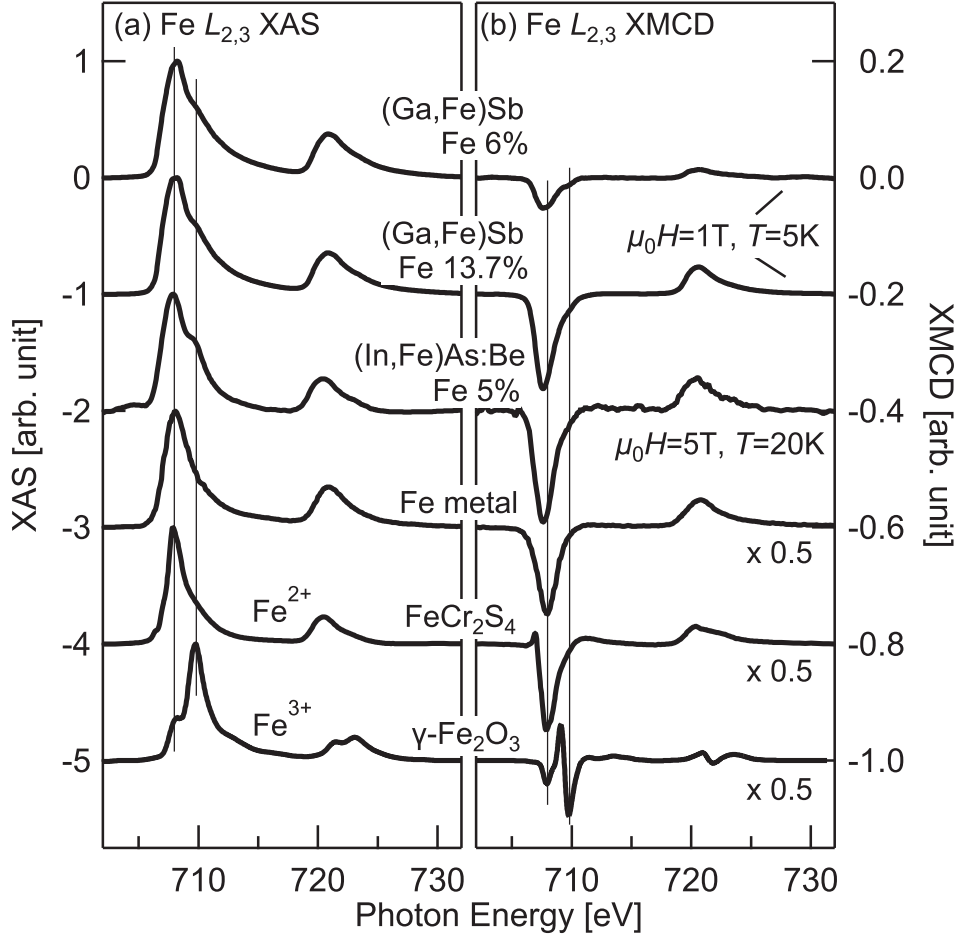almost ∼ 60 % before etching, and was significantly reduced to ∼ 4% after

Figure 5.1: XAS (a) and XMCD (b) spectra of (Ga,Fe)Sb compared with those of (In,Fe)As:Be [52], bcc Fe (Ref. 37) [67], $FeCr_2O_4$ [87], and γ-Fe_2O_3 [88]. The XMCD spectra of bcc Fe, $FeCr_2O_4$, and γ-Fe_2O_3 are multiplied by 0.5 for ease of comparison.

etching, which guarantees the efficiency of HCl etching.

One may suspect that, because the spectra look similar to those of bcc Fe, the magnetism may originate from nanoscale metallic Fe precipitates in the samples. In order to rule out this possibility, details of the "intrinsic XAS" and XMCD spectra at the Fe L_3 edge are shown in the inset of Fig. 5.2 together with the second derivative XAS spectrum to highlight weak shoulders on the XAS spectrum labeled $a - d$. Here, the signs of XMCD and the second derivative XAS spectra are reversed for ease of comparison. The XAS spectrum of (Ga,Fe)Sb mainly consists of two features c and d, which do not coincide with the feature in XMCD (labeled b). This is not the case for bcc Fe, where
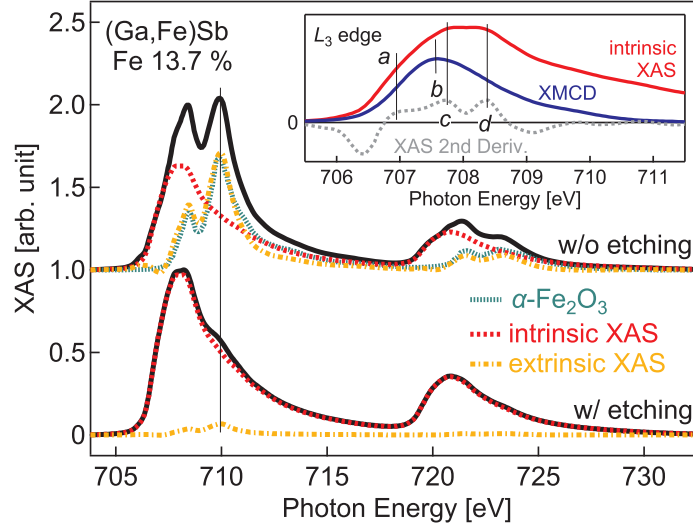
Figure 5.2: XAS and XMCD spectra of the 13.7% Fe-doped (Ga,Fe)Sb before
and after HCl etching. Intrinsic and extrinsic components are also separately
shown by red and orange dashed curves, respectively, together with the spec-
trum of α-Fe_2O_3. Inset shows the intrinsic XAS and XMCD spectra expanded
at the Fe L_3 edge. Second derivative of the XAS spectrum is also shown to
emphasize weak features, labeled as a-d. Here, the signs of the XMCD and the
second derivative spectrum have been reversed.

the XAS spectrum consists of a broad single peak, and the peak positions of
XAS and XMCD indeed coincide [52]. Such a peak-position difference was also
found in (In,Fe)As:Be [52] and Ge:Fe [55], and might be a universal spectral
feature of Fe-doped semiconductors. Note that there is also a shoulder at $\sim$710
eV in the XMCD spectra originating from Fe^{3+} oxides, but the contribution is
much smaller.

By applying the XMCD sum rules, we have estimated the spin and orbital
magnetic moments of Fe [64, 65] as follows.

$$m_{\mathrm{orb}} = -\frac{4 \int_{L_{2,3}} \mathrm{XMCD}\ \mathrm{d}\omega}{3 \int_{L_{2,3}} \mathrm{XAS}\ \mathrm{d}\omega} n_h, \tag{5.1}$$

$$m_{\mathrm{spin}} = -\frac{6 \int_{L_3} \mathrm{XMCD}\ \mathrm{d}\omega - 4 \int_{L_{2,3}} \mathrm{XMCD}\ \mathrm{d}\omega}{\int_{L_{2,3}} \mathrm{XAS}\ \mathrm{d}\omega} n_h, \tag{5.2}$$

where m_{orb} and m_{spin} are the orbital and spin magnetic moments in units of
μ_{B}, respectively, and n_h the number of $3d$ holes. Here, we have ignored the
magnetic dipole term, which is negligibly small for an atomic site with high

Table 5.1: Spin and orbital magnetic moments of Fe in (Ga,Fe)Sb in comparison with those of (In,Fe)As:Be, Ge:Fe, and bcc Fe metal. All the values have been estimated using the XMCD sum rules except for the ones in the third and the forth rows, which were computed using the GGA and GGA+U methods.

	$m_{\mathrm{orb}}/m_{\mathrm{spin}}$	m_{orb}	m_{spin}
$Ga_{0.94}Fe_{0.06}Sb^*$	0.13 ± 0.01	$0.05^\dagger$	$0.37^\dagger$
$Ga_{0.863}Fe_{0.137}Sb^*$	0.13 ± 0.01	$0.14^\dagger$	$1.07^\dagger$
$Ga_{26}Fe_1Sb_{27}$ (GGA)	0.051	0.157	3.08
$Ga_{26}Fe_1Sb_{27}$ (GGA+U)	0.051	0.163	3.17
$In_{0.9}Fe_{0.1}As:Be^{**}$ [52]	0.075 ± 0.015	$0.21^\ddagger$	$2.80^\ddagger$
$In_{0.9}Fe_{0.1}As:Be^*$ [52]	0.10 ± 0.02	$0.17^\ddagger$	$1.75^\ddagger$
$Ge_{0.935}Fe_{0.065}{}^*$ [55]	0.11 ± 0.03	$0.14^\dagger$	$1.29^\dagger$
Fe bcc [67]	0.043 ± 0.001	0.085	1.98

†Values at $\mu_0 H = 1$ T and $T = 5$ K; ‡ Values at 5 T and 20 K; *Fe^{2+} configuration was assumed; **Fe^{3+} configuration was assumed.

symmetry such as T_d or O_h [66]. n_h was set to 4 assuming the valence of Fe is 2+ with six $3d$ electrons as implied by the DFT calculation described below ($n_h = 3.95$). The correction factor of 0.875 for Fe^{2+} ion [68, 69] was used to estimate the spin magnetic moment. The raw XAS and XMCD spectra are used for the sake of simplicity because extrinsic contribution was only a few percent.

Table 5.1 summarizes the spin and orbital magnetic moments of various Fe compounds including other Fe-doped semiconductors and bcc Fe. The results of the present supercell GGA(+U) calculations on $Ga_{26}Fe_1Sb_{27}$ are also shown. It was found that the experimental $m_{\mathrm{orb}}/m_{\mathrm{spin}}$ ratio of (Ga,Fe)Sb is substantially larger than that of bcc Fe. This is may be due to the stronger localization of Fe $3d$ electrons [117] in bulk (Ga,Fe)Sb or at the interface between o the Fe-rich regions and Fe-poor regions, where the translational symmetry is broken [118]. The large value of $m_{\mathrm{orb}}/m_{\mathrm{spin}}$ indicates that the valence of Fe is 2+ with six $3d$ electrons plus one p hole ($3d^6\underline{L}$) because the orbital magnetic moments would be quenched if Fe took the high-spin Fe^{3+} ($3d^5$) configuration. Note that the $m_{\mathrm{orb}}/m_{\mathrm{spin}}$ ratio is more unambiguous than the absolute values of m_{orb} and m_{spin} since it does contain neither the uncertainty in estimating n_h nor extrinsic contributions to the XAS area. In fact, there is still a possibility that the XAS spectra contain Fe^{2+} oxides signals, which leads to the underestimation of m_{orb} and m_{spin}. The deduced spin magnetic moments for both the paramagnetic and ferromagnetic samples are small (0.37 μ_{B}/Fe and

1.07 μ_B/Fe, respectively) compared to the theoretical values. If the theoretical
value of the total moment of $3.24\mu_B$ is assumed, the induced magnetic moment
of the paramagnetic sample would become 0.74 μ_B at $T = 5$ K and $\mu_0 H = 1$
T following the Brillouin function. The cause of the small deduced magnetic
moment is unclear at this stage, but it can be attributed to antiferromag-
netic interaction between the Fe spins, most likely between adjacent Fe atoms
through superexchange interaction, or to the possible existence of Fe^{2+} oxides
component in the XAS spectra. Quantitative estimates of the ferromagnetic,
paramagnetic, and antiferromagnetic components would be possible through
temperature- and field-dependent XMCD measurements [52].

5.3.2   Resonance Photoemission

Figures 5.3(a) and 5.3(d) show RPES spectra of the 6% and 13.7% Fe-doped
samples, respectively, taken across the Fe L_3 absorption edge from 705 eV to 716
eV. The color and the baseline positions represent the photon energies indicated
by triangles on the XAS spectra in Figs. 5.3(c) and 5.3(f). Here, off-resonance
spectra taken with the photon energy of 704 eV shown in Figs. 5.3(b) and
5.3(e) have been subtracted to emphasize the resonance behavior. Note that
the units of the vertical axes of Figs. 5.3(a), 5.3(b), 5.3(d), and 5.3(e) are the
same. For both samples with different Fe contents, a strong normal Auger peak
dispersing with incident photon energy was observed. This suggests that the Fe
$3d$ electrons in (Ga,Fe)Sb have itinerant character, as already suggested by the
XAS measurements, since Auger decay is a consequence of faster screening of
the core hole than the recombination of the excited electron with the core hole
and is normally observed in metallic systems [75,107]. Such a strong Auger peak
was also observed in the case of Fe-doped Ge [91] as presented in Chapter 4.
In addition to the Auger peak, there are resonantly enhanced features around
-1.7 eV and -10.3 eV, denoted by α and β, respectively. Unlike the Auger
peak, these peaks do not disperse with incident photon energy, representing a
local excitation of Fe $3d$ states including charge transfer from ligand orbitals
accompanying the photoemission process. Such resonance features are widely
observed in transition-metal oxides, where the $3d$ electrons are well localized
and strongly correlated [72, 73, 119, 120]. Those local excitation peaks were
almost absent in the case of Fe-doped Ge (Ref. [91]), suggesting that Fe $3d$
electrons in (Ga,Fe)Sb are more correlated or more localized than those in
Ge:Fe. Considering that the Fe $3d$ density of states (DOS) should not be
located as deep as 10 eV below E_F, at least feature β can be attributed to
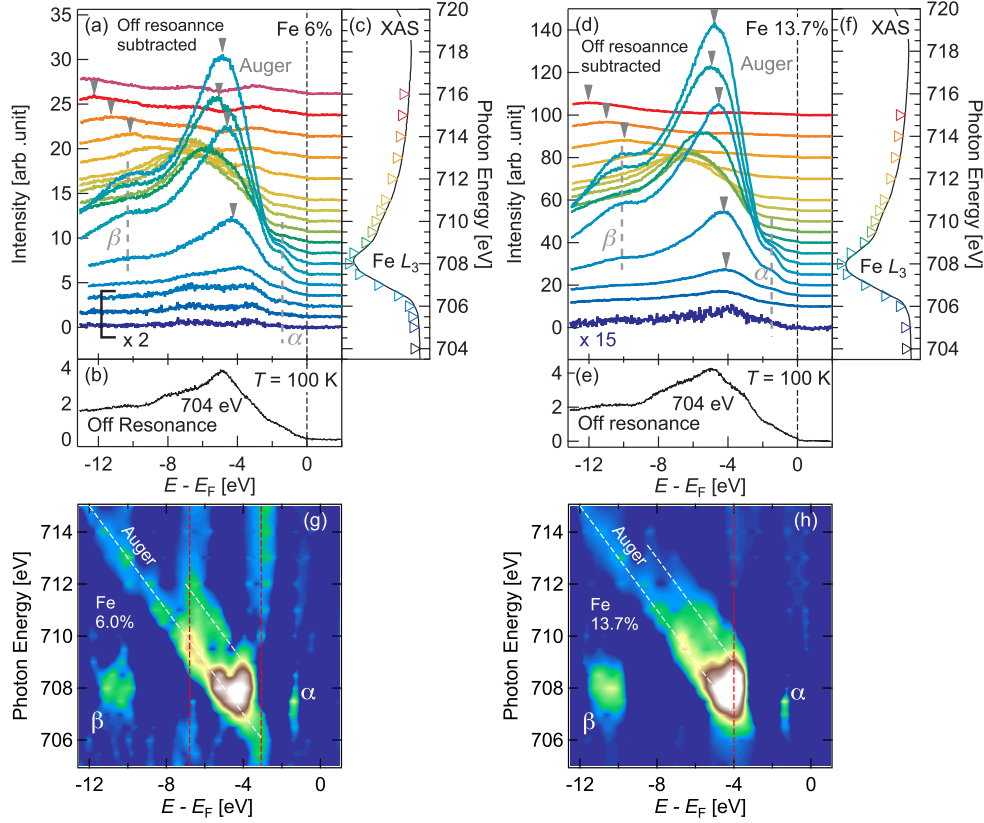a charge-transfer satellite. In order to highlight subtle features, the second

Figure 5.3: (a), (d) Resonance photoemission spectroscopy (RPES) spectra of (Ga,Fe)Sb with 6% Fe and 13.7% Fe taken with photon energies across the Fe L_3 absorption edge. The color and the base line positions of the spectra represent the photon energies as depicted by triangles on the XAS spectra in panels (c) and (f). Here, the off-resonance spectra shown in panels (b) and (e) have been subtracted from all the spectra. (g), (h) False color plots of the second derivatives of the RPES spectra in panels (a) and (d). The dispersive normal Auger peak and the non-dispersive resonance features are indicated by white dashed lines and red solid lines, respectively.

derivative image of the RPES spectra are shown in Figs. 5.3(g) and 5.3(h), where dispersive normal Auger peak and resonantly enhanced peaks α and β can be seen as described above. These features are commonly seen in by both samples, however, there exists a difference as indicated by red dashed lines in Figs. 5.3(g) and 5.3(h). For the 6% Fe sample, two features are observed around 6.8 eV and 3.1 eV in the entire photon energy range, while for the 13.7% Fe sample, there is only one feature around 4 eV. This may imply the difference in the electronic structure between the two samples. Probably the
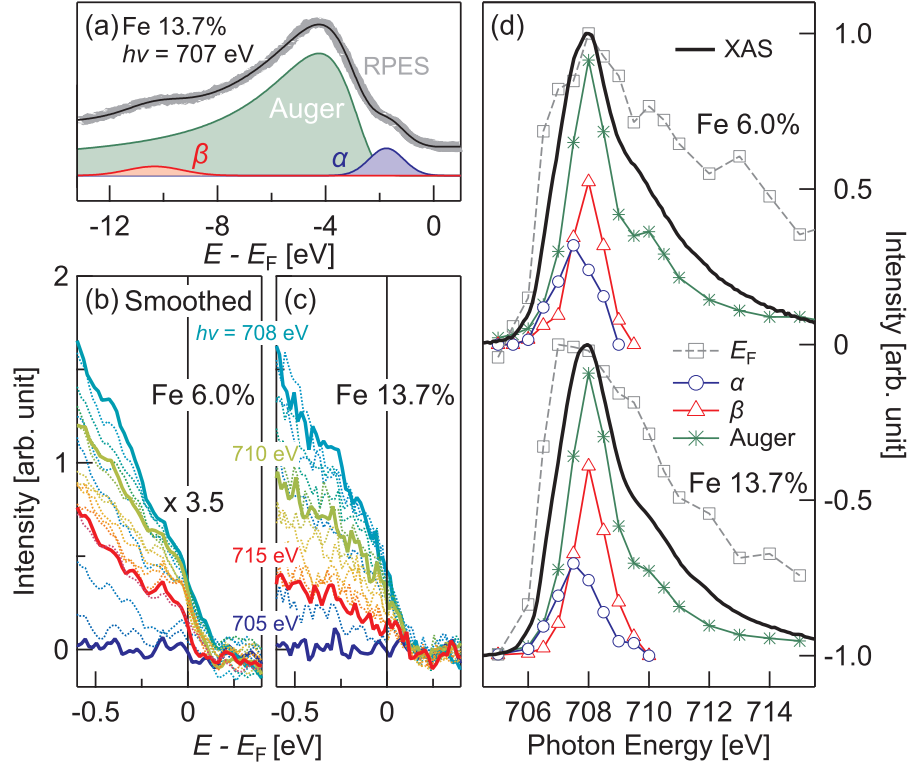
Figure 5.4: (a) RPES spectrum of the 13.7% Fe-doped sample taken with
$h\nu = 707$ eV (gray thick curve) and fitting results (black curve). Fitting
components of two Gaussian functions for features α and β and one asymmetric
Gaussian function for Auger peak are also shown separately. (b), (c) RPES
spectra of the 6% and 13.7% Fe-doped samples near E_F. Here, the color is the
same as those used in Figs. 5.3(a) and 5.3(d). Note that the RPES spectra of
the 6% Fe-doped sample have been smoothed and multiplied by 3.5 for easy
comparison. (d) Constant-initial-state (CIS) spectra for features α and β, and
the intensity at E_F and the Auger peak intensity as functions of photon energy.
For comparison, XAS spectra are also plotted.

$3d$ states are more localized or more correlated in the 6% Fe-doped sample
because the distance between adjacent Fe atoms are longer and the Fe $3d$ band
width would be narrower than in the 13.7% Fe-doped sample.

For the purpose of examining the nature of resonance enhancement, it is
useful to plot the intensity at a fixed binding energy as a function of incident
photon energy, namely, a constant-initial-state (CIS) spectrum. In order to
eliminate the effect of the overlapping Auger peak from the CIS spectra and
to extract the resonance behavior of features α and β, we have employed curve

fitting as shown in Fig. 5.4(a). In the figure, resonance peaks α and β are fitted to Gaussian functions and the Auger peak with its tail is fitted to an asymmetric Gaussian function introduced in Ref. [121]. CIS spectra for features α and β were obtained from the peak areas of the Gaussian functions. This is an *ad hoc* procedure, but still it provides a reasonable description of the resonance enhancement.

Figures 5.4(b) and 5.4(c) show the RPES spectra on an expanded scale near E_F. The data of the 6% Fe-doped sample have been smoothed and multiplied by 3.5 for ease of comparison with the data of the 13.7% Fe-doped sample. As can be seen from the figures, the spectral intensities at E_F for both samples are enhanced on resonance, suggesting that Fe $3d$ states have finite contribution to the DOS at E_F. Here, the CIS spectrum at E_F is defined as the area of RPES spectra between $E - E_F = -0.6$ eV and 0.2 eV.

Thus obtained CIS spectra for features α, β, and the intensity at E_F are plotted in Fig. 5.4(d) together with the Auger peak height as a function of photon energy and the XAS spectra. The CIS spectrum for feature α is peaked at $h\nu = 707.5$ eV, but that for feature β is peaked at a higher photon energy of $h\nu = 708$ eV for both samples. The difference in the CIS peak positions implies that the broad XAS spectra actually consist of different kinds of excitations, which may correspond to peaks c and d in the inset of Fig. 5.2, probably involving different types of $3d$ orbitals, *i.e.*, t_2 and e orbitals, rather than excitation into a single kind of broad metallic bands as in the case of bcc Fe metal. We note that the CIS spectra of features α and β vanish around the photon energy of 710 eV at which the extrinsic Fe^{3+} shoulder exists on each XAS spectrum. Therefore, the observed resonance features are not originated from surface oxides but are most likely intrinsic.

5.3.3   First-principles Calculations

Figures 5.5(a) shows the calculated spin-resolved DOS of the $Ga_{26}Fe_1Sb_{27}$ supercell using the GGA method. The figure shows the total DOS, the Fe t_2 (d_{xy}, d_{yz}, and d_{zx}) and e ($d_{x^2-y^2}$ and $d_{3z^2-r^2}$) PDOS, and the PDOS of Sb atoms nearest to and farthest from the Fe atom are shown. For ease of comparison, the total DOS has been divided by 54 (the number of atoms in the supercell), and the PDOS of the e orbitals and that of the t_2 orbitals have been multiplied by 0.05 or 0.1. Note that, because the PDOS of the farthest Sb atoms is not strongly affected by the presence of Fe atoms, the Fe atom in the supercell can be thought of as an isolated impurity.

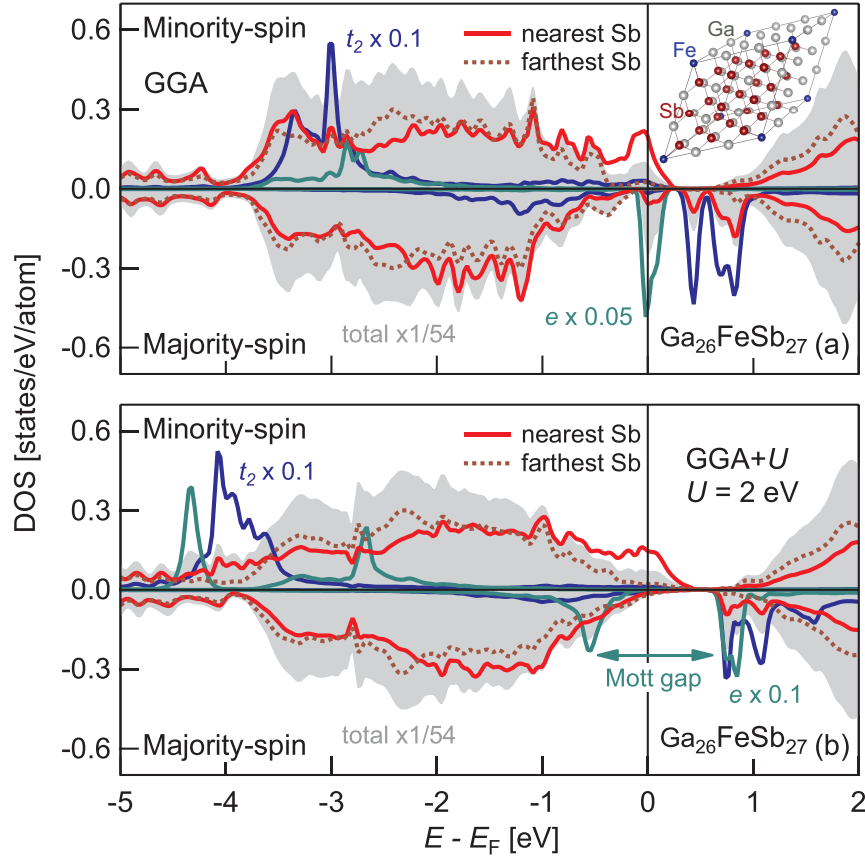On the basis of the calculated DOS, the energy-level diagram of (Ga,Fe)Sb is

Figure 5.5: Spin-resolved density of states (DOS) of a $Ga_{26}FeSb_{27}$ supercell
calculated using GGA (a) and GGA+U ($U = 2$ eV) (b) methods. The structure
of the supercell is illustrated in the inset of panel (a). The total DOS divided
by the number of atoms in the supercell is plotted by gray area, the PDOS of
the Fe e and t_2 orbitals are shown by green and blue curves, respectively, and
the PDOS of Sb atoms nearest to and farthest from the Fe atom are shown by
a red solid curve and a purple dashed curve, respectively.

schematically depicted in Fig. 5.6. In the figure, those levels with predominant
t_2 and p character are indicated by gray and green boxes, respectively. At the
substitutional sites, the Fe $3d$ levels are split into the doubly-degenerate lower
e levels and the triply-degenerate higher t_2 levels due to the crystal field of T_d
symmetry as shown in the figure. Due to the strong p-$d(t_2)$ hybridization, the Fe
t_2 orbitals and the ligand Sb p orbitals form bonding and anti-bonding states
with mixed t_2 and p character, and the $3d(t_2)$ electrons would thus acquire
itinerant nature. As for the majority-spin states, where the t_2 levels are located
well below the valence-band maximum (VBM) because of the relatively high Sb

$5p$-derived valence-band position [122], the bonding states have predominant Fe t_2 character, and the anti-bonding states predominant Sb p character. On the other hand, the minority-spin bonding states consist primarily of Sb p orbitals, and the anti-bonding levels Fe t_2 orbitals.

As opposed to the initial presumption that the Fe atom takes the valence of 3+ with the $3d^5(4sp)^3$ configuration, the calculation indicates that one electron occupies the e level and that the valence of Fe becomes 2+ with the $3d^6(4sp)^2$ configuration, as implied by the XAS and XMCD measurements. This is due to the low electronegativity of Sb and the high VBM of GaSb [122], which makes electrons preferentially occupy the sixth d level rather than fill the p level. If the $3d^5(4sp)^3$ configuration (Fe^{3+}) were realized, the majority-spin $3d$ states would be fully occupied, the minority-spin $3d$ states would be empty, and no carriers would be provided. In the case of the $3d^6(4sp)^2$ configuration, the sixth $3d$ electron resides in the minority-spin band of e character at the Fermi level, and one hole goes into the majority-spin anti-bonding p-$d(t_2)$ hybridized states as depicted by a white circle in a green box in Fig. 5.6. It is noteworthy that these states are located shallow inside the band gap just above the VBM. This is because the energy shift caused by p-d hybridization, most simply expressed as $t_{pd}^2/(E_p^\uparrow - E_d^\uparrow)$, is not very large, partly due to the fact that VBM, or the p level of GaSb ($E_p^\uparrow$), is high in energy compared to GaAs or InAs [122], making the denominator large. Here, $E_p^\uparrow$ and $E_d^\uparrow$ represent the energy positions of the Sb $5p$ and Fe $3d(t_2)$ levels, respectively, and t_{pd} denotes the transfer integral between Sb $5p$ and Fe $3d$ orbitals.

Interestingly, the energy levels of (Ga,Fe)Sb thus become similar to those of (Ga,Mn)As in terms of the relative positions of the ligand p levels and the majority-spin transition-metal d levels. The VBM of GaAs is lower in energy than that of GaSb, and the $3d$ levels of Mn^{2+} are lower than those of Fe^{2+} $3d$ levels due to the stronger Hund's coupling of Mn^{2+}, which results in the resemblance in the relative positions of the VBM and the d levels between (Ga,Mn)As and (Ga,Fe)Sb. Therefore, one can conclude that there exists long-range ferromagnetic interaction between the Fe magnetic moments mediated by relatively itinerant holes in the p-$d(t_2)$ hybridized states as in the case of (Ga,Mn)As. In fact, the acceptor level of Fe in GaSb was reported to be as shallow as 23 ± 2 meV [123], shallower than the Mn acceptor level of (Ga,Mn)As (110 meV [124]). This can be attributed to a smaller transfer integral t_{pd} between Fe $3d$ and Sb $5p$ orbitals in (Ga,Fe)Sb than between Mn $3d$ and As $4p$ orbitals in (Ga,Mn)As, because the Fe-Sb distance is larger than the Mn-As distance, resulting in smaller orbital overlap. This scenario also explains the linear increase of hole concentration upon Fe doping [42], which was previously attributed to
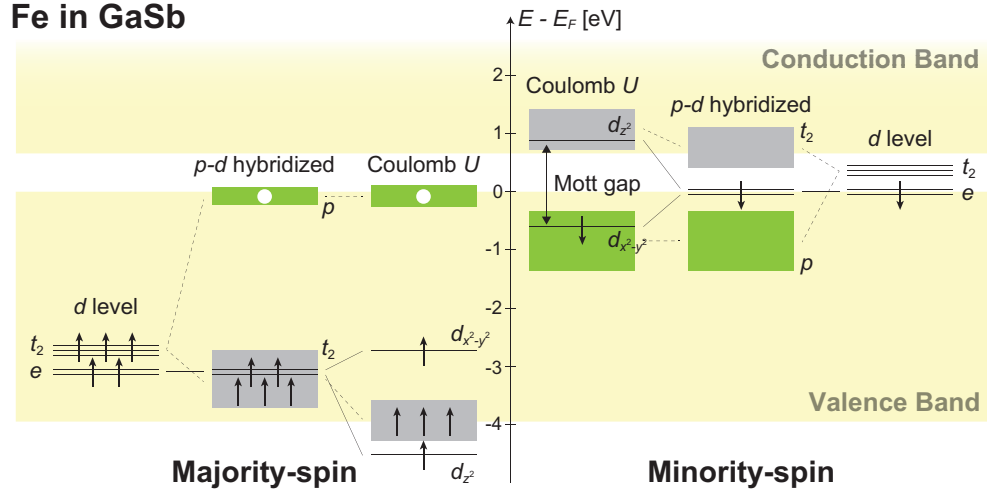
Figure 5.6: Schematic energy diagram of (Ga,Fe)Sb, where, in addition to the d levels of Fe, the valence band and the conduction band of the host GaSb are shown by large yellow boxes as the background. Due to p-$d(t_2)$ hybridization, the t_2 orbitals are split into bonding and anti-bonding states having both p and t_2 characters. States with predominant p and t_2 character are indicated by green and gray boxes, respectively. Furthermore, in the presence of strong correlation, represented by intra-atomic Coulomb energy U, the doubly degenerate e levels are split into lower and upper Hubbard-like bands, opening the gap of $\sim U$ at E_F for the minority-spin bands. Note that d electrons are represented by arrows while p holes by white circles.

defects such as Ga anti-sites.

A significant difference between (Ga,Mn)As and (Ga,Fe)Sb, however, arises from the number of $3d$ electrons. In the case of (Ga,Fe)Sb, Fe^{2+} has an additional sixth $3d$ electron in the minority-spin e bands at the Fermi level as mentioned above, which would affect the magnetism as well as the transport properties. Furthermore, since the minority-spin e band is half-filled at the Fermi level, there would also exist double-exchange interaction between Fe e electrons in addition to the long-range exchange interaction mentioned above. This interaction should be rather short-ranged because of the localized nature of the e electrons, whose hybridization with ligand orbitals is very weak. As the Fe concentration increases or the spatial distribution of Fe becomes inhomogeneous, overlap between the e orbitals will be larger and makes the double-exchange interaction stronger.

In order to discuss the effect of Coulomb interaction between the Fe $3d$ electrons, found in the RPES measurements, we have also performed GGA+U

calculation as shown in Fig. 5.5(b). Here, U was arbitrarily chosen to 2 eV, but the choice of the Hubbard U does not affect the following discussions. If the U parameter is included, the occupied d levels are shifted downwards, while the unoccupied ones upwards. In particular, the half-filled doubly-degenerate minority-spin e levels are split into occupied and unoccupied ones opening a gap in between reminiscent of the lower and upper Hubbard bands of a Mott insulator [125]. This is because the spin direction was set to the [001] direction and the spin-orbit interaction is included in the calculation, the minority-spin $d_{x^2-y^2}$ orbital extending perpendicularly to the spin axis is preferentially occupied while the d_{z^2} orbital unoccupied. As a result, the majority-spin e levels are also split into the $d_{x^2-y^2}$ and d_{z^2} levels due to the difference between inter- and intra-orbital Coulomb interactions. To be more precise, the size of the gap would be $U' - J$ for the minority-spin e levels, and $U - U'$ for the majority-spin counterparts, where U' and U denote inter- and intra-orbital Coulomb interactions and J represents Hund's coupling energy.

In the low Fe-content regime, the Fe $3d(e)$ band width W would be small compared to U ($U/W > 1$) and the gap would survive. In that regime, only p-d exchange mechanism would be effective. This is consistent with the observed T_{C} which follows the relationship of the p-d Zener model [20, 35, 42], namely, $T_{\mathrm{C}} \propto x p^{1/3}$. On the other hand, if the Fe concentration increases or the distribution of Fe atoms becomes inhomogeneous, the band width becomes larger than U ($U/W < 1$) and the gap in the minority-spin e levels is closed. Then, double-exchange interaction within the Fe $3d(e)$ bands would set in and add to the p-d exchange-like mechanism.

In real (Ga,Fe)Sb samples, it has been reported that there is Fe concentration fluctuation especially in heavily Fe-doped samples [42, 43]. Therefore, in Fe-rich regions, double-exchange interaction would stabilize local ferromagnetic domains even above T_{C}, while the macroscopic T_{C} may be determined by long-range p-d exchange interaction. This agrees with the observed convex line shape of M-T curves [42], indicating the existence of superparamagnetism even above T_{C}. To address these issues more precisely, magnetic-field and temperature-dependent XMCD measurements as well as further theoretical investigations are needed.

5.4 Summary

In the present work, we have studied the electronic structure and the magnetism of the novel p-type ferromagnetic semiconductor (Ga,Fe)Sb, whose Curie temperature exceeds room temperature, using XAS, XMCD, RPES, and first-

principles supercell calculations. The line shapes of XAS and XMCD spectra
suggested that the ferromagnetism is of intrinsic origin. XMCD sum rules
yielded an unquenched large orbital moment, implying the $3d^6$ configuration of
Fe. The valence-band RPES spectra showed a dispersive Auger peak and non-
dispersive resonantly enhanced peaks, which are fingerprints of the itinerant
and correlated nature of the Fe $3d$ electrons, respectively. From first-principles
supercell calculations using GGA $(+U)$, it was found that substitutional Fe
takes the valence of 2+ with $3d^6(4sp)^2$ configuration, consistent with the XAS
and XMCD results. This can be another cause of the increase of hole concentra-
tion upon Fe doping, previously attributed to defects such as Ga anti-site. The
calculation also indicated that there are two channels for ferromagnetic order,
namely, short-range double-exchange interaction mediated by the minority-spin
Fe $3d(e)$ electrons and long-range interaction mediated by the hole carriers in
the p-$d(t_2)$ hybridized anti-bonding acceptor states. The latter would deter-
mine the macroscopic T_{C}, while the former would lead to the strong nanoscale
ferromagnetic order in Fe-rich phases even above T_{C}.

Chapter 6

First-Principles Calculations of (III,Fe)V Semiconductors

6.1 Introduction

In Chapters 4 and 5, the results of first-principles calculations of Ge:Fe and (Ga,Fe)Sb supercells are presented. In this chapter, in order to investigate the host-semiconductor dependence of electronic structures, particularly the density of states and the magnitude of spin and orbital magnetic moments, we have performed the same kind of calculations on the series of Fe-doped III-V semiconductors.

6.2 Methods

DFT calculations were carried out using the all-electron full-potential (linearized) augmented-plane-wave plus local-orbital method implemented in the WIEN2k package [83]. The spherical harmonic expansion was made up to $l = 10$ inside the muffin-tin spheres. The used plane-wave cutoff values (K_{max}) and the radii of MT spheres are summarized in Table 6.2. For the exchange-correlation energy functional, the Perdew-Burke-Ernzerhof (PBE) generalized gradient approximation (GGA) was used [82]. In order to simulate the randomly doped system, supercells consisting of $3 \times 3 \times 3$ primitive unit cell of zinc blende structure are employed as shown in the inset of Fig. 6.1. The unit cell contains 27 group-V atoms, 26 group-III atoms, and one Fe atom. This supercell corresponds to 3.7% Fe doping and would be a good starting point to study the basic electronic structure of isolated Fe atoms in the III-V matrix without significant Fe-Fe interactions or hybridizations. The Brillouin zone
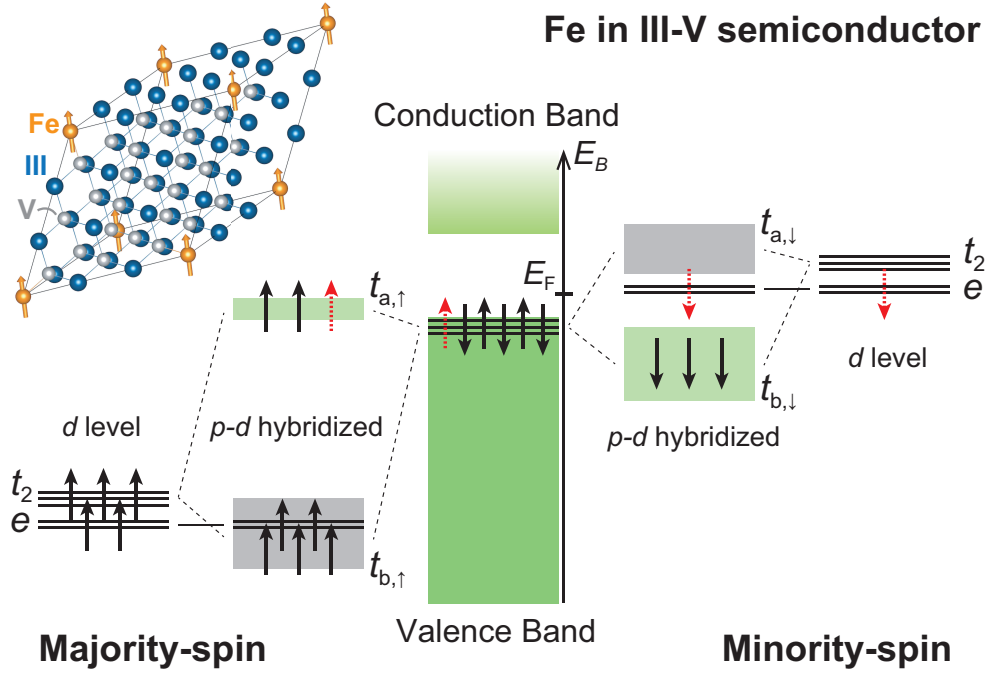
Fe in III-V semiconductor

Figure 6.1: Schematic energy diagram of Fe-doped III-V semiconductors. The valence and conduction bands of the host semiconductors are shown in the middle by green boxes, and the majority-spin and minority-spin $3d$ levels of the Fe atom without p-d hybridization are shown on the left- and right-hand sides, respectively. The energy levels with p-d hybridization are shown in between, where the gray and green colors represent that the states have predominantly Fe $3d$ t_2 and p character. In the inset, a $3 \times 3 \times 3$ supercell consisting of 27 group-V atoms such as As, 26 group-III atoms such as Ga, and one Fe atom is shown.

integration was performed with a $4 \times 4 \times 4$ k-point mesh. The experimental lattice constants of host semiconductors [122] were used for all the calculations for simplicity. Self-consistent calculations were repeated until the calculated total energy converged to within 0.0001 Ry.

6.3   Results

Figure 6.2 shows the spin-resolved total DOSs and partial DOSs (PDOSs) of Fe-doped III-V semiconductors. The total DOSs are indicated by gray areas, and the PDOSs of group-V atoms located nearest to and farthest from the Fe atom are shown by red solid and dashed curves, respectively. The PDOSs of the Fe t_2 (d_{xy},d_{yz},d_{zx}) and e ($d_{x^2-y^2}$,d_{z^2}) orbitals are also shown by blue and green
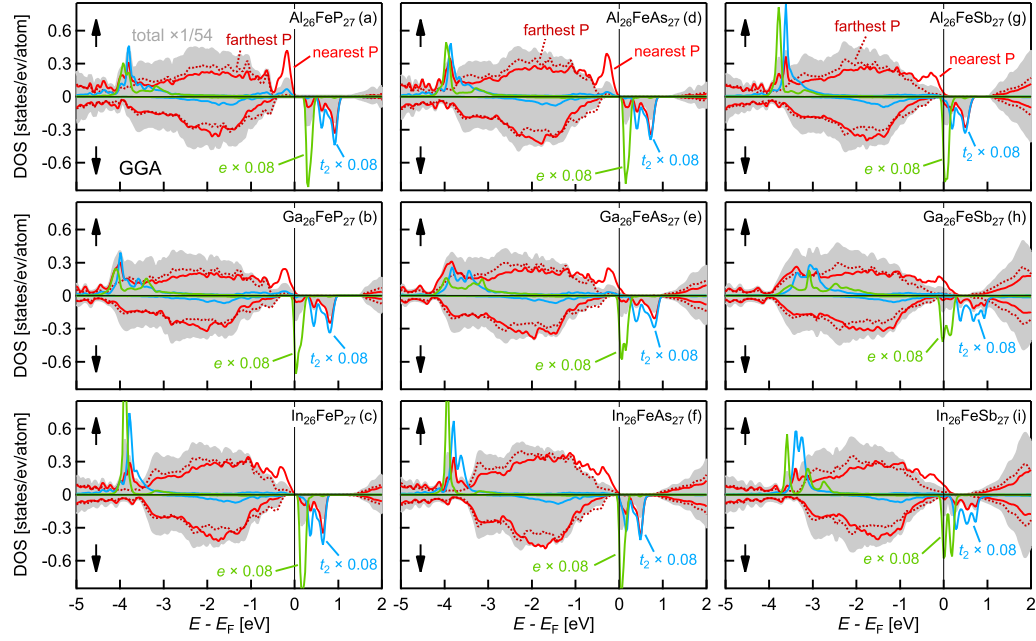
Figure 6.2: Total and partial densities of states of Fe-doped III-V semiconductors, namely, (a) AlP, (b) GaP, (c) InP, (d) AlAs, (e) GaAs, (f) InAs, (g) AlSb, (h) GaSb, and (i) InSb. Here, gray areas indicate the total DOSs, and red solid and dashed curves the PDOSs of group-V atoms nearest to and farthest from the Fe atom, respectively. The Fe t_2 and e PDOSs are also shown by blue and green curves. For ease of comparison, the total DOSs have been divided by 54 (total number of atoms in the supercell), and the Fe t_2 and e PDOSs have been multiplied by 0.08. The positive and negative values of the DOS represent the majority-spin and minority-spin contributions.

curves. For the sake of easy comparison, the total DOS have been divided by 54 (the total number of atoms in the supercell), and the PDOSs of the Fe t_2 and e orbitals have been multiplied by 0.08. The positive and negative values of DOS represent majority-spin and minority-spin contribution Note that the positive and negative values of the DOS represent the majority-spin and minority-spin contributions.

Taking into account the calculated DOSs, a schematic energy diagram is illustrated in Fig. 6.1. The valence and conduction bands of the host semiconductors are shown in the middle of the figure by green boxes, and the majority-spin and minority-spin $3d$ levels of the Fe atom without p-d hybridization are shown on the left- and right-hand sides, respectively. The $3d$ levels split into doubly-degenerate lower e state and triply-degenerate higher t_2 state because of the tetrahedral crystal field at the substitutional sites of group-III element

in zinc blende crystal. Furthermore, the Fe t_2 orbitals and the ligand p orbitals hybridize with each other rather strongly and form bonding and antibonding states. The majority-spin bonding state ($t_{b,\uparrow}$) of predominant Fe t_2 character is located deep about 3-4 eV below the Fermi energy (E_F), while the antibonding state ($t_{a,\uparrow}$) of predominant p character is just at the top of the valence band. On the other hand, the minority-spin bonding state ($t_{b,\downarrow}$) mainly consisting of ligand p orbitals forms a part of the valence band, and the antibonding state ($t_{a,\downarrow}$) of t_2 characters remains unoccupied. Note that the e orbitals do not strongly hybridize with ligand orbitals.

In the case of prototypical (III,Mn)V systems, because the Mn atom with the $3d^5(4sp)^2$ configuration substitutes for the Ga atom with $(4sp)^3$ and one hole is introduced in the valence band, the $t_{a,\uparrow}$ level pushed up above the E_F accommodate the hole. On the other hand, in the case of (III,Fe)V system, since Fe has one more electron than Mn and can take the $3d^5(4sp)^3$ configuration, the $t_{a,\uparrow}$ states would remain occupied. According to the present calculation, this is the case for (Al,Fe)P, (Al,Fe)As, and (In,Fe)P. To be more precise, Fe $3d$ and ligand p orbitals takes the $e_{\uparrow}^2(t_{b,\uparrow}t_{b,\downarrow})^3 t_{a,\uparrow}^3$ configuration in those cases, while Mn in III-V semiconductors takes the $e_{\uparrow}^2(t_{b,\uparrow}t_{b,\downarrow})^3 t_{a,\uparrow}^2$ configuration. (Ga,Fe)Sb and (In,Fe)Sb, on the other hand, show a distinct behavior. That is, the Fe and ligand orbitals take the $e_{\uparrow}^2(t_{b,\uparrow}t_{b,\downarrow})^3 t_{a,\uparrow}^2 e_{\downarrow}^1$ configuration, where one electron occupies the $e_{\downarrow}$ state instead of $t_{a,\uparrow}$. This is probably because the valence bands or the p levels of GaSb and InSb are rather high in energy [122], and it becomes more stable for the additional electron to occupy the $e_{\downarrow}$ state than to occupy the $t_{a,\uparrow}$ state. For the sake of convenience, the former electronic configuration $e_{\uparrow}^2(t_{b,\uparrow}t_{b,\downarrow})^3 t_{a,\uparrow}^3$ is denoted as Fe^{3+} hereafter, and the latter configuration $e_{\uparrow}^2(t_{b,\uparrow}t_{b,\downarrow})^3 t_{a,\uparrow}^2 e_{\downarrow}^1$ as Fe^{2+}. The other systems such as (Ga,Fe)As and (Al,Fe)Sb are intermediate cases, where a fraction of an electron occupies the $e_{\downarrow}$ state and a fraction of a hole occupies the $t_{a,\uparrow}$ states. This is represented by red dashed arrows in Fig. 6.1, where the electron of the highest energy occupies either the $t_{a,\uparrow}$ or $e_{\downarrow}$ levels. This situation is also illustrated in Fig. 6.3, where the band offsets of III-V semiconductors [122] and Ge [126] are shown. The dashed line roughly represents the energy level above which the Fe^{2+} configuration becomes more favorable. Note that the position of the dashed line is the $Fe^{3+/2+}$ charge transfer level observed in GaAs [127]. Considering that (Ga,Fe)As is paramagnetic [48,128], while the other Fe-doped semiconductors whose valence band maximum is located higher in energy than that of GaAs are ferromagnetic, ferromagnetism seems to appear when the Fe $e_{\downarrow}$ level becomes more likely to be occupied.

The strength of p-d hybridization or the exchange interaction between the d
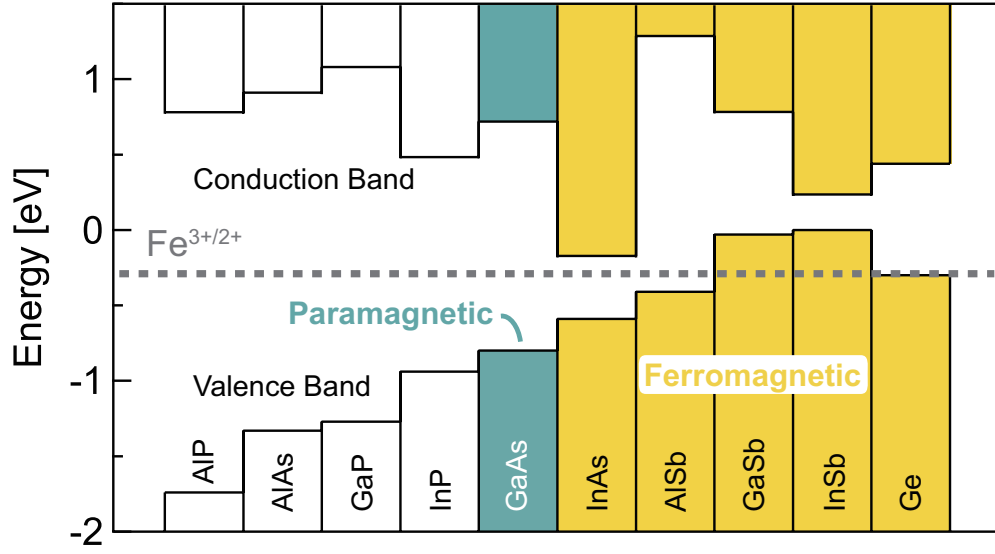
Figure 6.3: Band offsets of III-V semiconductors [122] and Ge. The band offset of Ge was an average value obtained from Ge/GaAs heterojunctions [126]. The boxes at the bottom represent valence bands, while the ones at the top conduction bands. The dashed line roughly represents the energy level above which Fe takes the Fe^{2+} configuration rather than Fe^{3+}. The position of the line was determined so that it corresponds to the $Fe^{3+/2+}$ charge transfer level in GaAs [127].

spin and the valence-band maximum ΔE_v caused by p-d hybridization can be most simply estimated by $t_{pd}^2/(E_p - E_d^\uparrow)$, where t_{pd} denotes a transfer integral between the ligand p and Fe t_2 orbitals, and E_p and $E_d^\uparrow$ the energy level of the ligand p and majority-spin Fe t_2 orbitals without the hybridization. For example, as the host semiconductor changes from AlP to GaP to InP, the hybridization becomes weaker because the increase in the lattice constant leads to the decrease in t_{pd} and the higher energy position of the valence band (E_p) results in the increase in $E_p^\uparrow - E_d^\uparrow$. This trend also holds for the AlAs $\to$ GaAs $\to$ InAs series and basically for the AlSb $\to$ GaSb $\to$ InSb series too. In fact, the splitting of the valence band summarized in Table 6.1 decreased as one goes from (Al,Fe)X to (Ga,Fe)X to (In,Fe)X, where X represents P, As, or Sb.

Note that the exchange splitting of the conduction-band minimum (ΔE_c) is significantly smaller than that of the valence band since s-d hybridization is very weak compared to p-d hybridization. Recent tunneling spectroscopy measurements [129] on ferromagnetic (In,Fe)As revealed that the splitting of

the conduction band was as small as 31.7 and 50 meV for 6% and 8% Fe doping, respectively. These values agree with the calculated one of 20 meV for 3.7% Fe doping, because the $N_0\alpha = \Delta E_c/x \langle S \rangle$ can be calculated assuming $\langle S \rangle = 5/2$ to be 0.22 eV and is almost the same as the experimental 0.21-0.25 eV.

Table 6.1 also shows the calculated spin and orbital magnetic moments of Fe atom, and the total magnetic moment of the supercell. Because of the strong p-d hybridization, a sizable amount of $3d$ electrons also occupies the $t_{b,\downarrow}$ states. This results in the smaller magnetic moment of Fe atoms than the ionic value of 5 μ_B. In the system with empty $e_\downarrow$ level such as (Al,Fe)P or (In,Fe)P, however, the total magnetic moment of the supercell is exactly 5 μ_B. Similar behavior was reported for (Ga,Mn)As [130], where the DFT calculation based on the local-spin-density approximation (LSDA) gives the Mn moment to be 3.47 μ_B, while the magnetic moment in the unit cell is exactly 4 μ_B. In the case of (Ga,Fe)Sb and (In,Fe)Sb, because an electron occupies the $e_\downarrow$ states instead of $t_{a,\uparrow}$, the total magnetic moment in the supercell is reduced by $\sim$1 μ_B. The intermediate cases of (Ga,Fe)As and (Al,Fe)Sb showed that the total magnetic moment is slightly smaller than 5 μ_B. Note that the number of $3d$ electrons is close to 6 for all the systems under the present study.

The orbital magnetic moment to spin magnetic moment ratio (m_l/m_s) increases from 0.015 to 0.061 as the host semiconductor becomes heavier and the spin-orbit interaction becomes stronger. This is qualitatively consistent with the results of the previous x-ray magnetic circular dichroism experiments that m_l/m_s increases from 0.1 for (In,Fe)As [52] to 0.13 for (Ga,Fe)Sb. The quantitative discrepancies are due to the limited ability of DFT in the prediction of orbital magnetism.

6.4   Discussion

In Fe^{3+} systems such as (Al,Fe)P, only superexchange interaction can be effective since no carriers are available for s, p-d exchange and double exchange interaction. The superexchange interaction is very short-ranged and antiferromagnetic for nearest Fe-As-Fe pairs [89] and, therefore, the ferromagnetism is not expected, especially when Fe atoms are distributed dilutely and randomly. On the other hand, (In,Fe)As (Fe 6%, $T_C = 45$ K) [129] and (Al,Fe)Sb (Fe 10%, $T_C = 40$ K) [46] exhibit ferromagnetism in spite of the very low carrier concentrations of 1×10^{18} cm^{-3} and 3×10^{17} cm^{-3}, respectively. In order to resolve this inconsistency, it may be necessary to consider the inhomogeneous distribution of Fe atoms or the spinodal decomposition on the nanoscale [131]. Actually, previous XMCD measurements on (In,Fe)As:Be [52] and (Al,Fe)Sb

Table 6.1: Calculated spin and orbital magnetic moments (m_s and m_l) of Fe atom, spin magnetic moment M_s in the supercell, the exchange interaction between the d spin and the valence band ΔE_v and the exchange splitting of the conduction band ΔE_c.

material	m_s $[\mu_B/\text{Fe}]$	m_l/m_s	M_s $[\mu_B/\text{cell}]$	ΔE_v [eV]	ΔE_c [eV]
(Al,Fe)P	3.33	0.015	5.00	0.41	0.08
(Ga,Fe)P	3.31	0.016	4.91	0.32	0.04
(In,Fe)P	3.51	0.017	5.00	0.21	0.02
(Al,Fe)As	3.33	0.023	4.97	0.34	0.06
(Ga,Fe)As	3.37	0.024	4.76	0.23	0.03
(In,Fe)As	3.48	0.027	4.96	0.22	0.02
(Al,Fe)Sb	3.29	0.043	4.89	0.28	0.04
(Ga,Fe)Sb	3.06	0.049	3.69	0.34	0.04
(In,Fe)Sb	3.30	0.061	4.16	0.25	0.03

indicated that there exist nanoscale ferromagnetic domains even at room temperature well above the macroscopic T_C, the origin of which was attributed to a nanoscale fluctuation of the Fe concentration. In such a case, the electronic structure may change in a way that the band width of Fe $3d$ states becomes broad.

Vu *et al.* [89] theoretically studied the chemical pair interactions as well as the electronic structure of (In,Fe)As:Be, and found that the Fe atoms tend to segregate to form an ordered phase especially when co-doped with Be. In addition, they showed that electrons provided by Be doping occupies the $e_\downarrow$ states as well as the conduction band and concluded that the double exchange interaction between the e orbitals is a source of ferromagnetism. Although the double exchange interaction is short ranged, the nanoscale non-uniformity of the Fe distribution can induce locally strong ferromagnetic interaction and hence ferromagnetic order. Such a scenario was discussed for Fe doped Ge [90, 91] as well, and may also be applied to the other Fe-doped FMSs discovered thus far, namely, (Al,Fe)Sb, (Ga,Fe)Sb, and (In,Fe)Sb, because the higher p energy levels, or the more strongly covalent nature, of Sb-based semiconductors is more likely to have electrons occupying the $e_\downarrow$ states, making double exchange interaction effective. In order to confirm this, further theoretical studies to examine the Fe concentration dependence of the electronic structure and exchange interaction are needed.

The transport properties of the Fe-doped semiconductors are another puz-

zle. n-type transport was reported for (In,Fe)As and (In,Fe)Sb, p-type for (Ga,Fe)Sb and (Ge,Fe), and insulating for (Al,Fe)Sb. If s,p-d exchange interaction were a dominant source of ferromagnetism, the n-type and insulating materials would have significantly smaller T_C because s-d exchange interaction is very small $\Delta E_v >> \Delta E_c$ as indicated in Table 6.1. However, the T_C of n-type (In,Fe)As and (In,Fe)Sb was actually even higher than that of p-type (Ga,Fe)Sb for the similar Fe content [40]. This again calls for another mechanism such as double-exchange interaction already discussed. In this regard, ferromagnetism and the transport in the Fe-doped III-V semiconductors may not be related and may be occurring in spatially rather separated regions in such a way that local ferromagnetic order in Fe-rich regions governs the ferromagnetism, while transport occurs in Fe-poor host-semiconductor-like regions with native defects.

6.5   Summary

In present study, we have calculated the basic electronic structures of Fe-doped III-V semiconductors by first-principles supercell calculation. The electronic structures of Fe-doped III-V semiconductors can be understood on the basis of the electronic structures of Mn-doped III-V compounds except that the additional electron of Fe compared to Mn occupies either a majority-spin antibonding state ($t_{a,\uparrow}$) or a minority-spin e state ($e_{\downarrow}$). The $e_{\downarrow}$ state is preferentially occupied in the cases of (Ga,Fe)Sb and (In,Fe)Sb, where the valence band or p level is located high in energy and, therefore, it is more stable for the additional electron to occupy the $e_{\downarrow}$ state than to occupy the $t_{a,\uparrow}$ state. As the group-III element changes from Al to Ga to In, p-d exchange interaction becomes weaker because the increase of Fe-group V atom bond length leads to the decrease of the transfer integral t_{pd} between the Fe t_2 and ligand p orbitals. As the group-V element changes from P to As to Sb, p-d exchange interaction also becomes weaker because the more strongly covalent nature and the higher energy position of the p levels make $E_p - E_d^{\uparrow}$ larger. The present calculations implied that the ferromagnetism originates from the nanoscale fluctuation of Fe atom distribution, because otherwise the small amount of carriers is not likely to stabilize the long-range ferromagnetic order unlike the carrier-induced ferromagnetism in the Mn-doped III-V semiconductors, especially in the case of n-type (In,Fe)As and (In,Fe)Sb, where s-d exchange interaction is very small, and insulating (Al,Fe)Sb.

Table 6.2: Parameters used for the present calculations: the lattice constants a [Å]; the muffin tin radii of Fe, group-III atoms, and group-V atoms, denoted by R_{MT}^{Fe}, R_{MT}^{III}, and R_{MT}^{V} [Bohr]; the plane wave cutoff K_{max}. Here, R_{MT}^{min} denotes the radius of smallest MT sphere.

material	a [Å]	R_{MT}^{Fe}	R_{MT}^{III}	R_{MT}^{V}	$R_{MT}^{min}K_{max}$
$Al_{26}FeP_{27}$	5.4672	2.5	2.33	1.95	5.5
$Ga_{26}FeP_{27}$	5.4505	2.49	2.44	1.94	5.5
$In_{26}FeP_{27}$	5.8697	2.5	2.5	2.09	5.5
$Al_{26}FeAs_{27}$	5.6611	2.36	2.19	2.24	6.5
$Ga_{26}FeAs_{27}$	5.6533	2.36	2.3	2.24	7.5
$In_{26}FeAs_{27}$	6.0583	2.5	2.5	2.4	7.5
$Al_{26}FeSb_{27}$	6.1355	2.49	2.3	2.49	6.5
$Ga_{26}FeSb_{27}$	6.0959	2.47	2.41	2.47	7.5
$In_{26}FeSb_{27}$	6.4794	2.5	2.5	2.5	8

6.6   Appendix

The parameters used for the present calculations are summarized in Table 6.2.

Chapter 7

Summary & Outlook

As introduced in Chapter 1, Fe-doped FMSs have advantages over prototypical Mn-doped systems such as (Ga,Mn)As. First, the Curie temperature (T_C) exceeds room temperature, 340 K for (Ga,Fe)Sb (Fe 25%) and 335 K for (In,Fe)Sb (Fe 16%). Second, various types of transport are realized, p-type for (Ga,Fe)Sb and Ge:Fe, n-type for (In,Fe)As:Be and (In,Fe)Sb, and insulating for (Al,Fe)Sb, while the Mn-doped compounds are always p-type. Despite the attractive properties, the mechanism of how ferromagnetism appears was unclear. In previous studies, we have found peculiar superparamagnetic behavior well above T_C in (In,Fe)As:Be and Ge:Fe. This was attributed to the non-uniform distribution of Fe atoms on the nanoscale, which also would be a key to understand the ferromagnetism. In the present thesis, in order to reveal the origin of the ferromagnetism as well as the superparamagnetic behavior, we have investigated their electronic structure and magnetic properties using x-ray absorption spectroscopy (XAS), x-ray magnetic circular dichroism (XMCD), resonance photoemission spectroscopy (RPES), soft x-ray angle-resolved photoemission spectroscopy (SX-ARPES), and first-principles supercell calculation.

In Chapter 3, we have performed XAS and XMCD measurements to study the magnetization process of (Al,Fe)Sb thin films. For an optimally doped sample with 10% Fe, a large magnetic response was found at room temperature well above the T_C of 40 K. We have attributed this behavior to the existence of nanoscale Fe-rich ferromagnetic domains acting as superparamagnet, and fitted the magnetization curves to the Langevin function representing superparamagnetism plus a paramagnetic linear function. It was found from the fitting that the average magnetic moment of the nanoscale ferromagnetic domain to be $\sim$400 μ_B, and the fraction of Fe atoms participating in the nanoscale ferromagnetism to be $\sim$50%. Further Fe doping up to 14% led to the weakening of the ferromagnetism and the strengthening of antiferromagnetic

correlation between Fe atoms probably because superexchange interaction between nearest-neighbor Fe-Fe pairs becomes dominant.

In Chapter 4, RPES, SX-ARPES, and first-principles calculation studies of group IV FMS Fe-doped Ge (Ge:Fe) have been presented. ARPES spectra showed that the Fermi level is located 0.35 eV in the middle of the band gap above the valence band maximum. From RPES spectra, non-dispersive Fe $3d$ states were found to exist at the Fermi level. This was attributed to majority-spin p-$d(t_2)$ antibonding states and also to minority-spin Fe $3d(e)$ states taking into account the results of the first-principles supercell calculation. It was suggested that the ferromagnetic interaction is mediated by double-exchange interaction within the minority-spin Fe $3d(e)$ band especially in Fe-rich regions.

In Chapter 5, the electronic structure and the magnetism of (Ga,Fe)Sb studied by XAS, XMCD, RPES and first-principles supercell calculation has been discussed. Analyses of XAS and XMCD spectra suggested that the ferromagnetism is of intrinsic origin and that the orbital moment is large, which implied the $3d^6$ configurations. From RPES, we observed a strong dispersive Auger peak and non-dispersive resonantly enhanced peaks in the valence-band spectra. The latter is a fingerprint of the correlated nature of Fe $3d$ electrons, whereas the former indicates their itinerant nature. First-principles supercell calculations also indicated that the substitutional Fe atom takes the valence of 2+ with six $3d$ electrons and that the valence-band maximum is located above the Fermi level, accommodating hole carriers in the GaSb host. This might be a reason why the hole concentration increases with Fe doping. The calculation also indicated that there are two kinds of ferromagnetic interactions, namely, short-range double-exchange interaction between the minority-spin Fe $3d(e)$ electrons and long-range interaction mediated by the hole carriers in the p-$d(t_2)$ anti-bonding states.

Chapter 6 summarizes the electronic structures of Fe-doped III-V semiconductors obtained by first-principles supercell calculation. The results were understood on the basis of the electronic structures of Mn-doped III-V compounds except that the additional electron of Fe compared to Mn occupies a majority-spin antibonding state ($t_{a,\uparrow}$) in the case of AlP or InP, where the energy of the valence band is low, or a minority-spin e states ($e_\downarrow$) in the case of GaSb and InSb, where the valence band or p level is located high in energy. The former cases give the magnetic moment of 5 μ_B per supercell, while the latter cases give a reduced magnetic moment because of the $e_\downarrow$ electron. Considering the fact that long range ferromagnetic order occurs in n-type (In,Fe)As:Be and (In,Fe)Sb, where the s-d exchange interaction should be weak, and insulating (Al,Fe)Sb, where carriers are absent, it was suggested that the high-

temperature ferromagnetism in Fe-doped III-V ferromagnetic semiconductors originates from ferromagnetic interaction between $e_\downarrow$ orbitals of Fe atoms separated by short distances, that arises from the nanoscale fluctuation of Fe atom distribution.

In this thesis, it is concluded that the ferromagnetic interaction in the Fe-doped FMSs is mediated by double-exchange interaction within the minority-spin Fe e bands, which are preferentially occupied when valence band maximum is located high in energy as in Sb-based materials. This interaction should be especially strong in Fe-rich regions, causing superparamagnetic behavior above T_C. In order to confirm this scenario, it would be necessary to examine what would happen when Fe atoms are doped into other semiconductors with wide band gap or low valence-band energy position such as AlP. In such a case, it is expected that Fe takes the Fe^{3+} configuration and ferromagnetism does not appear. It is also interesting to conduct XMCD measurements at high temperatures above room temperature so that the disappearance of the superparamagnetic behavior can be seen. ARPES measurements on (Al,Fe)Sb, (Ga,Fe)Sb, and (In,Fe)Sb are also required to investigate how valence-band position changes with varying host semiconductors. Lastly, detailed theoretical calculations are also needed.

Acknowledgments

It is my great pleasure to express special gratitude to the following people for their help concerning my doctoral study.

First of all, I would like to express my sincere gratitude to my supervisor Prof. Atsushi Fujimori, who has given me the opportunity to be engaged in a lot of exciting and fruitful researches. Without his continuous guidance and enlightening advices, my doctoral studies would never have been accomplished. I have been very fortunate to have a supervisor like him who is passionate about education and has immense knowledge of physics, from which I could learn many things.

I appreciate the financial supports from Advanced Leading Graduate Course for Photon Science (ALPS) and the JSPS Research Fellowship for Young Scientists. I am very grateful to Prof. Tomoko Ohtsuki and Dr. Avi Mukherjee for giving me an internship opportunity through ALPS program at Western Digital, San Jose and for supporting me during the stay. I also thank the colleagues at Western Digital, especially Dr. Antony Ajan, Dr. Kumar Srinivasan, Dr. Oleg Krupin, and Dr. Rui Zhang, who always guided me and allowed me to start the collaboration between our group and Western Digital after the internship. With their efforts, we could publish a paper in Physical Review B, although it is not included in this thesis.

The high quality Fe-doped ferromagnetic semiconductor samples are provided by Prof. Masaaki Tanaka's group from the Department of Electrical Engineering and Information Systems, the University of Tokyo. I deeply thank Prof. Masaaki Tanaka, Prof. Shinobu Ohya, and Prof. Pham Nam Hai, who has given me the chance to study the very interesting materials. My deep gratitude also goes to the members of the group, Dr. Le Duc Anh, Dr. Nguyen Thanh Tu, Dr. Yuki Wakabayashi, and Mr. Yoshisuke Ban who actually grew the samples for my research. I thank Prof. Ryosho Nakane for taking part in the experiments at BL23SU of SPring-8. The fruitful discussions with them have strongly motivated me and kept my research moving forward.

The experiments at BL23SU of SPring-8 were supported by Dr. Yukiharu

December 2017
Shoya Sakamoto

References

[1] S. A. Wolf, D. D. Awschalom, R. A. Buhrman, J. M. Daughton, S. von Molnár, M. L. Roukes, A. Y. Chtchelkanova, and D. M. Treger, Science **294**, 1488 (2001).

[2] B. Matthias, R. Bozorth, and J. Van Vleck, Phys. Rev. Lett. **7**, 160 (1961).

[3] T. R. McGuire, B. E. Argyle, M. W. Shafer, and J. S. Smart, Appl. Phys. Lett. **1**, 17 (1962).

[4] T. R. McGuire and M. W. Shafer, J. Appl. Phys. **35**, 984 (1964).

[5] T. Kasuya and A. Yanase, Rev. Mod. Phys. **40**, 684 (1968).

[6] J. K. Furdyna, J. Appl. Phys. **64**, R29 (1988).

[7] H. Ohno, Science **281**, 951 (1998).

[8] H. Munekata, H. Ohno, S. von Molnar, A. Segmüller, L. L. Chang, and L. Esaki, Phys. Rev. Lett. **63**, 1849 (1989).

[9] H. Munekata, Mater. Sci. Eng., B **31**, 151 (1995).

[10] F. Matsukura, H. Ohno, and T. Dietl, Handbook of Magnetic Materials **14**, 1 (2002).

[11] H. Ohno, H. Munekata, T. Penney, S. von Molnár, and L. Chang, Phys. Rev. Lett. **68**, 2664 (1992).

[12] H. Ohno, A. Shen, F. Matsukura, A. Oiwa, A. Endo, S. Katsumoto, and Y. Iye, Appl. Phys. Lett. **69**, 363 (1996).

[13] F. Matsukura, H. Ohno, A. Shen, and Y. Sugawara, Phys. Rev. B **57**, R2037 (1998).

[14] T. Dietl and H. Ohno, Rev. Mod. Phys. **86**, 187 (2014).

[15] T. Jungwirth, J. Wunderlich, V. Novák, K. Olejník, B. L. Gallagher, R. P. Campion, K. W. Edmonds, A. W. Rushforth, A. J. Ferguson, and P. Němec, Rev. Mod. Phys. **86**, 855 (2014).

[16] L. Chen, X. Yang, F. Yang, J. Zhao, J. Misuraca, P. Xiong, and S. von Molnár, Nano Lett. **11**, 2584 (2011).

[17] T. Schallenberg and H. Munekata, Appl. Phys. Lett. **89**, 042507 (2006).

[18] P. Němec, V. Novák, N. Tesařová, E. Rozkotová, H. Reichlová, D. Butkovičová, F. Trojánek, K. Olejník, P. Malý, R. P. Campion, B. L. Gallagher, J. Sinova, and T. Jungwirth, Nat. Commun. **4**, 1422 EP (2013).

[19] M. Mayer, P. Stone, N. Miller, H. Smith, O. Dubon, E. Haller, K. Yu, W. Walukiewicz, X. Liu, and J. Furdyna, Phys. Rev. B **81**, 045205 (2010).

[20] T. Dietl, H. Ohno, and F. Matsukura, Phys. Rev. B **63**, 195205 (2001).

[21] K. Yu, W. Walukiewicz, T. Wojtowicz, I. Kuryliszyn, X. Liu, Y. Sasaki, and J. Furdyna, Phys. Rev. B **65**, 201303 (2002).

[22] K. Y. Wang, K. W. Edmonds, R. P. Campion, B. L. Gallagher, N. R. S. Farley, C. T. Foxon, M. Sawicki, P. Boguslawski, and T. Dietl, J. Appl. Phys. **95**, 6512 (2004).

[23] Y. Takeda, M. Kobayashi, T. Okane, T. Ohkochi, J. Okamoto, Y. Saitoh, K. Kobayashi, H. Yamagami, A. Fujimori, A. Tanaka, J. Okabayashi, M. Oshima, S. Ohya, P. N. Hai, and M. Tanaka, Phys. Rev. Lett. **100**, 247202 (2008).

[24] H. Ohno, D. Chiba, F. Matsukura, T. Omiya, E. Abe, T. Dietl, Y. Ohno, and K. Ohtani, Nature **408**, 944 (2000).

[25] D. Chiba, F. Matsukura, and H. Ohno, Appl. Phys. Lett. **89**, 162505 (2006).

[26] M. Sawicki, D. Chiba, A. Korbecka, Y. Nishitani, J. A. Majewski, F. Matsukura, T. Dietl, and H. Ohno, Nat. Phys. **6**, 22 (2010).

[27] H. Munekata, T. Abe, S. Koshihara, A. Oiwa, M. Hirasawa, S. Katsumoto, Y. Iye, C. Urano, and H. Takagi, J. Appl. Phys. **81**, 4862 (1997).

[28] S. Koshihara, A. Oiwa, M. Hirasawa, S. Katsumoto, Y. Iye, C. Urano, H. Takagi, and H. Munekata, Phys. Rev. Lett. **78**, 4617 (1997).

[29] Y. Ohno, D. K. Young, B. Beschoten, F. Matsukura, H. Ohno, and D. D. Awschalom, Nature **402**, 790 (1999).

[30] C. Zener, Phys. Rev. **82**, 403 (1951).

[31] K. Sato, L. Bergqvist, J. Kudrnovský, P. H. Dederichs, O. Eriksson, I. Turek, B. Sanyal, G. Bouzerar, H. Katayama-Yoshida, V. A. Dinh, T. Fukushima, H. Kizaki, and R. Zeller, Rev. Mod. Phys. **82**, 1633 (2010).

[32] C. Zener, Phys. Rev. **81**, 440 (1951).

[33] M. Kobayashi, I. Muneta, Y. Takeda, Y. Harada, A. Fujimori, J. Krempaský, T. Schmitt, S. Ohya, M. Tanaka, M. Oshima, and V. N. Strocov, Phys. Rev. B **89**, 205204 (2014).

[34] M. Kobayashi, I. Muneta, T. Schmitt, L. Patthey, S. Ohya, M. Tanaka, M. Oshima, and V. N. Strocov, Appl. Phys. Lett. **101**, (2012).

[35] T. Dietl, H. Ohno, F. Matsukura, J. Cibert, and D. Ferrand, Science **287**, 1019 (2000).

[36] P. Nam Hai, D. Sasaki, L. D. Anh, and M. Tanaka, Appl. Phys. Lett. **100**, 262409 (2012).

[37] P. Nam Hai, L. D. Anh, and M. Tanaka, Appl. Phys. Lett. **101**, 252410 (2012).

[38] P. Nam Hai, L. Duc Anh, S. Mohan, T. Tamegai, M. Kodzuka, T. Ohkubo, K. Hono, and M. Tanaka, Appl. Phys. Lett. **101**, 182403 (2012).

[39] M. Tanaka, S. Ohya, and P. Nam Hai, Appl. Phys. Rev. **1**, 011102 (2014).

[40] N. Thanh Tu, P. N. Hai, L. D. Anh, and M. Tanaka, arXiv:1706.00735 .

[41] N. T. Tu, P. N. Hai, L. D. Anh, and M. Tanaka, Appl. Phys. Lett. **105**, 132402 (2014).

[42] N. T. Tu, P. N. Hai, L. D. Anh, and M. Tanaka, Phys. Rev. B **92**, 144403 (2015).

[43] N. T. Tu, P. N. Hai, L. D. Anh, and M. Tanaka, Appl. Phys. Lett. **108**, 192401 (2016).

[44] Y. Shuto, M. Tanaka, and S. Sugahara, Appl. Phys. Lett. **90**, 132512 (2007).

[45] Y. K. Wakabayashi, Y. Ban, S. Ohya, and M. Tanaka, Phys. Rev. B **90**, 205209 (2014).

[46] L. D. Anh, D. Kaneko, P. N. Hai, and M. Tanaka, Appl. Phys. Lett. **107**, 232405 (2015).

[47] Y. Ban, Y. K. Wakabayashi, R. Nakane, and M. Tanaka, arXiv:1706.04445 .

[48] S. Haneda, M. Yamaura, Y. Takatani, K. Hara, S. ichi Harigae, and H. Munekata, Jpn. J. Appl. Phys. **39**, L9 (2000).

[49] D. Sasaki, L. D. Anh, P. Nam Hai, and M. Tanaka, Appl. Phys. Lett. **104**, 142406 (2014).

[50] K. Ando and H. Munekata, J. Magn. Magn. Mater. **272-276, Part 3**, 2004 (2004).

[51] K. Ando, Science **312**, 1883 (2006).

[52] S. Sakamoto, L. D. Anh, P. N. Hai, G. Shibata, Y. Takeda, M. Kobayashi, Y. Takahashi, T. Koide, M. Tanaka, and A. Fujimori, Phys. Rev. B **93**, 035203 (2016).

[53] A. V. Kudrin, Y. A. Danilov, V. P. Lesnikov, M. V. Dorokhin, O. V. Vikhrova, D. A. Pavlov, Y. V. Usov, I. N. Antonov, R. N. Kriukov, A. V. Alaferdov, and N. A. Sobolev, J. Appl. Phys. **122**, 183901 (2017).

[54] Y. K. Wakabayashi, S. Ohya, Y. Ban, and M. Tanaka, J. Appl. Phys. **116**, 173906 (2014).

[55] Y. K. Wakabayashi, S. Sakamoto, Y.-h. Takeda, K. Ishigami, Y. Takahashi, Y. Saitoh, H. Yamagami, A. Fujimori, M. Tanaka, and S. Ohya, Sci. Rep. **6**, 23295 (2016).

[56] F. de Groot, J. Electron. Spectrosc. Relat. Phenom. **67**, 529 (1994).

[57] K. Amemiya, S. Kitagawa, D. Matsumura, H. Abe, T. Ohta, and T. Yokoyama, Appl. Phys. Lett. **84**, 936 (2004).

[58] S. Eisebitt, T. Böske, J.-E. Rubensson, and W. Eberhardt, Phys. Rev. B **47**, 14103 (1993).

[59] R. Nakajima, J. Stöhr, and Y. U. Idzerda, Phys. Rev. B **59**, 6421 (1999).

[60] M. Kobayashi, Y. Ishida, J. I. Hwang, Y. Osafune, A. Fujimori, Y. Takeda, T. Okane, Y. Saitoh, K. Kobayashi, H. Saeki, T. Kawai, and H. Tabata, Phys. Rev. B **81**, 075204 (2010).

[61] T. Funk, A. Deb, S. J. George, H. Wang, and S. P. Cramer, Coord. Chem. Rev. **249**, 3 (2005).

[62] A. Scherz, Doctor Thesis at Free University of Berlin (2003).

[63] M. Kobayashi, Doctor Thesis at the University of Tokyo (2007).

[64] B. T. Thole, P. Carra, F. Sette, and G. van der Laan, Phys. Rev. Lett. **68**, 1943 (1992).

[65] P. Carra, B. T. Thole, M. Altarelli, and X. Wang, Phys. Rev. Lett. **70**, 694 (1993).

[66] J. Stöhr and H. König, Phys. Rev. Lett. **75**, 3748 (1995).

[67] C. T. Chen, Y. U. Idzerda, H.-J. Lin, N. V. Smith, G. Meigs, E. Chaban, G. H. Ho, E. Pellegrin, and F. Sette, Phys. Rev. Lett. **75**, 152 (1995).

[68] Y. Teramura, A. Tanaka, and T. Jo, J. Phys. Soc. Jpn. **65**, 1053 (1996).

[69] C. Piamonteze, P. Miedema, and F. M. F. de Groot, Phys. Rev. B **80**, 184410 (2009).

[70] M. Horio, Doctor Thesis at the University of Tokyo (2016).

[71] A. Damascelli, Z. Hussain, and Z.-X. Shen, Rev. Mod. Phys. **75**, 473 (2003).

[72] A. Fujimori, M. Saeki, N. Kimizuka, M. Taniguchi, and S. Suga, Phys. Rev. B **34**, 7318 (1986).

[73] A. Fujimori, N. Kimizuka, M. Taniguchi, and S. Suga, Phys. Rev. B **36**, 6691 (1987).

[74] O. Rader, C. Pampuch, A. M. Shikin, W. Gudat, J. Okabayashi, T. Mizokawa, A. Fujimori, T. Hayashi, M. Tanaka, A. Tanaka, and A. Kimura, Phys. Rev. B **69**, 075202 (2004).

[75] G. Levy, R. Sutarto, D. Chevrier, T. Regier, R. Blyth, J. Geck, S. Wurmehl, L. Harnagea, H. Wadati, T. Mizokawa, I. S. Elfimov, A. Damascelli, and G. A. Sawatzky, Phys. Rev. Lett. **109**, 077001 (2012).

[76] I. Di Marco, P. Thunström, M. I. Katsnelson, J. Sadowski, K. Karlsson, S. Lebègue, J. Kanski, and O. Eriksson, Nat. Commun. **4**, (2013).

[77] U. Fano, Phys. Rev. **124**, 1866 (1961).

[78] A. Tanaka and T. Jo, J. Phys. Soc. Jpn. **63**, 2788 (1994).

[79] F. J. García de Abajo, C. S. Fadley, and M. A. Van Hove, Phys. Rev. Lett. **82**, 4126 (1999).

[80] P. Hohenberg and W. Kohn, Phys. Rev. **136**, B864 (1964).

[81] W. Kohn and L. J. Sham, Phys. Rev. **140**, A1133 (1965).

[82] J. P. Perdew, K. Burke, and M. Ernzerhof, Phys. Rev. Lett. **77**, 3865 (1996).

[83] P. Blaha, K. Schwarz, G. Madsen, D. Kvasnicka, and J. Luitz, An augmented plane wave+ local orbitals program for calculating crystal properties (2001).

[84] Y. Saitoh, Y. Fukuda, Y. Takeda, H. Yamagami, S. Takahashi, Y. Asano, T. Hara, K. Shirasawa, M. Takeuchi, T. Tanaka, and H. Kitamura, J. Synchrotron Radiat. **19**, 388 (2012).

[85] Y. Saitoh, T. Nakatani, T. Matsushita, A. Agui, A. Yoshigoe, Y. Teraoka, and A. Yokoya, Nucl. Instr. Meth. Phys. Res. A **474**, 253 (2001).

[86] T. Hara, K. Shirasawa, M. Takeuchi, T. Seike, Y. Saito, T. Muro, and H. Kitamura, Nucl. Instr. Meth. Phys. Res. A **498**, 496 (2003).

[87] V. K. Verma, V. R. Singh, K. Ishigami, G. Shibata, T. Harano, T. Kadono, A. Fujimori, T. Koide, K. Ohgushi, and Y. Tokura, Photon Factory Activity Report **29 2011**, (2012).

[88] S. Brice-Profeta, M.-A. Arrio, E. Tronc, N. Menguy, I. Letard, C. C. dit Moulin, M. Noguès, C. Chanéac, J.-P. Jolivet, and P. Sainctavit, J. Magn. Magn. Mater. **288**, 354 (2005).

[89] N. D. Vu, T. Fukushima, K. Sato, and H. Katayama-Yoshida, Jpn. J. Appl. Phys. **53**, 110307 (2014).

[90] H. Shinya, T. Fukushima, A. Masago, K. Sato, and H. Katayama-Yoshida, Phys. Rev. B **96**, 104415 (2017).

[91] S. Sakamoto, Y. K. Wakabayashi, Y. Takeda, S.-i. Fujimori, H. Suzuki, Y. Ban, H. Yamagami, M. Tanaka, S. Ohya, and A. Fujimori, Phys. Rev. B **95**, 075203 (2017).

[92] I. Žutić, J. Fabian, and S. Das Sarma, Rev. Mod. Phys. **76**, 323 (2004).

[93] T. Dietl, Nat. Mater. **9**, 965 (2010).

[94] Y. Shuto, M. Tanaka, and S. Sugahara, J. Appl. Phys. **99**, 08D516 (2006).

[95] Y. Ban, Y. Wakabayashi, R. Akiyama, R. Nakane, and M. Tanaka, AIP Adv. **4**, 097108 (2014).

[96] T. Jungwirth, J. Sinova, J. Mašek, J. Kučera, and A. H. MacDonald, Rev. Mod. Phys. **78**, 809 (2006).

[97] J. Okabayashi, A. Kimura, O. Rader, T. Mizokawa, A. Fujimori, T. Hayashi, and M. Tanaka, Phys. Rev. B **64**, 125304 (2001).

[98] K. Sato and H. Katayama-Yoshida, Semicond. Sci. Technol. **17**, 367 (2002).

[99] K. S. Burch, D. B. Shrekenhamer, E. J. Singley, J. Stephens, B. L. Sheu, R. K. Kawakami, P. Schiffer, N. Samarth, D. D. Awschalom, and D. N. Basov, Phys. Rev. Lett. **97**, 087208 (2006).

[100] S. Ohya, K. Takata, and M. Tanaka, Nat. Phys. **7**, 342 (2011).

[101] S. Sun, Y. Sun, Z. Liu, D.-I. Lee, S. Peterson, and P. Pianetta, Appl. Phys. Lett. **88**, 021903 (2006).

[102] F. Tran and P. Blaha, Phys. Rev. Lett. **102**, 226401 (2009).

[103] G. van der Laan and I. W. Kirkman, J. Phys. Condens. Matter **4**, 4189 (1992).

[104] M. R. Thuler, R. L. Benbow, and Z. Hurych, Phys. Rev. B **26**, 669 (1982).

[105] C. Guillot, Y. Ballu, J. Paigné, J. Lecante, K. P. Jain, P. Thiry, R. Pinchaux, Y. Pétroff, and L. M. Falicov, Phys. Rev. Lett. **39**, 1632 (1977).

[106] M. Weinelt, A. Nilsson, M. Magnuson, T. Wiell, N. Wassdahl, O. Karis, A. Föhlisch, N. Mårtensson, J. Stöhr, and M. Samant, Phys. Rev. Lett. **78**, 967 (1997).

[107] S. Hüfner, S.-H. Yang, B. S. Mun, C. S. Fadley, J. Schäfer, E. Rotenberg, and S. D. Kevan, Phys. Rev. B **61**, 12582 (2000).

[108] F. Bondino, E. Magnano, M. Malvestuto, F. Parmigiani, M. A. McGuire, A. S. Sefat, B. C. Sales, R. Jin, D. Mandrus, E. W. Plummer, D. J. Singh, and N. Mannella, Phys. Rev. Lett. **101**, 267001 (2008).

[109] A. Koitzsch, R. Kraus, T. Kroll, M. Knupfer, B. Büchner, H. Eschrig, D. R. Batchelor, G. L. Sun, D. L. Sun, and C. T. Lin, Phys. Rev. B **81**, 174519 (2010).

[110] M. Kobayashi, L. D. Anh, P. N. Hai, Y. Takeda, S. Sakamoto, T. Kadono, T. Okane, Y. Saitoh, H. Yamagami, Y. Harada, M. Oshima, M. Tanaka, and A. Fujimori, Appl. Phys. Lett. **105**, 032403 (2014).

[111] S. Souma, L. Chen, R. Oszwałdowski, T. Sato, F. Matsukura, T. Dietl, H. Ohno, and T. Takahashi, Sci. Rep. **6**, 27266 EP (2016).

[112] K. Momma and F. Izumi, J. Appl. Crystallogr. **44**, 1272 (2011).

[113] H. Weng and J. Dong, Phys. Rev. B **71**, 035201 (2005).

[114] K. W. Edmonds, N. R. S. Farley, R. P. Campion, C. T. Foxon, B. L. Gallagher, T. K. Johal, G. van der Laan, M. MacKenzie, J. N. Chapman, and E. Arenholz, Appl. Phys. Lett. **84**, 4065 (2004).

[115] V. I. Anisimov, J. Zaanen, and O. K. Andersen, Phys. Rev. B **44**, 943 (1991).

[116] D. Wu, D. J. Keavney, R. Wu, E. Johnston-Halperin, D. D. Awschalom, and J. Shi, Phys. Rev. B **71**, 153310 (2005).

[117] J. Stöhr, J. Magn. Magn. Mater. **200**, 470 (1999).

[118] K. W. Edmonds, C. Binns, S. H. Baker, S. C. Thornton, C. Norris, J. B. Goedkoop, M. Finazzi, and N. B. Brookes, Phys. Rev. B **60**, 472 (1999).

[119] R. J. Lad and V. E. Henrich, Phys. Rev. B **39**, 13478 (1989).

[120] J.-S. Kang, J. H. Kim, A. Sekiyama, S. Kasai, S. Suga, S. W. Han, K. H. Kim, T. Muro, Y. Saitoh, C. Hwang, C. G. Olson, B. J. Park, B. W. Lee, J. H. Shim, J. H. Park, and B. I. Min, Phys. Rev. B **66**, 113105 (2002).

[121] M. Schmid, H.-P. Steinrück, and J. M. Gottfried, Surf. Interface Anal. **46**, 505 (2014).

[122] I. Vurgaftman, J. R. Meyer, and L. R. Ram-Mohan, J. Appl. Phys. **89**, 5815 (2001).

[123] E. Georgitse, L. Gutzuleac, A. Mikhelake, I. Postolachi, S. U. Yuldashev, and T. Kang, J. Lumin. **1**, 1 (2014).

[124] M. Linnarsson, E. Janzén, B. Monemar, M. Kleverman, and A. Thilderkvist, Phys. Rev. B **55**, 6938 (1997).

[125] M. Imada, A. Fujimori, and Y. Tokura, Rev. Mod. Phys. **70**, 1039 (1998).

[126] A. Franciosi and C. G. V. de Walle, Surf. Sci. Rep. **25**, 1 (1996).

[127] E. Malguth, A. Hoffmann, and M. R. Phillips, Phys. Status Solidi B **245**, 455 (2008).

[128] R. Moriya, Y. Katsumata, Y. Takatani, S. Haneda, T. Kondo, and H. Munekata, Phys. E **10**, 224 (2001).

[129] P. N. H. Le Duc Anh and M. Tanaka, Nat. Commun. **7**, (2016).

[130] A. B. Shick, J. Kudrnovský, and V. Drchal, Phys. Rev. B **69**, 125207 (2004).

[131] T. Dietl, K. Sato, T. Fukushima, A. Bonanni, M. Jamet, A. Barski, S. Kuroda, M. Tanaka, P. N. Hai, and H. Katayama-Yoshida, Rev. Mod. Phys. **87**, 1311 (2015).